Title

Effect of Grain Boundary Chemical Segregation on Electrical Transport in Complex Oxides

Permalink

https://escholarship.org/uc/item/84r9h1vf

Author

Vahidi, Hasti

Publication Date

2024

UNIVERSITY OF CALIFORNIA,
IRVINE

Effect of Grain Boundary Chemical Segregation on Electrical Transport in Complex Oxides

DISSERTATION

submitted in partial satisfaction of the requirements
for the degree of

DOCTOR OF PHILOSOPHY

in Materials Science and Engineering

by

Hasti Vahidi

Dissertation Committee:

Professor William J. Bowman, Chair
Professor Daniel Mumm
Professor Shen Dillon

2024

DEDICATION

I dedicate this dissertation to:

Maman Nayer and Baba Mohammadreza. None of this would have been possible without you.
Thank you for believing in me. I love you forevermore.
Parsa, I am more grateful for you every single day.
My mentor and friend, Will. Thank you for your confidence in me and for putting up with me.
Keith, thank you for being by my side and making me laugh.
Kladis and Farnoosh, thank you for making me feel at home since I came to the US.
Everyone I crossed paths with, in my journey through life and graduate school, with whom I
shared a meaningful connection, a deep conversation, a smile, laughter, or tears.

and lastly,

I dedicate this work to everyone who fights for freedom in Iran and around the world.

TABLE OF CONTENTS

LIST OF FIGURES

LIST OF TABLES

ACKNOWLEDGEMENTS

First and foremost, I would like to thank my Ph.D. advisor and dissertation committee chair, Prof. William Bowman. His enthusiasm and knowledge inspire me to be a better scientist. Thank you Will, for the opportunity to join your group as the first graduate student, before you had a lab. I am impressed and proud to see your research group grow and do bigger and better things. Thank you for continuously supporting me not only as a scientist, but as a person.

I would like to thank Prof. Daniel Mumm and Prof. Shen Dillon for serving as my dissertation committee members and for insightful discussions, feedback, and contributions. I would also like to thank Prof. Martha Mecartney, for her guidance and mentorship throughout my Ph.D. program, for helping me transition into a different research group and for allowing me to rotate in her group and use her lab space, before Bowman lab was up and running.

I want to thank my collaborators, especially: Prof. David Mebane and Alejandro Mejia (West Virginia University), Prof. Tim Rupert, Prof. Julie Schoenung, Justin Cortez and Pulkit Garg (UCI). Thanks to my collaborator Prof. Alexander Dupuy, who introduced me to research in graduate school when I first arrived at UCI. I will forever cherish his mentorship, friendship, and support.

I want to wholeheartedly thank all the past and present members of Bowman lab at UCI, for their friendship and support. Special acknowledgement goes to my dear friends Jenna Wardini, Komal Syed, Huiming Guo, Xin Wang, Shengquan Xuan and Somnath Mandal. I want to particularly thank Jenna and Komal, for our wonderful connections and discussions which kept me cheerful (and sane!) throughout this process.

A special thanks goes to my dear friend Shirley Chang, for being by my side and always cheering me on! Another special thanks to Sayna Yaghooby, for over 15 years of real friendship, I am grateful to have you as my best friend.

I want to thank the staff at Irvine Materials Research Institute (IMRI), especially Dr. Mingjie Xu, Dr. Toshihiro Aoki, Dr. Qiyin Lin and Dr. Jian-Guo Zheng for providing essential training and insights that was critical for my research. Special thanks to Dr. Mingjie Xu and Jenna Wardini, for teaching me how to use TEM and for our late-night discussions at IMRI.

Thanks to all the members of NSF-MRSEC at UCI particularly Prof. Regina Ragan and Prof. Horst Hahn, for their guidance and support. Thanks to all the staff at UCI MSE.

Portions of Chapters 1 and 2 of this dissertation are [a reprint / an adaptation] of the material as it appears in "A Review of Grain Boundary and Heterointerface Characterization in Polycrystalline Oxides by (Scanning) Transmission Electron Microscopy" in Crystals, used with permission from MDPI. The coauthors listed in this publication are Komal Syed, Huiming Guo, Xin Wang, Jenna L. Wardini, Jenny Martinez, and William J. Bowman. William J. Bowman directed and supervised research which forms the basis for the dissertation.

Chapter 4 of this dissertation is [a reprint / an adaptation] of the material as it appears in "Reversible Enhancement of Electronic Conduction Caused by Phase Transformation and Interfacial Segregation in an Entropy-Stabilized Oxide" in Advanced Functional Materials, used with permission from Wiley-VCH GmbH. The coauthors listed in this publication are Alexander D. Dupuy, Benjamin X. Lam, Justin Cortez, Pulkit Garg, Timothy J. Rupert, Julie M. Schoenung and William J. Bowman. William J. Bowman directed and supervised research which forms the basis for the dissertation.

I would like to acknowledge the UCI Samueli School of Engineering Faculty Start-up grant and the National Science Foundation (NSF-MRSEC at UCI) grant (DMR-2011967) for supporting my graduate research.

VITA

HASTI VAHIDI

EDUCATION

University of California Irvine — Irvine, CA
Ph.D. in Materials Science and Engineering — *June 2024*

University of California Irvine — Irvine, CA
M.Sc. in Materials Science and Engineering — *March 2019*

Iran University of Science and Technology — Tehran, Iran
B.Sc. in Materials Engineering-Ceramics — *Sep. 2016*

PROFESSIONAL EXPERIENCES

NSF-MRSEC Research Fellow — March 2020 – June 2024
PI: William Bowman, University of California Irvine — *Irvine, CA*

- Synthesized and characterized complex concentrated oxide materials (CCOs) with controllable microstructures for strengthening functional performance.
- Implemented electron microscopy techniques to study materials structure, composition and processing effects of bulk and interfaces at atomic scale.
- Discovered enhanced electrical conductivity in an entropy stabilized oxide by tuning bulk defect chemistry, measured via impedance spectroscopy.
- Collaborated with cross-functional teams, worked alongside and mentored lab members, and presented my work at international conferences.

Fuel Cell (Membrane Electrode Assemblies) Systems Intern — Jun 2021 – Sep. 2021
Ford Motor Company — *Dearborn, MI*

- Developed and upgraded MATLAB transfer functions to predict the degradation of PEM fuel cell stacks.
- Analyzed and incorporated large experimental data sets from F-550 truck customers data in models.
- Supported team members with voltage cycling and chemical degradation experimental design parameters.
- Investigated the impact of driver location (humidity, temperature) and vocation on fuel cell lifetime.
- Communicated research findings and future suggestions to team leaders in writing and oral presentations.

Materials Characterization Lab Assistant — Jan 2018 – Jan 2020
Irvine Materials Research Institute — *Irvine, CA*

- Trained and mentored over 40 students in understanding and operation of XRD, SEM, and EDS.

TECHNICAL SKILLS

Material Characterization:

- Electron Microscopy/Spectroscopy including SEM, TEM, S/TEM, EDS, EELS, EBSD and FIB
- X-ray Diffraction (XRD), High-temperature XRD, Thermogravimetric analysis (TGA), EIS and CV
- Magnetron Sputter Coating, Slip Casting, Uniaxial, Hot and Cold Isostatic Press, Machining, Polishing
- Nanoindentation, Vickers Hardness, Ball Milling and Batching, Solid-State Synthesis, Spark Plasma Sintering (SPS)

Programming and Software:

- MATLAB for simulation of complex physical phenomena.
- Adobe Illustrator and Inkscape for designing scientific/schematic figures.
- Crystal Maker, CrysTBox, PDXL2 and Vesta for detection and simulation of crystal structures.
- Digital Micrograph (GMS) for qualitative and quantitative analysis of electron spectroscopy data.

PUBLICATIONS

- **Hasti Vahidi**, Alexander D. Dupuy, Benjamin X. Lam, Justin Cortez, Pulkit Garg, Timothy J. Rupert, Julie M. Schoenung, William J. Bowman "Enhanced Electronic Conduction caused by Phase Transformation and Interfacial Segregation in an Entropy Stabilized Oxide" *Advanced Functional Materials* (2024): 15895

- **Hasti Vahidi**, Alejandro Mejia, Shengquan Xuan, Angel Cassiadoro, David Mebane, William J. Bowman "Which Interfaces Matter Most? A Non-monotonic Relationship between Grain Boundary Defect Chemistry and Ionic Conductivity in a Concentrated Solid" (ChemRxiv)
- **Hasti Vahidi**, Komal Syed, Huiming Guo, Xin Wang, Jenna L. Wardini, Jenny Martinez and William J. Bowman "A Review of Grain Boundary and Heterointerface Characterization in Polycrystalline Oxides by (Scanning) Transmission Electron Microscopy" *Crystals* 11.8 (2021): 878.878
- Jenna. L Wardini, **Hasti Vahidi**, Huiming Guo, William J. Bowman " Probing Multiscale Disorder in Pyrochlore and Related Complex Oxides in the Transmission Electron Microscope: A Review" *Frontiers in Chemistry* (2021)
- Huiming Guo, **Hasti Vahidi**, Hyojoo Kang, Soham Shah, Mingjie Xu, Toshihiro Aoki, Timothy Rupert, Juan Luo, Kandis Leslie Gilliard-AbdulAziz, William J. Bowman "Tuning grain boundary cation segregation with oxygen deficiency and atomic structure in a perovskite compositionally complex oxide thin film" *Applied Physics Letters* (2024)

LEADERSHIP EXPERIENCES

- Science Outreach Leader: Designed and led workshops for elementary, middle, and high school students.
- Teaching Assistant: Instructed over 600 undergraduates in 3 lecture and lab classes, presented invited lectures/talks on topics including "Crystallography", designed and graded exams/presentations, demonstrated lab activities.
- Research Mentor: Designed and guided experimental plans for 1 master student and 2 undergraduates, evaluated research results/presentations, mentored students throughout their career.
- Treasurer (American Ceramic Society-Southern California Section): Plan and host events networking events for ceramics-related companies and students such as professional development events and site visits.

HONORS AND AWARDS

- Ph.D. Bridge Fellowship by UCI Samueli School of Engineering
- Goldstein Scholar Award by the Microscopy Society of America
- Geoscience Congressional Visit Day in Washington, D.C. to advocate for science funding
- 3rd place in UCI-MSE elevator pitch competition, Acquired UCI's "Effective Communications for Scientists" and "Science Policy and Advocacy" certificates, Member UCI GPS-STEM Trainee Council

CONFERENCE PRESENTATIONS

- "Structure & Composition of Heterointerfacs in Multiphase High Entropy Oxides" TMS, Anaheim, CA,2022
- "The Influence of Structure and Chemistry of Phases in Enhanced Electrical Conductivity of Multiphase High Entropy Oxides" MRS Solid-state Ionics 23, Boston, MA, 2022
- "Mixed Ionic Electronic Conduction Caused by Phase Transformation and Interfacial Segregation in an Entropy Stabilized Oxide" ECS 244, Gothenburg, Sweden, 2023

ABSTRACT OF THE DISSERTATION

Effect of Grain Boundary Chemical Segregation on Electrical Transport in Complex Oxides

By

Hasti Vahidi

Doctor of Philosophy in Materials Science & Engineering

University of California, Irvine, 2024

Professor William J. Bowman, Chair

The significance of polycrystalline ceramic oxides as material candidates for applications in and beyond electronics, information technology and energy storage/conversion is undeniable. However, to further enhance the functionality and scalability of polycrystalline oxides for real-world applications, considerable efforts have been focused on tuning macroscopic properties including electrical conductivity through the design of new chemistries and structures at atomic scale. Of particular interest, is understanding the role of grain boundary (GB) chemical segregation in electrical conductivity, to engineer effective GBs with improved electrical conductivity. GBs make up a considerable volume fraction of polycrystals, particularly in nano sized grains and have different structure and chemistry and therefore properties compared to that of the grains.

While the influence of GB segregation in electrical conductivity of most binary oxides (containing one cation) and slightly doped, dilute solid solutions (containing < 1 mol% dopant concentration) is extensively studied, there is a noticeable gap in understanding GB segregation behavior in *complex oxides*, which comprise the most technologically important ceramics. In this

work, we thus seek to expand the understanding of GB segregation in 2 different *complex oxides* defined here as *oxides containing 2 or more cation species and more than 1 mol % of each in the lattice,* with the goal of improving GB and total electrical conductivity.

The first part of this work aims to simulate cross-GB oxygen ion (O^{2-}) conductivity in a concentrated gadolinium-doped ceria ($Gd_{0.25}Ce_{0.75}O_{2-\delta}$) model system using the experimentally measured defect distribution profiles near the GB. Using aberration-corrected STEM-EELS and ELNES, we quantify Gd segregation, oxygen vacancy ($V_O^{\bullet\bullet}$) depletion and Ce^{3+} segregation to 5 random GBs. This information is then used to develop a phase field model that calculates defect-defect interaction energies (that were ignored in conventional models for dilute solid solutions), and inputs them to the Martin-Nakayama model, to predict the conductivity across each individual GB. Our results suggest that unlike in dilute solid solutions, where conductivity has a monotonic relationship with the concentrations of $V_O^{\bullet\bullet}$ near the GB, conductivity in a concentrated gadolinium-doped ceria is not solely dependent on the $V_O^{\bullet\bullet}$ concentrations. Instead, conductivity tends to peak when optimal amounts of $V_O^{\bullet\bullet}$ are present. This is a reasonable observation, considering that the interactions between defects (e.g., $V_O^{\bullet\bullet}$ and Gd solutes) influence the mobility and migration of O^{2-}across GBs. In summary, we divide the studied GBs into 2 categories: "*type a*" and "*type b*". Unlike the *type a* GB, which is likely a better O^{2-}conductor with higher $V_O^{\bullet\bullet}$ depletions (~ 0.14 – 0.15 mole fraction which is the optimal amount mentioned above), *type b* GB is likely a poor O^{2-} conductor with lower $V_O^{\bullet\bullet}$ depletions (~ 0.7 - 0.9 mole fractions). It should be noted that both *type a* and *type b* GBs have similar amounts of Gd^{3+} dopant and Ce^{3+} local electron concentrations.

The second part of this work explores the changes in the GB chemistry of a single phase (CoCuNiZnMg)O entropy stabilized oxide (ESO) rocksalt as it undergoes heat-treatment induced phase transformation. We hypothesized that the phase transformations result in changes in the concentrations of charge carrying defects in grains and at the GBs, affecting charge transport properties. Aberration-corrected STEM coupled with EDS and EELS is used to study the phase evolution at atomic-scale, by analyzing one single-phase (ESO-single) and two multiphase ESOs (heat treated at for 2 and 24 h at 700 °C - ESO-2h and ESO-24h). Our findings directly reveal that Cu segregates to the GBs in ESO-single, with homogenous distribution of all cations to the grains. In multiphase ESOs, an enthalpy stabilized Cu-rich tenorite secondary phase forms at some GBs in ESO-2h and at all GBs in ESO-24h. Additionally, Cu-rich tenorite and Co-rich spinel secondary phase particles are found in grains of ESO-24h. Changes in the electrical conductivity are then measured using electrochemical impedance spectroscopy (EIS). No resistivity contribution is detected for the GBs in ESO-single, suggesting that the insignificance of GB space charge potential. Upon heat treatment, the electrical conductivity of grains increases by 2 and 4 orders of magnitude in ESO-2h and ESO-24h, respectively. We attribute this significant enhancement to the formation of additional Cu^{+}/Cu^{2+} pairs in grains introduced by the secondary phases. As hypothesized earlier, the altered GB chemistry plays a significant role in dictating charge transport properties of this ESO by allowing the nucleation and formation of secondary phases. We find that, while the conductivity across GBs covered by tenorite particles is much lower than that of the grains, ESO's total conductivity still experiences a significant increase in this system with ~2-μm average grain size.

CHAPTER 1:Introduction

1.1 *Motivation*

Electricity is undoubtably an essential part of modern society and determines the quality of life on Earth[9]. Today, most of our electricity comes from combusting fossil fuels (e.g., natural gas, coal, etc.) and biomass (e.g., wood, animal residues, etc.). The heat generated from the combustion process is converted to electricity using technologies such as steam boilers or gas turbines. Unfortunately, these processes produce large quantities of carbonous gasses such as CO_2 that are the principal driver of climate change and air pollution[10]. Today, fossil fuels provide about 80% of our global energy and due to the increase in energy use, emissions are expected to rise every year, worsening climate change[11]. Therefore, the innovation and adaptation of technologies that produce electricity with minimal greenhouse gas emissions are critical to mitigate the yearly increase in temperature and stabilize it at 1.5 °C by 2040[12].

Polycrystalline ceramics are key to the newly developed low or net-zero emission technologies such as solid oxide fuel cells (SOFC) and batteries, due to their intrinsic properties such as high thermal, and chemical stability even under severe conditions, low costs, and production scalability. Additionally, while most commercialized ceramics (e.g., cathode materials in Li-ion batteries or gadolinium-doped ceria in SOFC) have not yet reached desired energy generation or storage efficiencies, the flexibility in engineering them to achieve novel functional properties sets them apart from other materials candidates and technologies. As an example, developments and recent progress in solid electrolytes for SOFC are discussed. Fuel cells convert currently available fuels (hydrogen, methane, etc.) to electricity with a higher efficiency than combustion engines, exceeding 60%. While hydrogen polymer exchange membrane fuel cells (PEM FC) only emit water, they rely on the expensive Pt group metal/metal-alloy catalysts which increases the costs and limits their adaptability. On the other hand, SOFC are among the most efficient fuel cells that operate by the oxidation of fuel such as H_2 at anode and reduction of oxygen at cathode[13]. In SOFCs, the solid ceramic-based electrolyte, sandwiched between anode and cathode (Fig. 1.1), is responsible for the conduction of oxygen ions to anode and it the primary reason for higher operation temperatures in SOFC (750-1000 °C) compared to other fuel cells.

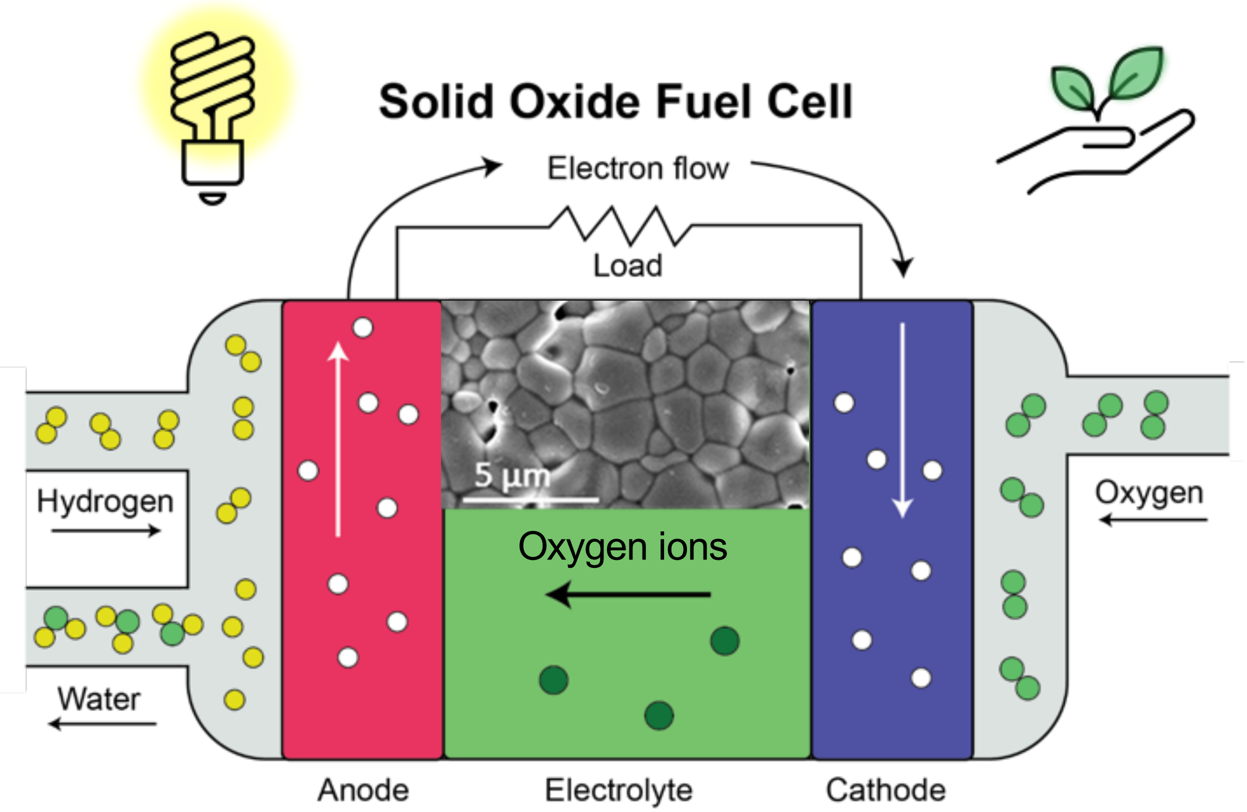

Fig. 1.1. Schematic of a solid oxide fuel cell. Oxidation of fuel happens at anode and reduction of oxygen is shown at the cathode electrode. Electricity is generated in the external circuit.

Even though ceramics are known for high temperature durability, higher operation temperature of SOFC is not ideal and can leads to issues including higher costs, long-term durability concerns and incompatibility with small scale applications, motivating the development of intermediate temperature SOFCs (500-750 °C)[14]. Among candidate electrolytes for intermediate temperatures, gadolinium-doped ceria (GDC) has great electrochemical stability but shows a much higher grain boundary (GB) resistance compared to counterpart yttria-stabilized zirconia (YSZ) or scandia-stabilized zirconia (ScSZ), which adversely impacts SOFC efficiency. In general, GB ionic conductivity in most manufactured electrolytes can be 10^2 – 10^8 times lower than that of grains[4,15,16]. Therefore, significant research has focused on reducing the resistance of GDC GBs via tuning the structure and/or composition through doping, alternative sintering techniques[17], or ion radiation. The challenge to enhance GB conductivity goes beyond SOFC and can play a significant role in other renewable technologies including proton conductors[7] and Li-ion conductors for PEM fuel cells/electrolyzers and Li-ion batteries.[1] An example GB resistive to Li-ion conductivity in a perovskite oxide is shown in Fig. 1.2.

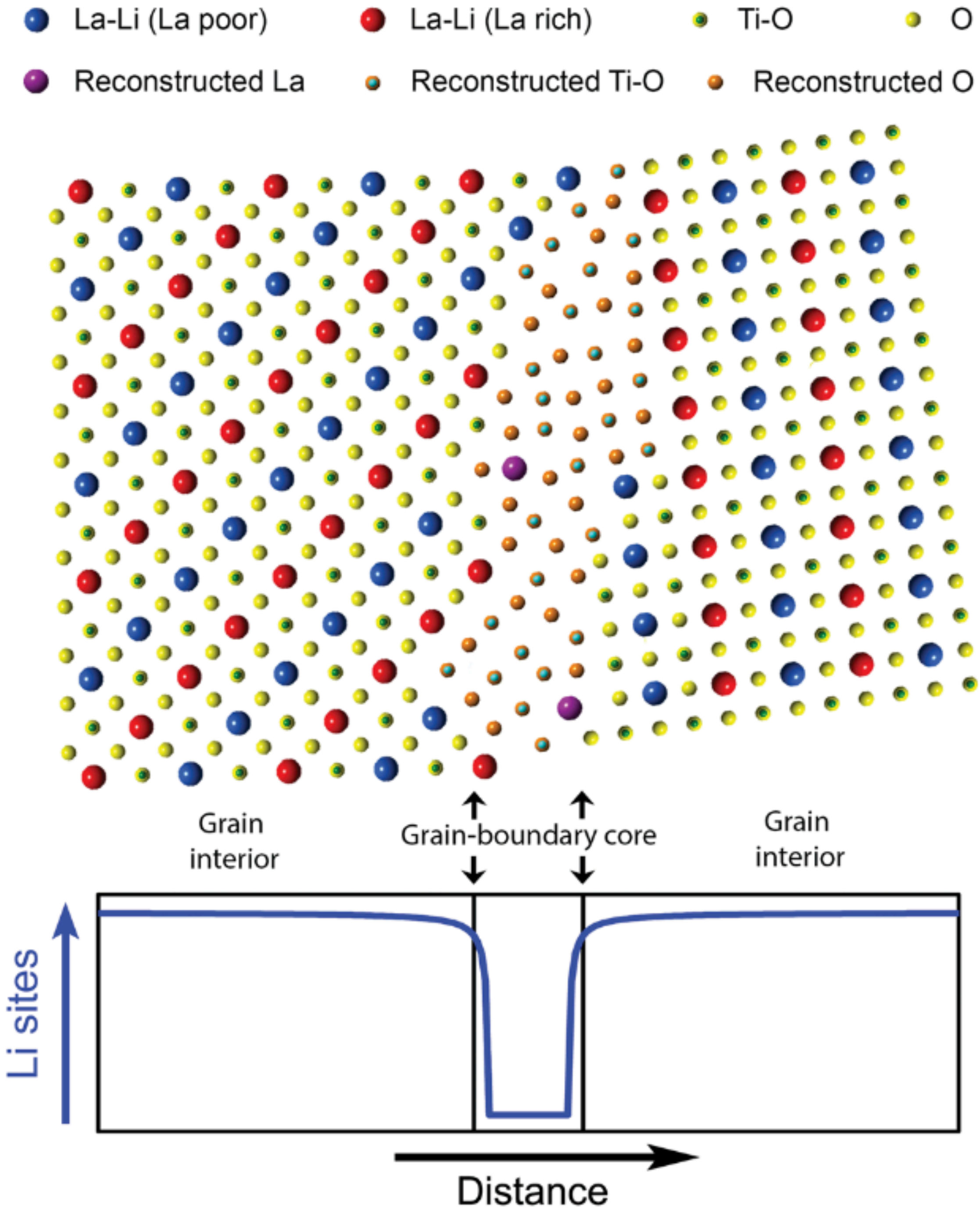

Fig. 1.2. Schematic of the atomic configuration of a specific GB type based on HAASD-STEM images and EELS analysis, along with an illustration of the decreased Li site concentrations at the GB. (Reproduced from Ref.[1])

The study presented in chapter three of this work is motivated by the overarching goal of enhancing the ionic conductivity of GBs in dilute and concentrated (doped) polycrystalline ceramics. A concentrated 25 mole % gadolinium doped ceria is selected as a model system for intermediate-temperature SOFCs and oxygen ion conductivity across individual GBs is predicted using an experimental-computational framework that considers charge carrier distributions measured using transmission electron microscopy and spectroscopy. This information allows for tuning GB conductivity for specific application using synthesis techniques such as spark plasma sintering (SPS) or cold sintering[18] that have proven to control GB chemistry and defect profiles.

1.2 Grain boundary segregation

A GB is an interface where the two grains of same phases (i.e., equivalent stoichiometry and crystal structure) come together. Due to their disordered structure, GBs tend to have a stoichiometry different from that of grains and defect formation energies (such as oxygen vacancies or Schottky point defects) are usually lower in GBs. As a result, segregation of solutes to GBs is a common observation and usually tends to reduce the total Gibbs free energy of the system[19], example shown in Fig. 1.3. Segregation can be an equilibrium or non-equilibrium phenomenon. Equilibrium segregation is based on the intrinsic chemical properties of the system, while the non-equilibrium stems from systems processing and thermal history; for example, coupling of solutes with oxygen vacancies at the GB. Equilibrium segregation is typically driven by factors including the electrostatic potential at the GB space charge layer. Elastic strain energy due to the lattice disorder (variation in size of solute and host atoms/ions) is another driving force, which creates lower energy sites for solutes at the GBs.

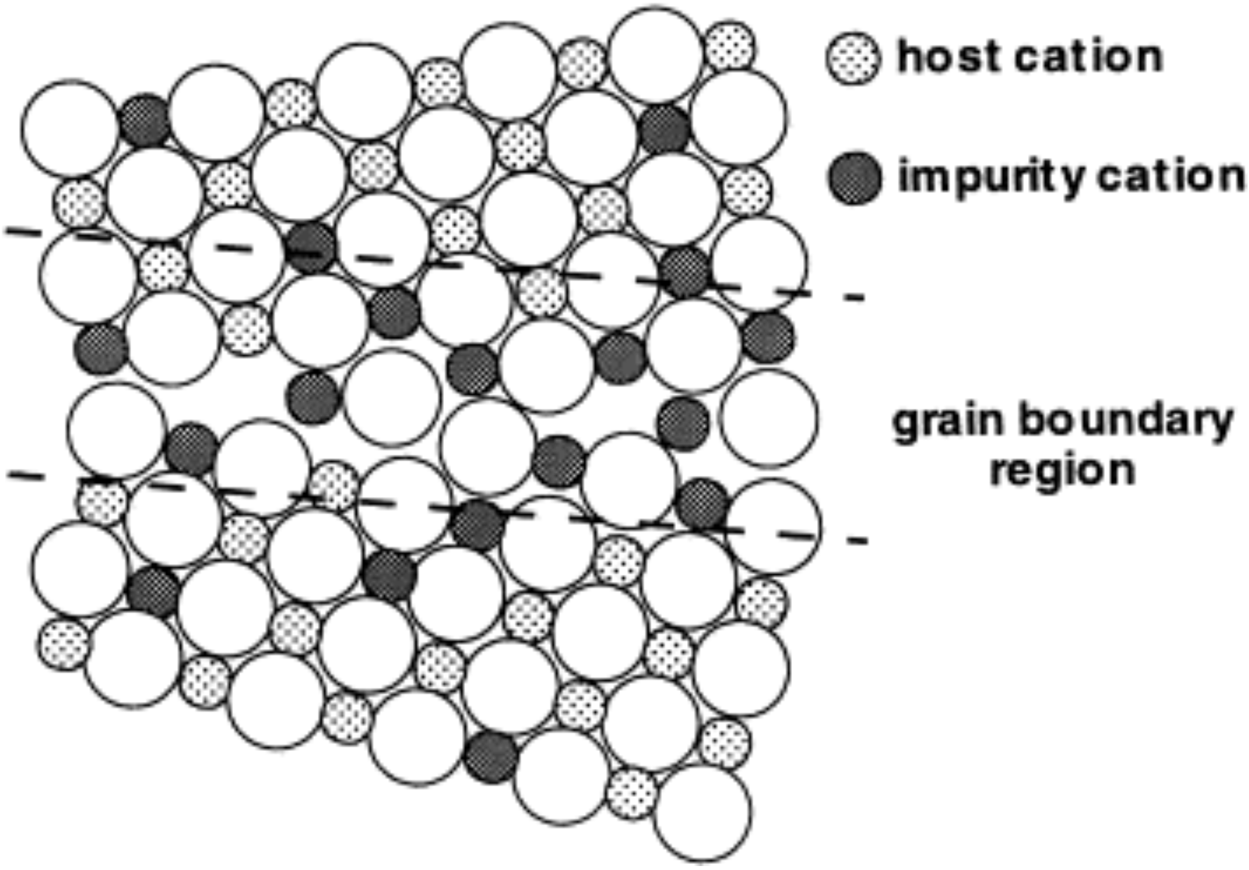

Fig. 1.3. Schematic of GB segregation in a ceramic oxide with dark circles representing segregated solute ions.(Reproduced from Ref.[2])

1.3 *Grain boundary conductivity and space charge layers*

In a polycrystalline material, charge carriers must transport through both grains and across/along GBs, as GBs make up a significant volume fraction of the materials, particularly when grain size is smaller. Due to their structural and compositional deviations from grains, GBs tend to have a different contribution of conductivity, acting as fast or slow conduction pathways. As an example, oxygen ion transport across a polycrystalline zirconia involves oxygen ion hopping via oxygen vacancies through the grains and across the GBs, not along GBs, due to their high resistivity. The high resistivity phenomenon at GBs of such ceramics is attributed to the formation of an intrinsic electrostatic space charge layer (SCL) at GBs[20–22]. It is well-accepted that a high concentration of oxygen vacancies exists at the GB core. Due to the positive charge of these oxygen vacancies, compared to divalent oxygen anions in the grains, a net positive electrostatic potential is created at the GB core, resulting in redistribution of other charges around GB core, forming SCL that are typically a few nm wide. As positive oxygen vacancies at GB core repulse other positive charges, the rest of the oxygen vacancies are depleted from the SCL and are unable to participate in charge transport, ultimately leading to the resistive GBs, which reduce total conductivity. In the case of doped ceramics such as yttria-stabilized zirconia and gadolinium-doped ceria, substitutional solutes with a net negative charge (e.g., Gd^{3+} substituting a Ce^{4+} with a net charge of -1 or $Gd_{Ce}^{'}$ according to Kröger & Vink notations[23]) accumulate near the GBs due to the attractive electrostatic force between positive GB core and negative solute. While the segregation of solutes can adversely impact GB conductivity by increasing conductivity activation energy through increased solute-vacancy interactions, research shows that the concentration or type of segregated solutes be used as tools to alter conductivity by changing the space charge potential[15].

Nowadays, conventional models are available to predict defect concentration profiles near the GB under different space charge potentials such as Mott-Schottky (M-S)[20,24], Gouy-Chapman (G-C)[24] and Poisson- Boltzmann[25]. Fig. 1.4 shows the distribution and concentrations of defects at and away from the GB according to M-S and G-C.

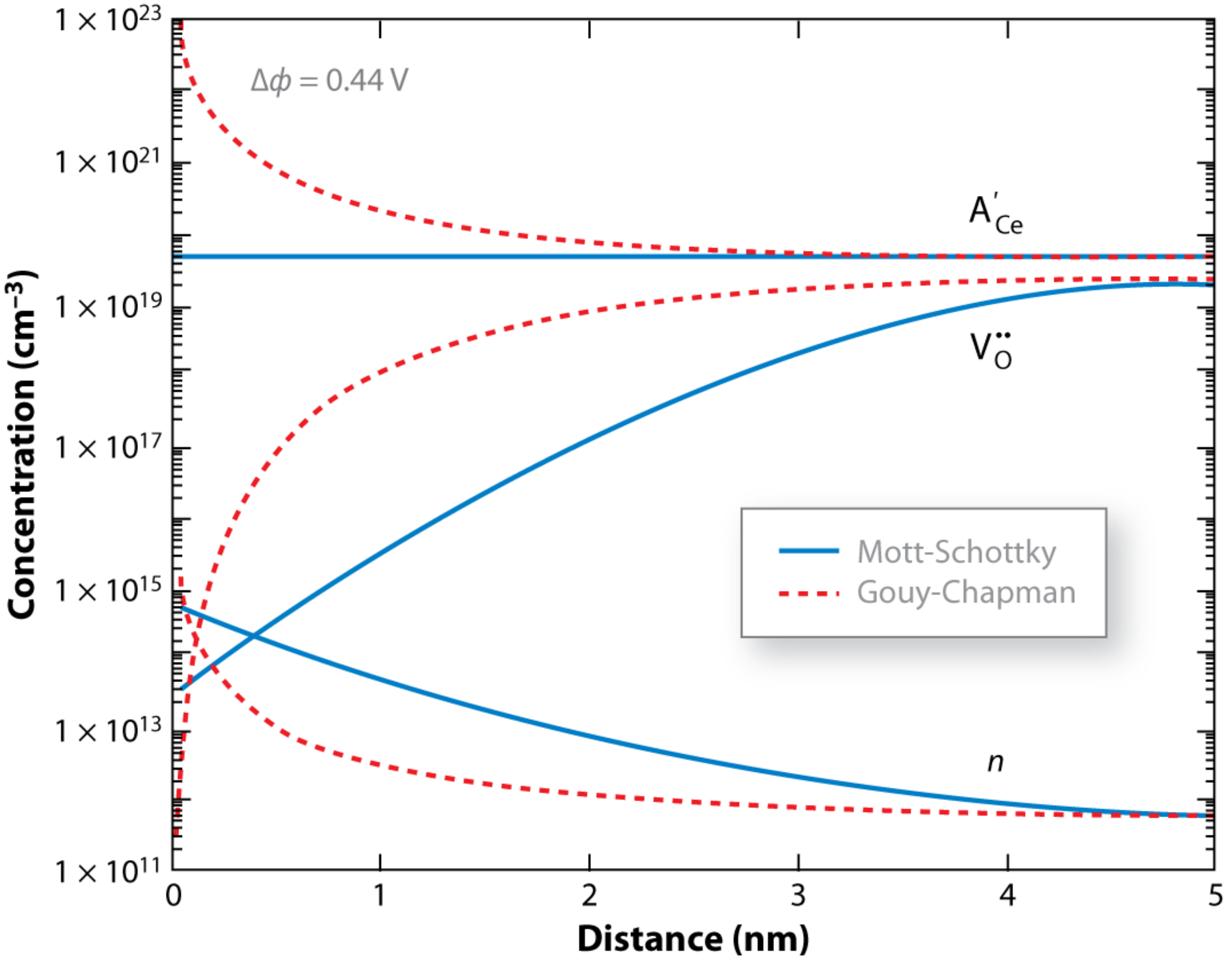

Fig. 1.4. Space charge profiles of acceptor dopant, oxygen vacancies, and electron near a GB interface with a space charge potential +0.44 V, according to both the G-P model and the M-S model. Reproduced from Ref.[3].

However, these models assume a reasonably dilute solid solution (i.e., < 1 mol %) in which defects are not interacting with each other. Therefore, there are uncertainties about the influence of higher-level dopants and there has been effort to include the defect interaction contribution to the models[22,26,27]. Concentrated solid solutions are particularly important as the most useful compositions for solid electrolyte applications and therefore, there is a need for development of theories capable of explaining these regimes as well. It is worth noting that due to limited simulation cell size, it is hard to use DFT for ascertaining point defect distributions in concentrated solid solutions[28].

1.4 Heterointerfaces

A heterointerface (HI) describes an interface between two phases that differ structurally and/or chemically[29]. Fig. 1.5. contains schematic diagrams and BF-TEM micrographs of GBs and HIs in a single phase and a multiphase polycrystalline oxide. GBs/HIs comprise an approximately two-dimensional "core" or "structural" region where the atomic structure deviates from that of both adjacent crystals over ~1 unit cell in the direction normal to the interface plane. A diffuse three-dimensional "space charge zone" or "chemical" region extends up to several nm into adjacent crystals depending on the point defect concentration[30].

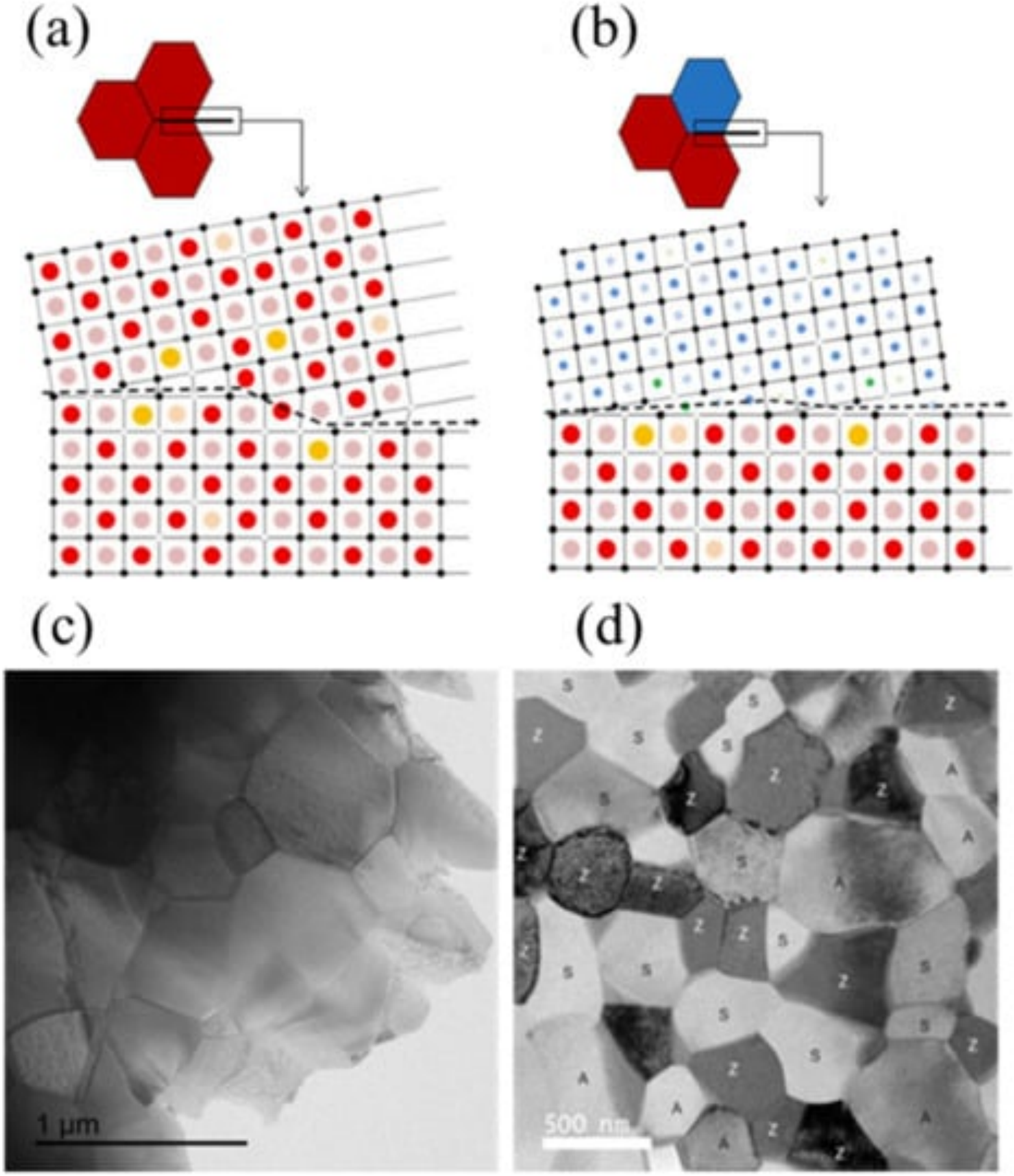

Fig. 1.5. Schematic diagrams of interface between (**a**) same material (GBs) and (**b**) different materials (HIs) at atomic scale (**c**) BF-TEM micrograph of GBs in a polycrystalline Gd/Pr co-doped CeO_2 (**d**) BF-TEM micrograph of HI and GBs in a polycrystalline $MgAl_2O_4$, YSZ and Al_2O_3 multiphase oxide. Grains in red and blue in (**a**, **b**) are depicting different materials with different chemistry and crystal structures for demonstration (Reproduced from Ref.[4–6].

1.5 Entropy stabilized oxides

A grand challenge facing materials science and engineering in the upcoming years is the continuous need to identify new compositions and engineer their properties. Utilizing entropy stabilization as a material design strategy rose from the metal community more than 2 decades ago, to introduce new, potentially useful materials[31,32]. In 2015, this concept was introduced to the ceramics community by Rost *et al* [33]. The newly discovered materials, called high entropy oxides (HEO) are composed of 5 distinct cations sitting in an anion sublattice, forming a single-phase crystal structure with homogenous distribution of cations. Later, entropy stabilized oxides (ESO) were defined as a subset of HEO, in which entropy dominates the enthalpic term and allows for the formation of a single phase, without one or more of the parent constituents. Interestingly, it was shown that ESO can reversibly convert to multiphases, proving the dominance of entropy over enthalpy. Since both HEO and ESO greatly expand the available compositional space and possess promising functional and mechanical properties [34], they are strong candidates for solid electrolytes in batteries, fuel cells/electrolyzers, solid-state electrochemical devices, etc[35–40]. Reasonable electrochemical stability due to the sluggish nature of diffusions and coexistence of active and inactive components during the redox reaction in battery cycling are among the other attractive properties of these materials [41,42]. In addition to oxides, other high entropy systems such as carbides [43–46], borides [47–49] and nitrides [50–52] have been the topic of interest of several studies. Entropy stabilization can form unique and long-range crystal structures and local compositional disorder in the lattice[1]. In oxides with O-M-O-M bonds, factors such as the M cation coordination number, bond length, angle, energy, degree of covalency, and vibration frequency are influenced by compositional complexity imposed through the distribution of M cations, allowing tunability of functional properties, such as thermoelectric[2], dielectric[3],magnetic[4], electronic[5], ionic[6], thermal conductivity[7], and catalytic activity[8] that are useful in energy storage and conversion[9,10].

1.6 Scientific Problem and Research Objectives

Grain boundaries (GB) play a determining role in the macroscopic functional and mechanical properties of polycrystalline materials including ceramic oxides, as elaborated in previous sections. Large scale production of such materials is relatively easy and cheap compared to single crystals synthesis or thin film deposition. Unfortunately, most existing grain boundaries in ceramics negatively influence the overall properties, a phenomenon known as GB effect, which limits the functionality and adaptation of technologies that heavily rely on polycrystalline ceramic oxides. It is noteworthy that there are GBs with enhanced properties observed in some polycrystals as well. As a result, scientists and engineers have spent decades on understanding the GB effects in many material systems, with the goal of enhancing GB properties. This can be done using structural or compositional tuning through a variety of ceramic processing and sintering methods. Such findings can lead to the creation of a new era of material design and large-scale production of polycrystalline ceramic oxides for aerospace, automotive, energy storage and conversion, defense and more. In addition, the significance of this research is not limited to conventionally sintered polycrystalline ceramics, as GBs are commonly seen in ceramic thin films and can influence their properties and applicability in multilayered micro-devices.

Additionally, the concept of GB engineering, once established, can be applied to tailor the properties of many other interfaces in materials and devices such as heterointerfaces in multiphase materials and interfaces between multilayer devices such as solid-state batteries[53] and microelectronics[54].

However, big problem requires bigger solutions. While the extensive body of research so far has led to novel discoveries, there is still room for improving our understanding of grain boundaries, particularly with respect to *complex oxides.* The term *complex oxide* used throughout this dissertation refers to *oxides with 2 or more cation species and more than 1 mol % of each in the lattice*. The grain boundaries in so-called complex polycrystalline oxides are more difficult to analyze, predict and improve due to the existing of more constituting elements and possibly point defects.

This work attempts to bridge this gap in the literature through synthesis, characterization, and modeling of GBs in complex polycrystalline oxides. Two promising and different complex polycrystalline oxide model systems (gadolinium-doped ceria and (Co,Cu,Mg,Ni,Zn)O entropy stabilized oxide) are selected and synthesized via conventional and spark plasma sintering (SPS). Due to the fine nature of these interfaces, useful characterization techniques are limited to a few with high enough resolution and efficiency. Here, the role of GBs and grain structure and composition in charge transport/electrical conductivity is investigated by scanning/transmission electron microscopy (S/TEM) coupled with spectroscopy (EDS and EELS) as well as electrochemical impedance spectroscopy (EIS) (see methods in chapter 2). STEM enables offer unique capabilities for such explorations in polycrystalline oxides by enabling qualitative and quantitative analysis of structure and chemistry down to the atomic scale. EIS enables resolving GB electrical conductivity. The findings of this work can expand our knowledge on transport phenomenon in many materials systems and help design defect chemistry in a way that meets the needs for energy storage and conversion.

Despite the similarities in the two material systems and exploration techniques used, each project involves a unique investigation approach, covering different aspects of GB analysis, yet with one cohesive goal of enhancing GB properties for future applications not limited to solid electrolytes in solid-state batteries and fuel cells, oxygen sensors, membranes, and thermal barrier coatings. Detailed research objectives of each project are provided below:

Project 1: Gadolinium-doped Ceria

This project involves the synthesis and characterization of a 25 mol% gadolinium-doped ceria with fluorite crystal structure as a concentrated solid-solution. Five randomly selected GBs are probed vis STEM/EELS to measure the atomic concentration of charge carrying point defects (Gd^{3+} solutes, electrons localized at Ce^{3+}, and $V_O^{\bullet\bullet}$) across each boundary. Each measured set is put into a phase-field model that calculates defect-defect interaction (ex. oxygen-vacancy-dopant) energies and incorporates them into the Martin-Nayakama model for conductivity prediction[55]. So far, limited research has been done on the influence of defects-defect interactions in GB conductivity, which is a significant factor for complex polycrystalline oxides with high concentrations of dopants (> 1 mol%) or high number of cation configurations, that are the most technologically relevant solids. We hypothesize to find a relationship between defect concentrations and predicted conductivity values at each individual GB. The findings will enable the optimization of total conductivity through engineering GB chemistry by sintering and processing routes, such as spark plasma sintering, cold sintering, or ion beam radiation.

Project 2: (Co,Cu,Mg,Ni,Zn)O Entropy Stabilized Oxide

This work focuses on measuring charge transport in an entropy stabilized oxide (ESO) as it undergoes heat treatment induced phase transformation. Single-phase ESOs were synthesized via solid-state powder processing and spark plasma sintering. Two specimens were heat treated for 2 and 24 h at 700 °C, to undergo phase transformation. The composition and structure of each ESO sample was explored via S/TEM EDS and EELS. EIS was used to identify the electrical conductivity and conductivity activation energy. We hypothesize that GBs play a role in stabilization of single phase by accommodating cation species that may reduce to the GB. The segregation of some cations to the GBs can cause a noticeable GB space charge potential and influence GB conductivity. As the ESO undergoes phase transformation, GB's role in conductivity may change, due to potential accommodation of second phase particles in the GB, that can influence defect chemistry. This is the first work focusing on composition and conductivity of GBs in ESOs and will shed light on the nature of GBs in ESO, with specific focus on their role on electrical conductivity. The results of this work allow for tuning single and multiphase ESOs with superior functional performance.

CHAPTER 2:

2.1 Material Fabrication

2.1.1. Co-precipitation Particle Synthesis

Nanocrystalline ceramic particles can be synthesized using various routs. Particles prepared via soft chemical routes, including co-precipitation and sol-gel methods co tend to have smaller sizes leading to higher densification kinetics and sinterability[56]. Particle size is shown to have a significant role in the densification process of sintered ceramics[57]. The co-precipitation and sol-gel methods are commonly used for synthesis of nanoparticles. In each method, different parameters like pH, reaction temperature and time, concentration of the initial solution play an important role particle shape and size. Both methods require dissolving appropriate amounts of metal nitrates in deionized water followed by the addition of a complexing agent such as ethylene glycol ($C_2H_6O_2$). Unlike in aqueous sol-gel[58], the reaction and solution environment lead to formation of a gel, co-precipitation[56] requires the stirring the solutions for several hours, leading to precipitation of particles, that will then be filtered and washed properly.

2.1.2. Conventional and Spark Plasma Sintering

Conventional sintering ceramic particles involves consolidation of particles by heating the green body to high temperatures for long times below the melting point, in which separate particles diffuse to the neighboring particles and bond together. Reduction of particle surface energy by minimizing air-particle interfaces is the driving force for sintering process. Since sintering is a diffusion process, it often requires several hours to allow for particle diffusion in solid-state form. As a result of sintering, pores formed in the green body tend to shrink or close, leading to densification of bulk ceramic with enhanced mechanical properties.

To enhance the densification process of ceramics and control microstructural features such as grain size, advanced sintering techniques are invented that use additional external forces for sintering. Among these methods, park plasma sintering (SPS) utilizes uniaxial force and a pulsed direct electrical current (DC) under low atmospheric pressure to speed up the consolidation of the powder, achieving enhanced densification in short periods of time (a few minutes)[59,60].

2.2 *Electrical Characterization*

2.2.1. AC- Impedance Spectroscopy (AC-EIS)

Electrical conductivity is the migration of charged species through a medium and can be calculated using the following general equation:

$$\sigma = n \cdot q \cdot \mu \qquad \text{Eq. 2.1}$$

Where n is the concentration of charge carrier, q is the charge of the charge carrier and μ is the mobility of charge carrier in the environment that depends on factors such as concentrations of charged and neutral species in the environment and temperature. In ceramic oxides, mobile charged species are often positively or negatively charged ions such as Li^+ and O^{2-} or localized electrons or holes (also known as small polarons) that hop through an oxide lattice via defects including oxygen vacancies[61] (example is O^{2-} conductivity in gadolinium-doped ceria) or transition metals cations with more than one available oxidation state[62] (example is Ce^{3+} localized electron in ceria).

In a polycrystalline ceramic, the total electrical conductivity (ion or localized electron/hole) comprises conduction through grains and across GBs (in the case of GBs being highly resistive). GBs tend to have several orders of magnitude difference in conductivity from that of grains. Less often, GBs have a higher conductivity than that of the grain, resulting in conduction through the GB network. The conductivity of a polycrystalline ceramic can be measured using ac-electrochemical impedance spectroscopy (AC-EIS), assuming the microstructure consists of fully dense arrays of cubic grains separated by uniform GB layers, Fig. 2.1. This strategy or the so-called *brick layer model* has been extensively used in literature[63,64] and considers grain sizes with an average width of *G* and GBs with a uniform thickness of *g*. In this model, GBs are either arrange perpendicular or parallel to the conduction direction.

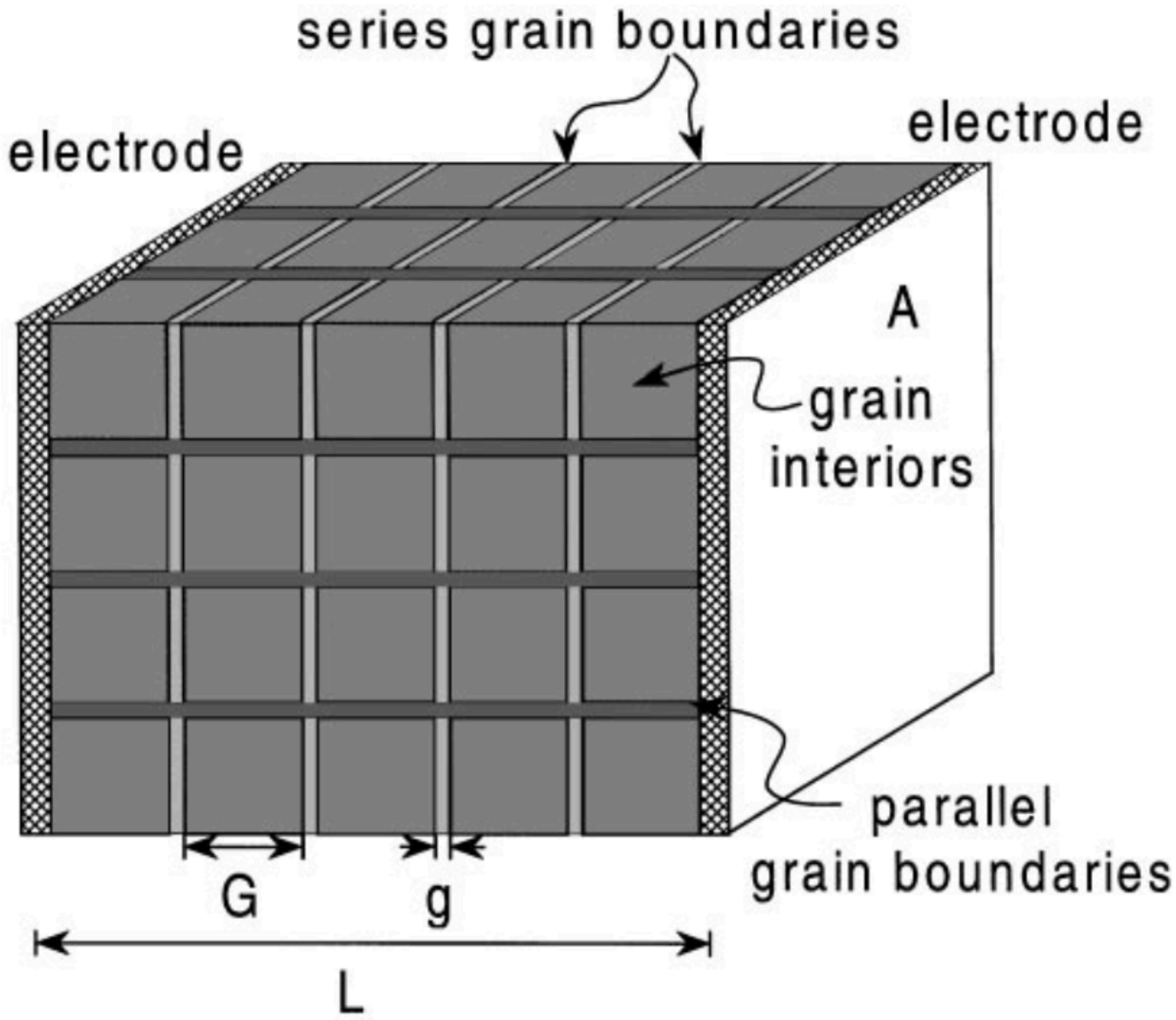

Fig. 2.1. Schematics of brick layer model for measuring the conductivity of polycrystalline solids with grains (grain interiors) depicted as cubes with a width of G and GBs depicted as uniform layers with a thickness of g. Reproduced from Ref.[7].

In AC-EIS, an AC voltage of E_t with signal amplitude of E_0 and radial frequency of $\omega = 2\pi f$ is applied to the sample, inducing a current of It that is out of phase with E_t by phase angel φ as can be seen below:

$$E_t = E_0 \, sin(\omega t) \qquad \text{Eq. 2.2}$$

$$I_t = I_0 \, sin(\omega t + \varphi) \qquad \text{Eq. 2.3}$$

The impedance of the sample, *Z*, can be defined as:

$$Z = \frac{E_t}{I_t} = \frac{E_0 \, sin(\omega t)}{I_0 \, sin(\omega t + \varphi)} = Z_0 \frac{sin(\omega t)}{sin(\omega t + \varphi)} \qquad \text{Eq. 2.4}$$

Assuming Z_0 is the magnitude of impedance and based on Euler's relationship, *Z* can be written as:

$$Z(\omega) = \frac{E_t}{I_t} = Z_0 \, exp(j\varphi) = Z_0(cos\,\varphi + j\,sin\,\varphi) \qquad \text{Eq. 2.5}$$

When plotting the real and imaginary components of impedance or Z_{real} and $Z_{imaginary}$ in x and -y direction as a function of frequency yields a spectrum called a Nyquist plot, that helps to present and extract impedance information from the sample. Nyquist plots usually contain a series of arcs each of which correspond to impedance response of an electrically independent component of the sample, see Fig. 2.2.

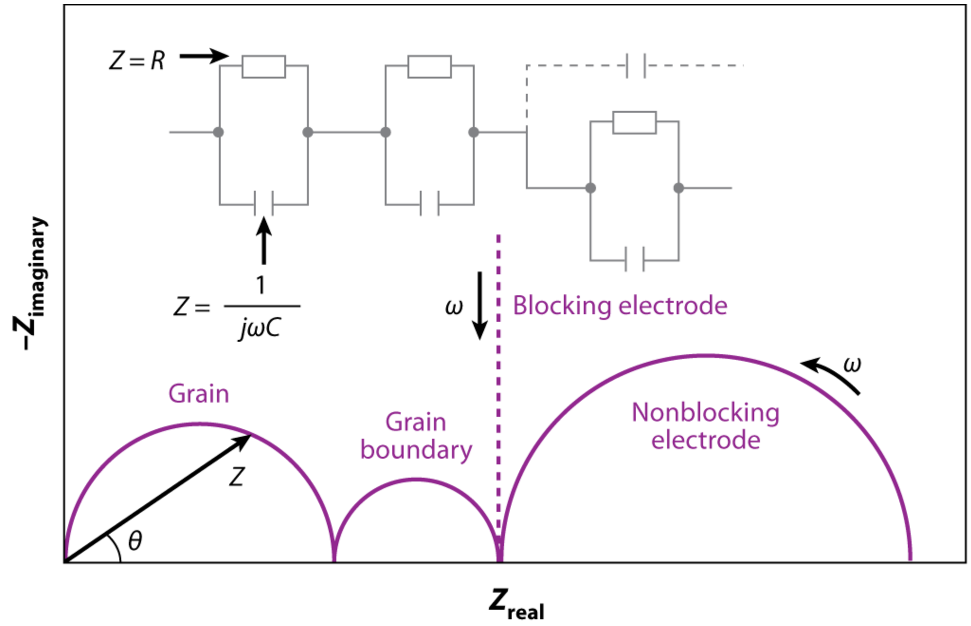

Fig. 2.2. A typical impedance spectrum for a solid with GBs and blocking (or partially blocking) electrodes. The equivalent circuit model shown with definitions of impedance for a resistor and a capacitor. Reproduced from Ref.[3].

In a polycrystalline sample, the arcs are usually attributed the grain, GB, and electrode. To determine the conductivity values of each of these components, a Nyquist plot is fit to an equivalent circuit model with elements that mimic the electrical response of each component and are connected in series or parallel. The equivalent circuit model in this case typically contains a single resistor in series with 2 parallel resistor-constant phase elements (CPE) subcircuits. A CPE is a non-ideal capacitor which has an uneven distribution of charge alongside the capacitor. CPE has an impedance given by Eq. 2.6. where Q denotes the CPE:

$$Z_Q = [(j\omega)^\alpha Y]^{-1} \qquad \text{Eq. 2.6}$$

Where α and Y are constants. α ranges between 0 – 1 and is experimentally found to be closer to 1, suggesting that CPE behaves like a capacitor. Each RQ pair in the model represents an independent phase/component in terms of impedance behavior. These components can either correspond to grain, GB, or electrode. Eq. 2.7. was used to calculate grain conductivity:

$$\sigma_{Grain} = RA \cdot L^{-1} \qquad \text{Eq.2.7}$$

To determine the GB conductivity based on the derivation of *brick layer model,* the ratio of the microstructural data (*G*: average grain width and *g*: GB thickness) can be used. If not available, the ratio of the geometric capacitance of grain and GB (C_{Grain} and C_{GB}) can be used[65]. The geometric capacitance values can be determined from the capacitance values measured from the Nyquist plot. The GB conductivity can be determined using Eq. 2.8:

$$\sigma_{GB} = \frac{L}{A}\frac{1}{R_2}\left(\frac{C_1}{C_2}\right) \qquad \text{Eq. 2.8}$$

Where C_1 is the geometric capacitance of grain and C_2 is the geometric capacitance of GB.

2.2.2. Conductivity Activation Energy

The activation energy of conductivity is shown with Ea and can be calculated for grain and GB using the slope of Arrhenius plot of *Ln(σT)* as a function of *1/T* using the following equation:

$$\sigma T = \sigma_0{}^{\frac{-Ea}{kT}} \qquad \text{Eq. 2.9}$$

2.3 Physical Characterization

2.3.1. X-Ray Diffraction (XRD)

X-ray diffraction (XRD) is a powerful tool for identification of crystalline phases and structures in materials. It is widely used in research and across many industries. In addition to phase and structure, other useful information can be obtained from XRD including stress measurements and texture or orientation analysis. The XRD technique shines x-ray beams through the materials, bouncing off the atoms in the structure, which changes the direction of the beam at some different angle from the original beam. This angle is called the diffraction angle, and it is caused by constructive interference as when beams. The angel of diffraction can be used to determine the differences in atomic planes or *d* using Braggs law:

$$n\lambda = 2d\sin\theta \qquad \text{Eq. 2.10}$$

Where λ is the wavelength theta is the angle of diffraction, d is the distance between atomic planes. The distance between atomic plates can then be used to determine composition or crystalline structure.

2.3.2. Scanning Electron Microscopy (SEM)

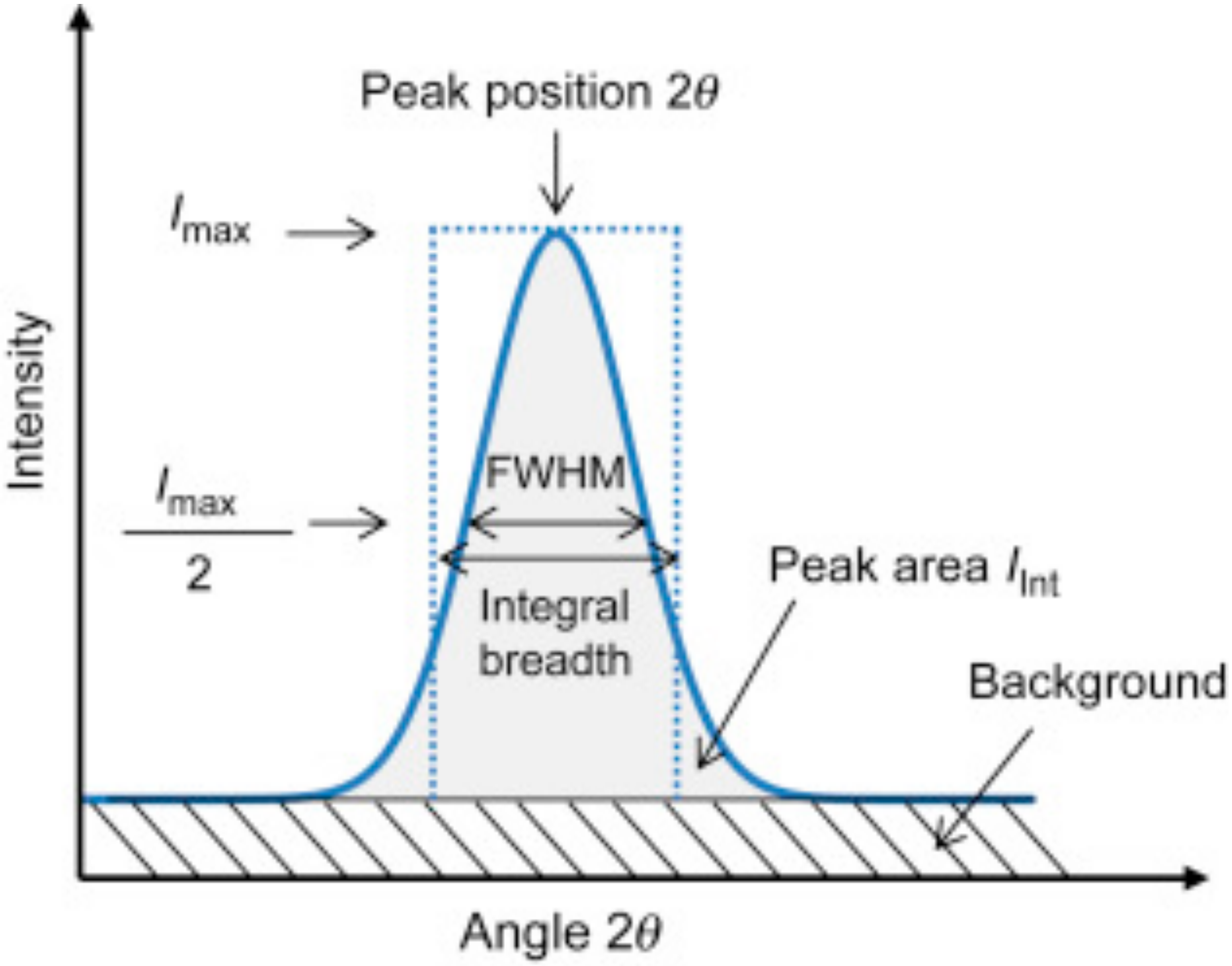

Fig. 2.3. X-ray diffraction diagram showing a diffraction peak and information content that can be extracted. From Ref.[8].

Scanning electron microscopy (SEM) is a technique used to image and analyze the microstructure, surface of materials using the electron beam. In SEM, an electron beam is focused to a spot and is scanned sequentially across the area of interest in the sample. Due to the interactions of electrons, different signals are emitted from the specimen which can be collected by various detectors. Intensities of signals collected from each specific location are used to modulate a pixel corresponding to that location and the combination of those pixels form an image[66].

2.3.3. Focused ion-beam (FIB)

Focused ion beam (FIB) combined with SEM (FIB/SEM) is a powerful tool used for preparing thin material specimens for analysis in a TEM[67]. One of the major methods for TEM sample preparation in an FIB/SEM is the *lift-out technique*. This technique involves preparing a thin layer or lamella of the material by removing the material in the sides via ion beam bombardment with certain voltage and energy. This is followed by lifting the prepared lamella using an omni probe as viewed via SEM and FIB images. The lamella is finally transferred from the probe to a TEM grid and thinned by bombardment of lower energy ions. Once electron transparent, the grid that can be taken to a TEM column.

2.3.4. Scanning/Transmission Electron Microscopy (STEM)

Transmission electron microscope (TEM) and scanning TEM (STEM) are powerful tools for directly imaging atomic arrangements, and quantitative chemical analysis down to the atomic scale. Several books and review articles are written focusing on TEM[68], STEM[69,70], and the various analytical techniques available in both[71–73]. A basic introduction to these techniques *as they pertain to GB characterization in polycrystalline oxides is provided here.* In general, TEMs can be configured to operate in multiple modes. In “TEM mode” (also called conventional TEM) a broad electron beam provides parallel illumination to the specimen. In “STEM mode” the electron beam is converged to a point (or “probe”) by pre-specimen electromagnetic focusing lenses and scanned in a raster pattern over the specimen. Today, a variety of analysis techniques are available to probe important characteristics and functionalities of organic and inorganic specimens in solid, liquid, and gas phases. Here, we highlight various imaging, diffraction, and spectroscopy techniques suited to characterize interfaces within polycrystalline ceramics, such as atomic resolution imaging, microstructure analyses (e.g., grain orientation mapping), and chemistry mapping (e.g., elemental concentration and chemical segregation).

2.3.5. Imaging and Selected Area Electron Diffraction (SAED)

Due to the wavelike nature of electrons and periodic arrangement of atoms within a crystalline specimen, electrons scattered from the specimen generate a diffraction pattern that contains rich crystal structure information. From the position and symmetry of the diffraction spots, it is possible to determine the crystal structure, unit-cell parameters, lattice type, defects such as twinning, while the intensities of the diffraction spots are related to the arrangement of atoms within the unit cell[74]. Selected-area electron diffraction (SAED) is the most used method to acquire this information, and it requires the microscope to operate in “diffraction mode. The information contained in the diffraction pattern is also contained in the image However, the TEM image displays this information in real space while the diffraction pattern represents this information into reciprocal space, the two are related through a Fourier transform. Depending on the application, one or the other representation may prove to be more useful.

A SAED pattern is acquired by isolating a small area of the specimen for diffraction analysis with an area-limiting aperture (usually 0.1 um or greater). In addition to crystal structure determination, the SAED pattern also contains information about overall pellet crystallinity and can be used to establish orientation relationships between multiple diffracting crystals (e.g., between precipitates and a host matrix, or at an interface like GB). On the other hand, widely used techniques such as bright-field (BF) and dark-field (DF) TEM imaging rely on filtering information from the SAED pattern to either exclude (BF-TEM) or preferentially select (DF-TEM) diffracted beams for image formation, generating contrast based on whether a particular region does or does not meet the Bragg condition. In the case of apertureless imaging, the transmitted and diffracted intensities recombine, and the diffraction contrast is suppressed, while the BF and DF TEM images show much better diffraction contrast due to the coexistence of large intensity in transmitted beam and large loss of intensity in the diffracted beam, and vice versa. For example, heavier phases tend to be darker in BF and brighter in the DF mode. While the BF-TEM helps learn about the morphology of the sample, DF can provide information about nanocrystal size and distribution in addition to defects such as dislocations, stacking faults and twinning.

In STEM mode, the electron beam is converged to form a probe and scanned across the specimen. Imaging in the STEM is done primarily using elastically and inelastically scattered electrons which have interacted with, and passed through a thinned section of material, usually <300 nm. The scatter collection angle is critically important for image interpretation. The main imaging modes in STEM are explained below in the order of high to low scattering collection angles. They are often collected simultaneously and can be coupled with EELS and EDS analysis, which are explained below.

2.3.6. Electron Energy-Loss Spectroscopy (EELS)

EELS is the analysis of the energy distribution of electrons that have lost energy through inelastic scattering while passing through an electron transparent sample[75,76]. There are two general types of EELS in S/TEM, both of which rely on the fact that inelastically scattered electrons have kinetic energy corresponding to the energy lost, and that they can be dispersed in space by passing through a magnetic field, i.e., an energy-loss spectrometer. The first is energy-filtered imaging, known as energy-filtered TEM (EFTEM)[72], in which electrons having lost a relatively narrow range of energy (e.g., ~5 eV) are filtered out of the transmitted beam and used to form a real space image. The specific amounts of energy form a real space image. The second is parallel EELS, where all electrons having lost a relatively large range of energy (e.g., <2000 eV) are dispersed onto a detector plane and typically analyzed further in terms of a one-dimensional spectrum of counts versus energy loss. Both provide spatially resolved information about chemical composition and electronic structure, though parallel EELS is currently more commonly used because an entire EELS spectrum can be recorded at specified locations in a S/TEM specimen, potentially providing a rich set of data containing information about specimen thickness, chemical composition, and electronic structure of multiple elements simultaneously.

EELS is now incorporated into S/TEMs that typically operate using high energy electron (60–300 kV) sources. The interactions between electrons and matter are either elastic (approximately zero energy loss) or inelastic (finite energy loss), providing various information about the sample. Elastic scattering involves Coulomb interactions with the atomic nuclei, while inelastic scattering refers to the interactions between a fast incident electron and the atomic electrons that surround the nucleus. Inelastic processes can be understood in terms of the energy band theory[77].

The zero-loss peak (ZLP) represents electrons that are transmitted without losing measurable energy, including electrons scattered elastically and those that excite phonon modes, for which the energy loss is less than the experimental energy resolution (in conventional EELS systems). While the ZLP does not contain spectroscopic information about the specimen, it is useful for energy calibration of the loss spectrum, deconvolution of plural scattering in thicker specimens and determining local thickness. The high-loss electrons are related to the core binding energy, and therefore provide both qualitative and quantitative chemical information, as the intensity of each edge corresponds to the quantity of electrons generating a specific energy. In addition to the core-loss edges, the first 30–40 eV beyond each edge is related to the change in density of unoccupied states, which affects the electron loss near edge structure (ELNES), or fine structure[78,79].

2.3.7. Energy-Dispersive X-Ray Spectroscopy (EDS)

EDS is a powerful qualitative and quantitative analytical technique available in S/TEM used for chemical analysis of a desired specimen. The technique relies on the X-rays generated in the microscope due to the interaction between the electron beam and sample. Two different types of X-ray signals are generated: Bremsstrahlung X-rays and Characteristic X-rays. Bremsstrahlung or braking radiation results from the deceleration of primary beam electrons when deflected by the atomic nuclei in the sample. The characteristic X-rays are a result of sample atoms being ionized by the primary electron beam. Simply, a core-shell electron is excited and ejected from the atom, while an outer-shell electron replaces it; this energy difference is released as an X-ray. These characteristics X-rays are like fingerprints for each element and as a result, EDS spectra are very useful to determine elemental composition of any sample[80].

CHAPTER 3: Which Interfaces Matter Most? Variability in Grain Boundary Defect Chemistry and Conductivity in a Concentrated Solid Electrolyte

3.1 Contributions and Acknowledgements

Authors list: Hasti Vahidi[a]*, Alejandro Mejia*[b]*, Shengquan Xuan*[a]*, Angelo Cassiadoro*[b]*, David Mebane*[b] *and William J. bowman*[a*]

[a]*Department of Materials Science & Engineering, University of California, Irvine, CA USA*
[b]*Department of Mechanical and Aerospace Engineering, West Virginia University, WV USA*

Detailed information: WJB and DM conceptualized the experimental and computational work, respectively. HV fabricated the samples, performed the EIS conductivity measurement, and collected and analyzed the STEM EELS characterization data. SX analyzed and interpreted the EIS data and compiled the literature transport data. AM, DM, AA, and AC modeled and predicted GB defect chemistry and conductivity values. WB, DM, HV and AM contributed to the interpretation and discussion of the results. HV, WJB and DM drafted the manuscript and all authors reviewed and revised the final manuscript.

Acknowledgements: HV and WJB acknowledge primary support from the UCI new faculty startup funding. This research was partially supported by the National Science Foundation Materials Research Science and Engineering Center program through the UC Irvine Center for Complex and Active Materials (DMR-2011967). We acknowledge the use of facilities and instrumentation at the UC Irvine Materials Research Institute (IMRI) supported in part by the same NSF MRSEC (DMR-2011967). AM, DM, and AC acknowledge funding from the NSF (CBET-1705397) and the WVU Research Computing Thorny Flat HPC cluster for providing computational resources for the numerical modeling work, which is funded in part by NSF OAC-1726534.

3.2 Chapter Summary

High-conductivity solid electrolytes are critical components of solid oxide fuel/electrolysis cells, solid-state batteries, information storage devices, and other electrochemical systems. Like many electrolytes, polycrystalline $Gd_xCe_{1-x}O_{2-\delta}$ (GCO) can suffer from low grain boundary (GB) conductivity relative to grain interiors, attributed to local nanoscale oxygen vacancy ($V_O^{\bullet\bullet}$) depletion which diminishes cross-GB ionic conductivity. To improve conductivity, microscopic analyses of GB structure and chemistry along with multiscale computational models are needed to accurately relate nanoscopic point defect concentrations to macroscopic ionic conductivity. Here, we present an experimental-computational framework that predicts which GBs in a polycrystalline electrolyte likely facilitate ionic conductivity. We developed a thermodynamic phase-field modeling framework and applied it to a model high-solute-content oxygen electrolyte $Gd_{0.25}Ce_{0.75}O_{2-\delta}$, wherein the microscopically measured GB-to-GB variability in defect concentrations was used to predict the GB-to-GB variability in cross-GB ionic conduction. Uniquely, our model prioritizes reproducing microscopically observed GB defect distributions and considers defect-defect interactions in highly concentrated solid solutions, making the framework applicable to most technologically relevant solid electrolytes. Across the GBs studied, we revealed a non-monotonic relationship between $V_O^{\bullet\bullet}$ depletion and GB conductivity, with the highest conductivity predicted for intermediate $V_O^{\bullet\bullet}$ depletion amount.

3.3 Introduction

Inorganic solid electrolytes with fast ionic conductivity are critical components of fuel/electrolysis cells, all-solid-state batteries, membrane and separation reactors, sensors and other electrochemical devices[22,27,81–88]. For example, solid oxygen ion (O^{2-}) conductors are used in solid oxide fuel/electrolysis cells (SOFCs/SOECs) for high-efficiency conversion between chemical and electrical energy and chemical production from CO_2. For these applications, yttria-stabilized zirconia (YSZ) is a widely used solid electrolyte partly due to its high O^{2-} conductivity at high temperatures (800-1000 °C), facilitated by hopping oxygen vacancies ($V_O^{\bullet\bullet}$) which charge compensate Y^{3+} acceptor solutes in YSZ[89–91]. However, high operating temperatures are problematic as they speed electrochemical cell degradation and increase cost, motivating the development of highly conductive O^{2-} conductors at lower temperatures. Gadolinium cerium oxide (GCO, $Gd_xCe_{1-x}O_{2-\delta}$) is a popular alternative to YSZ and a model system that exhibits higher O^{2-} conductivity and reasonable chemical stability < 700 °C[92–94].

Like other solid electrolytes, polycrystalline GCO can suffer from low grain boundary (GB) conductivity relative to grain interiors[18,95,96]. This was initially attributed to highly resistive silica-based glassy impurity phases[97]. However, once observed in samples without glassy GB phases, high GB resistivity was attributed to the formation of intrinsic space charge layers (SCLs) directly adjacent to GB cores[98–100]. SCLs form due to discontinuous crystallinity at GB cores accommodated by $V_O^{\bullet\bullet}$—whose lower formation energy in the core increases their concentration, resulting in both the segregation of charge compensating acceptor solutes from grain interiors (when sufficiently mobile) and $V_O^{\bullet\bullet}$ depletion in the SCL, diminishing cross-GB conductivity[101,102]. Several strategies have been explored to improve GB conductivity by mitigating the SCL effects, such as engineered solute segregation to GBs to counteract the core charge via conventional solid-state synthesis[103], cold sintering[18] or photoelectron-mediated reduction of the GB space charge potential[104].

Persistent barriers to elucidating the impact of SCLs on fast ion conduction in polycrystalline ceramics are the requirement for high spatial resolution experimental probes and the lack of comprehensive thermodynamic models describing both microscopic GB characteristics (e.g., electrostatic potential and defect concentrations) and cross-GB ion transport. For example, accurate GB characterization often requires nano- or atomic-scale imaging, spectroscopy, and/or holography by scanning/transmission electron microscopy (S/TEM), atom probe tomography (APT), or Kelvin probe force microscopy (KPFM) [84,85,103,105,106]. In dilute solution solid electrolytes (< 1 mole% solute), conventional thermodynamic models such as Mott-Schottky and Gouy-Chapman describe experimentally observed distributions of electrochemical potential and point defects near GBs[3,107].

However, for concentrated solid solutions (> 1 mole% solute), experimental observations consistently fail to reflect the thermodynamically expected defect profiles derived from these theories, likely due to their omission of significant defect interactions involving acceptor solutes, reduced cations (e.g., Ce^{3+}), and $V_O^{\bullet\bullet}$ [95,108–110]. This is a major drawback as concentrated solid solutions comprise most of the technologically important ceramics[103]. More accurate computational models based on density functional theory (DFT) are limited in simulation cell size and are non-trivial for ascertaining point defect distributions near GBs in concentrated solid solutions[111]. Inhomogeneous thermodynamic approaches, i.e., phase-field models, are able to replicate experimentally measured volume-averaged ionic conductivity of ceramics,[112–116] or microscopically observed point defect compositions[115] *independently*, but a single model has not been successful at reproducing *both* conductivity and defect concentration profiles.

Here, we present an experimental-computational framework that predicts which GBs in a polycrystalline electrolyte likely facilitate ionic conductivity. We developed a thermodynamic phase-field modelling framework and applied it to a model concentrated solid solution oxygen electrolyte $Gd_{0.25}Ce_{0.75}O_{2-\delta}$, wherein the GB-to-GB variability in defect concentrations (Gd^{3+} solutes, electrons localized at Ce^{3+}, and $V_O^{\bullet\bullet}$) was measured microscopically using STEM electron energy-loss spectroscopy (EELS) and energy-loss near-edge structure (ELNES). These data were used to predict the GB-to-GB variability in cross-GB ionic conduction using a unique model, which prioritizes reproducing microscopically observed GB defect concentrations and considers defect-defect interactions in highly concentrated solid solutions, making the framework applicable to other technologically relevant solid electrolytes. Across the GBs studied, we revealed a non-monotonic relationship between $V_O^{\bullet\bullet}$ depletion and GB conductivity, with the highest conductivity predicted for intermediate $V_O^{\bullet\bullet}$ depletion amount. This work lays the foundation for future experimental-computational research and advanced data-driven design of solid electrolytes needed for functional and energy storage/conversion devices.

3.4 Materials and Methods

3.4.1. Fabrication and physical characterization

$Gd_xCe_{1-x}O_{2-\delta}$ nanoparticles (x = 0.001, 0.01, 0.05, 0.1, 0.2, 0.25) were synthesized using a coprecipitation method.[117] Prepared compositions are named "GxCO", with x being the mole % of Gd, e.g., G25CO is the aforementioned x = 0.25 sample. Gadolinium nitrate hexahydrate and cerium nitrate hexahydrate (99.9% purity, Alfa Aesar, Ward Hill, MA) were dissolved in deionized water and mixed. Addition of ammonium carbonate to the solutions resulted in precipitation of Ce and Gd mixed carbonates. To evaporate all organics, solutions were stirred at 80 °C for 1h then dried overnight at 100 °C. Products were calcined at 700 °C for 2 h, then deagglomerated using mortar and pestle.

The powder was pressed into pellets using a 13 mm cylindrical stainless-steel die with a pressure of 186 MPa for 2 min. Stearic acid was used as a lubricant inside the die. Pellets were covered by powder beds in an alumina crucible and sintered at 1550 °C for 5 h (5 °C/min heating/cooling rates) in an NBD-M 1700 muffle furnace (NBD LAB, Kibbutz Zikim, Israel). Sintered pellets were polished using 6.5- 63 μm SiC grids.

X-ray diffraction (Rigaku SmartLab, Wilmington, MA) confirmed the expected fluorite crystal structure, and the relationship between lattice parameter and Gd dopant concentration, which indicated successful formation of single-phase solid solutions (Fig 3.1. in results and discussion). Theoretical density was calculated using lattice parameters from XRD data and the real density was measured using the Archimedes method. Pellets were prepared for SEM by polishing to 1-micron finish using diamond suspensions, then thermally etched for 30 min at 1440 °C (10 °C/min rate). After etching, the samples were sonicated in ethanol and acetone for 5 min, dried and the microstructures of the pellets were observed in a field-emission scanning electron microscope (Magellan XHR 400L FE-SEM, Thermo Fisher Scientific, Waltham, MA) with an electron beam accelerating voltage of 10 kV and 10 pA, respectively. To avoid charging effects in the SEM, pellets were coated with 3 nm of iridium. The average grain sizes were estimated over a total of 300 random grain measurements via ImageJ (open source). Physical properties of the bulk specimen are provided in Table 3.1 in results and discussion.

The G25CO pellet was used for experimental measurement of defect profiles across the GBs using STEM EELS. Energy-dispersive X-ray spectroscopy (EDS) in SEM was used to measure the composition of G25CO at 5 random locations on sample surface (2500 μm^2 each). By comparing the averaged EDS spectrum to a series of simulated EDS spectra calculated using NIST DTSA-II X-ray processing software,[118] the stoichiometry of G25CO was confirmed to be $Gd_{0.245}Ce_{0.755}O_{2-\delta}$ (Fig. 3.2 in results and discussion) (0.245 rounded up to 25).

3.4.2. TEM specimen preparation by focused ion beam (FIB)

A thin foil STEM specimen was prepared using the focused ion beam (FIB) lift-out technique in a dual-beam SEM/FIB (TESCAN GAIA3, Brno-Kohoutovice, Czech Republic) equipped with Ga^+ focused beam. To minimize contamination prior to STEM characterization, the specimen was plasma cleaned in O_2/Ar for 10 min before insertion into the TEM column.

3.4.3. Defect chemistry measurements by electron energy loss spectroscopy (EELS)

Point defect concentration profiles across 5 random GBs were measured using aberration-corrected STEM coupled with EELS (JEM-ARM300F, JEOL Ltd, Japan). A convergence semi-angle of 28 mrad, collection semi-angle of 100 mrad, exposure time of 0.02 S/pixel, and 0.05 eV/pixel dispersion were used to collect the EEL spectrums across the GBs. Several 1D profiles in each EEL spectrum are averaged to calculate the overall defect profile across each GB as well as the uncertainty values. Microscope data were processed using Gatan Microscopy Suite, (Gatan, Pleasanton, CA). EELS background was subtracted using the inverse-power law fits (Table 3.1)

Table 3.1. EELS background and signal windows used in analysis.

Core loss Edge	Background window (eV)	Signal Window (eV)
Ce M	650 - 868	869 - 1000
Gd M	1022 - 1168	1169 - 1289
O K	415 - 524	525 - 594
Ce M_5	650 - 868	879.5 - 882
Ce M_4	650 - 868	897.5 - 900

The quantification of point defects across the GBs were performed using the Cliff-Lorimer method.[119,120] K factors (microscope detection sensitivity factors) were measured using the grain EEL spectra (~ 6 nm away from GB cores) and were used to convert background-subtracted signal intensities to mole fractions using the Cliff-Lorimer equation (Eq. 3.1):

$$\frac{C_{Ce}}{C_{Gd}} = K_{Ce-Gd} \cdot \frac{I_{Ce}}{I_{Gd}} \qquad \text{Eq. 3.1}$$

where C and I are concentration and signal intensity, respectively. Averaged K factors (sensitivity factors) were $K_{Ce\text{-}Gd}$=1.87 and $K_{Ce\text{-}O}$ = 3.93 assuming the grain composition (at least 6 nm away from each GB) is equal the measured ($Gd_{0.245}Ce_{0.755}O_{2-\delta}$) stoichiometry. O K, Ce M_{45} and Gd M_{45} EELS ionization edges were used to measure defect concentrations (Fig. 3.3 in results and discussion), and Ce M_{45} ELNES (Ce M_4-to-M_5 peak ratio) were used to quantify the reduction of Ce^{4+} to Ce^{3+} near the GB. Lower Ce M_4-to-M_5 peak ratio values are correlated to the reduction of Ce^{4+} to Ce^{3+}, due to the addition of one valence electron to 4F orbital.[121] The Ce M_{45} ELNES in grain and at the GB core were used to calculate the highest and lowest Ce M_4-to-M_5 peak ratios (taken as the points of minimum (A) and maximum (B) amounts of relative $Ce^{4+} \rightarrow Ce^{3+}$ reduction for each case- Fig 3.1.).

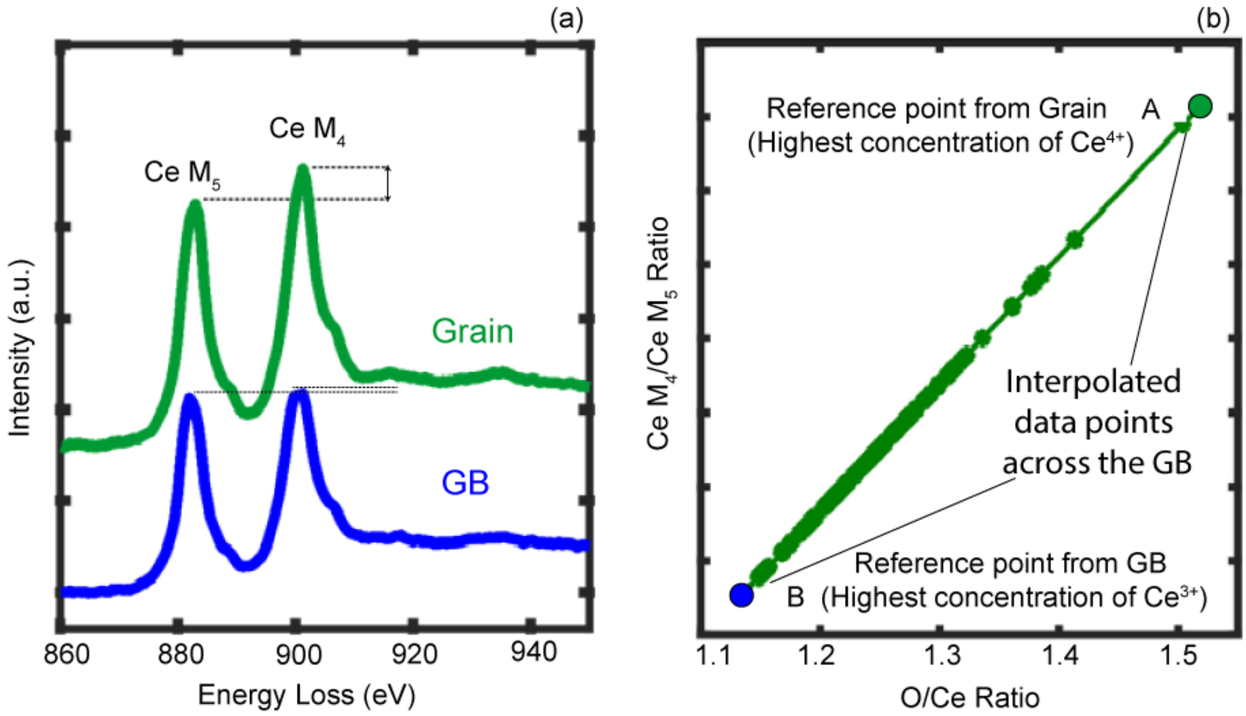

Fig. 3.1. (a) ELNES of Ce M_{45} for grain and GB. (b) The linear relationship between Ce M_4/M_5 ratio and oxygen/cerium ratio for oxidation state quantification.

Linear interpolations between the highest and lowest Ce M_4-to-M_5 peak ratio values (points A and B) were used to calculate the molar fractions of Ce^{3+} and Ce^{4+}. Due to the bombardment of specimen surface with Ga^{+} during preparation, partial reduction of Ce^{4+} to Ce^{3+} was observed in the grain. Subsequently, the Ce^{3+} concentration profile was scaled to zero in the grains to account for the assumption that all Ce in the center of the grains is fully oxidized (Ce^{4+}). We assumed too that the concentration of $V_O^{\bullet\bullet}$ in the grains was equal to 0.5 × (Gd^{3+}+ Ce^{3+}). We made no assumption about the Gd or $V_O^{\bullet\bullet}$ concentrations at/near the GBs.

3.4.4. Ionic transport measurement by electrochemical impedance spectroscopy (EIS)

Grain, specific GB, and total O^{2-} conductivity, as well as the associated conductivity activation energies were measured from 207 °C to 521 °C in air (~ 50 °C increments with 2 h hold at each temperature) using EIS. Measurements were performed from 0.1 Hz to 1 MHz with 50 mV applied potential using a commercial electrochemical measurement station (Plug & Probe, Huber Scientific, Vienna) connected to a potentiostat (Interface 1010e, Gamry Instruments, Warminster, PA). Pellets were heated using a tube furnace (Carbolite Gero 1600, UK). Porous silver paste (Fuel Cell Materials, Columbus, OH) was applied on the polished surfaces of all pellets and annealed at 800 °C for 1 h.[122]

EIS data were interpreted by fitting to equivalent circuit models containing a single resistor in series with 2 subcircuits each comprising a resistor in parallel with a constant phase element (Q). A CPE is a non-ideal capacitor which has an uneven distribution of charge alongside the capacitor. Constant phase element has an impedance (Z) given by Eq. 3.2. below:

$$Z_Q = [(j\omega)^{\alpha} Y]^{-1} \qquad \text{Eq. 3.2}$$

where ω is radial frequency, Y and α are constants, with α ranging between 0 - 1 and Y experimentally found to be close to unity.[123] Each RQ pair in the model (corresponding to an arc in the Nyquist plot) represents an electrochemically distinct phase component. Components can either correspond to electrochemical responses of the grain, GB, or electrode. The R-2RQ circuit model was used in our analysis which corresponds to system offset resistance (R_0), grain (R_1Q) and GBs (R_2Q). Eq. 3.3. was used to calculate the total conductivity:

$$\sigma_t = \frac{L}{RA} \qquad \text{Eq. 3.3}$$

where L and A are specimen thickness and cross-section area, respectively. R is the resistance (i.e., the diameter of the grain arc in the calculation of grain conductivity, or the sum of the diameters of the grain and GB arcs in the calculation of total conductivity). For GB conductivity, Eq. 3.4. was used[124]:

$$\sigma_{GB} = \frac{\tau_{GB}}{\tau_g} \cdot \sigma_t \qquad \text{Eq. 3.4}$$

where τ, is the time constant which is equal the product of resistance and capacitance values for each arc (determined from data fitting). Eq. 3.5. is the Arrhenius expression used to calculate the conductivity activation energy, E_a of grain and GB:

$$\sigma = \frac{\sigma_0}{T} exp(\frac{-E_a}{k\,T}) \qquad \text{Eq. 3.5}$$

where T is temperature in Kelvin, σ_0 is a pre-exponential constant, and k is Boltzmann's constant. Eq. 3.6. was used for simplified porosity correction (ionic conduction is limited to the solid portion of the ceramic) to calculate the accurate grain and total conductivity[125,126]:

$$\sigma = \frac{1}{\rho D_f} \qquad \text{Eq. 3.6}$$

D_f ($D_{fraction}$) represents relative theoretical density, and ρ is resistivity. Without this porosity correction (taking volume fraction of pores into consideration), the material's actual conductivity is underestimated.

3.4.5. Modeling defect chemistry and ionic conductivity

The Poisson-Cahn model[22] equipped with BSS-ANOVA Gaussian process (GP) stochastic functions[127] was applied to the experimental results to estimate free energy functions for each GB. To accomplish this, first BSS-ANOVA GPs, δ (Eq. 3.7) were applied to the experimental defect profiles directly, using a modified version of the MATLAB-based FoKL-GP[128] sampling routine:

$$\delta = \sum_i \beta_i \varphi_i \quad \text{Eq. 3.7}$$

where β_i are the estimated basis coefficients and φ_i are the known basis functions. The MATLAB-based sampling routine requires a set of user inputs to build a single-output BSS-ANOVA emulator model automatically. The user input parameters include shape (a) and scale (b) parameters of the inverse gamma (IG) distribution for the observation error variance (σ) of the data. Additionally, τ_a and τ_b are parameters of the IG distribution for the τ^2 parameter (variance of the basis coefficients). The selected number of draws or specimens is also required. BSS-ANOVA functions are represented by an expansion over a known set of spectral and deterministic basis functions (φ_i) which are expressed using cubic splines. The model-building routine decomposes the desired function into main effects, two-way interactions, and so on through an expansion over the basic functions. It incrementally adds higher order basis terms to better model the experimental data profiles.

Although adding more terms can, in principle, achieve a better coverage of the data variability, too many terms can make the model unnecessarily complex, and a balance is therefore struck using the Bayesian Information Criterion (BIC), which penalizes models that have more expansion terms. Due to the inherent noise in the experimental data, the fitted emulator defect profiles require additional filtering to remove physically inconsistent data (such as negative concentrations) and enforce reasonable boundary conditions on the system, such as electroneutrality in the grain. When readily differentiable, stochastic representation of the defect profiles has been achieved, the next step is to use the continuous BSS-ANOVA functions for the defects to numerically solve Poisson's equation (Eq. 3.8 and 3.9) for the electrostatic potential (ϕ).

$$\nabla^2\phi = -\frac{F}{\varepsilon_r\varepsilon_0}\rho \qquad \text{Eq. 3.8}$$

where ρ corresponds to the charge density:

$$\rho = 2n_v v - n_y y - n_q q \qquad \text{Eq. 3.9}$$

The filtered emulator functions for the dopant (y), electrons (q) and $\mathrm{V_O^{\bullet\bullet}}$ (v) defect site fraction profiles are then accessible to solve the Poisson-Cahn formulation for inhomogeneous systems. This allows the emulator routine to be reused in modeling the free energy of the system (F) and build an empirical function (Eq. 3.10) for the interaction energies of the defects (η) and their corresponding gradient energy coefficient (c_v and c_y):

$$F = \eta(y, v, q) + \frac{c_v}{2}\left|\frac{dv}{dx}\right|^2 + \frac{c_y}{2}\left|\frac{dy}{dx}\right|^2 + \sum_i z_i F n_i \chi_i \phi + W(y, v, q) \qquad \text{Eq. 3.10}$$

where W (Eq. 3.11) is the configurational entropy and η (Eq. 3.12) the excess free energy contribution from the defect interaction energies that is modelled using the BSS-ANOVA decomposition (Eq. 3.13):

$$W(y, v, q) = \sum_i RT[\chi_i \, ln \, \chi_i + (1 - \chi_i) \, ln(1 - \chi_i)] \qquad \text{Eq. 3.11}$$

$$\eta(y, v, q) = \sum_i \beta_i \varphi(y, v, q) \qquad \text{Eq. 3.12}$$

$$\eta(y,v,q) = \beta_1\varphi_1(v) + \beta_2\varphi_1(y) + \beta_3\varphi_1(q) + \beta_4(v)\,\varphi_1(y) + \beta_5\varphi_1(v)\varphi_1(q) + \beta_6\varphi_1(y)\varphi_1(q) \qquad \text{Eq. 3.13}$$

Taking a variational derivative of the free energy (F) with respect to each defect (Eq. 3.14) gives the electrochemical potential of the defect (μ_i) in the system (Eq. 3.15):

$$\frac{\delta F}{\delta x_i} = \mu_i \qquad \text{Eq. 3.14}$$

$$\mu_i = \frac{\delta \eta}{\delta \chi_i} - c_i \frac{d^2 \chi_i}{dx^2} + z_i F \phi + RT \, ln \frac{\chi_i}{1 - \chi_i} \qquad \text{Eq. 3.15}$$

where z_i represents the defect-specific charge, ϕ the electrostatic potential, F the energy constant, R the universal gas constant, T the temperature, and χ_i the defect-specific site fraction.

Balancing this result with the grain value, $\tilde{\mu}_i$ (Eq. 3.16) leads to a set of differential equations (Poisson-Cahn formalism). These equations can be used to transform the microscope data in the emulator into a linear statistical model for the coefficients in the

BSS-ANOVA expression excess free energy, η, and the gradient energy coefficients, c_i using Eq. 3.17:

$$\mu_i - \tilde{\mu} = 0 \qquad \text{Eq. 3.16}$$

$$\frac{\partial \eta(\chi_i - \tilde{\chi}_i)}{\partial \chi_i} - \frac{c_i}{n_i}\frac{d^2\chi_i}{dx^2} = -z_i F \phi - RT\, ln\left(\frac{\chi_i}{1-\chi_i} \cdot \frac{1-\tilde{\chi}_i}{\tilde{\chi}_i}\right) \qquad \text{Eq. 3.17}$$

The outcome from the data-driven model-building routine using this approach provides a concentration-dependent function for the interaction energies of the defects (self-interaction and two-way interactions). Because of the high observation error (noise) in the experimental measurements, a direct sub-model for electrons was ignored and terms were estimated only for $V_O^{\bullet\bullet}$ and the dopant defect concentrations. (Data for electrons was utilized in the solution of Poisson's equation and in the estimation of interaction terms with vacancies and the dopant.) Ultimately this yields a two-dimensional surface for the interaction free energy, in terms of the concentration of the defects.

The rare-earth solute and oxygen vacancy (RE-V) interaction energy for a Gd-doped system is used to determine the ionic conductivity for a given specimen's data by applying the Nakayama-Martin model[55] (Eq. 3.18) to discretize the one-dimensional domain into smaller elements and sum the individual resistivities (Ω_i) in series:

$$\Omega_i = \frac{\Delta x_i}{\zeta(4F^2/RT)\nu\lambda^2 n_v v_i e^{\left(-FE_{a_i}/RT\right)}} \qquad \text{Eq. 3.18}$$

where Δx denotes the 1D element length (m), ζ the unitless jump frequency, ν the vibrational frequency (s^{-1}), λ the lattice parameter (m), FE_{a_i} the Faraday constant ($C.mol^{-1}$) and

E_{a_i} is the activation energy for discretized element i. Knowing the averaged grain size measurement, the total conductivity, σ_T, (Eq. 3.19) for each grain is estimated and identifying the last discretized element in the series resistance, the grain/bulk conductivity (σ_b) is also determined. With the total and grain conductivities estimated, the GB conductivity (σ_{GB}) is approximated by using a cut-off of the initial element resistivities where the interaction energy profile has the most significant variation with respect to the grain/bulk.

$$\sigma_{Total} = \frac{l}{\sum_{i=1}^{L} \Omega_i} \qquad \text{Eq. 3.19}$$

Given the intrinsically heterogeneous fluctuations from the microscopic data for any experimentally obtained compositional line-scan for a unique GB, and the favored generalization from comprehensive datasets, it becomes apparent that coupling multiple datasets to generate a global description of the excess free energy, and thus a more unified defect-defect interaction energy, gives a more realistic idea of the behavior for the GB ionic conductivity in each individual GB.

Expanding on this notion and following the approach from Scott *et al.*[129], a consolidated model ($\hat{\beta}$) obtained using a weighted average method (Eq. 3.20) for combining the separate basis coefficients from each individual BSS-ANOVA GB model (β_s) is imposed and used to produce grain, total, and GB conductivities for the 5 experimental datasets.

$$\hat{\beta} = \left(\textstyle\sum_s W_s\right)^{-1} \textstyle\sum_s W_s \beta_s \qquad \text{Eq. 3.20}$$

where W_s are the model precision matrices, computed as the inverse of the covariance matrices for the basis coefficients, and β_s the mean for the basis coefficients.

3.5 *Results and Discussion*

3.5.1. Physical properties of GCO samples

X-ray diffraction confirmed the expected fluorite crystal structure, and the successful Gd doped single-phase solid solutions, which indicated an expansion in lattice parameter as dopant concentration increases (Fig. 3.2).

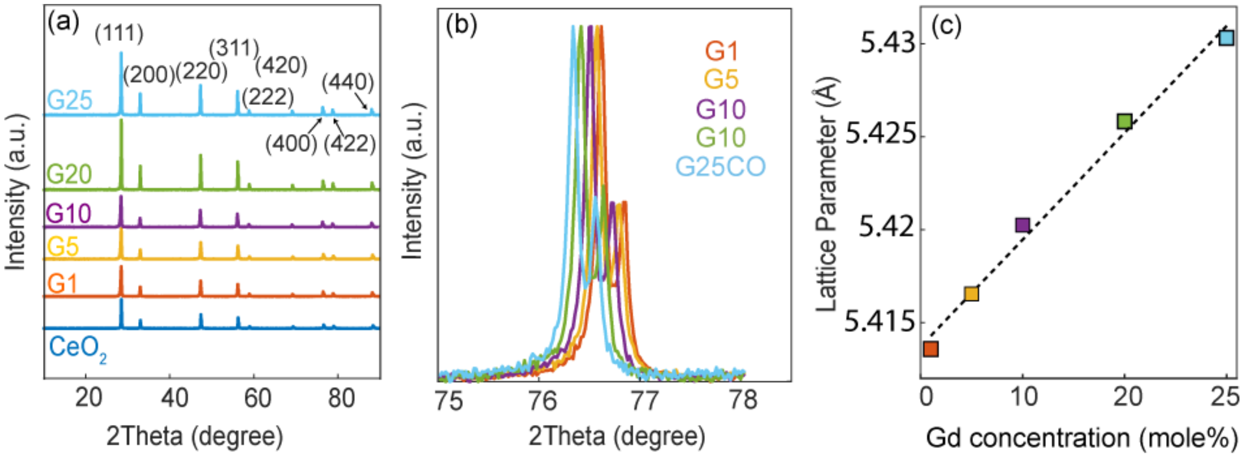

Fig. 3.2. (a) X-ray diffraction patterns of $Gd_xCe_{1-x}O_{2-\delta}$ (GCO) pellets with 1-25 mole % Gd and pure ceria (from Advantage Materials Research, Southlake, TX). (b) As the Gd content increases, XRD peaks shift to lower diffraction angles. (c) Change in lattice parameter indicates lattice expansion and successful solid solution preparation.

Density of pellets measured using Archimedes method, lattice parameter measured in XRD, and average grain size measured by SEM are reported in Table 3.2.

Table. 3.2. Physical properties of G_XCO (X = 0.1, 1, 2, 5, 10, 20, and 25 moles % Gd) sintered pellets. G25CO is the pellet used for STEM EELS defect chemistry concentration measurements and contains ~ 24.5 mole % Gd per SEM EDS analysis (Fig. S3).

Gd content-x $Gd_xCe_{1-x}O_{2-\delta}$	**Lattice Parameter (Å)**	**Theoretical Density (g cm^{-3})**	**Real Density (g cm^{-3})**	**Relative Density (%)**	**Average Grain Size (µm)**
0.001	5.410	7.18	6.26	89.32	2.06 ± 0.72
0.01	5.413	7.21	6.39	88.57	2.67 ± 1.8

0.05	5.416	7.23	6.61	91.44	1.26 ± 0.9
0.01	5.420	7.25	6.49	89.61	4.65 ± 2.04
0.02	5.425	7.30	6.59	90.25	2.12 ± 0.65
~ 0.25 (0.245)	5.430	7.35	6.76	92.04	2.05 ± 0.71

SEM-EDS was used to measure the composition of synthesized powder. To confirm the measured composition, EDS spectrum was simulated for each composition and experimental EDS spectrum was compared with the simulation results as shown in Fig. 3.3.

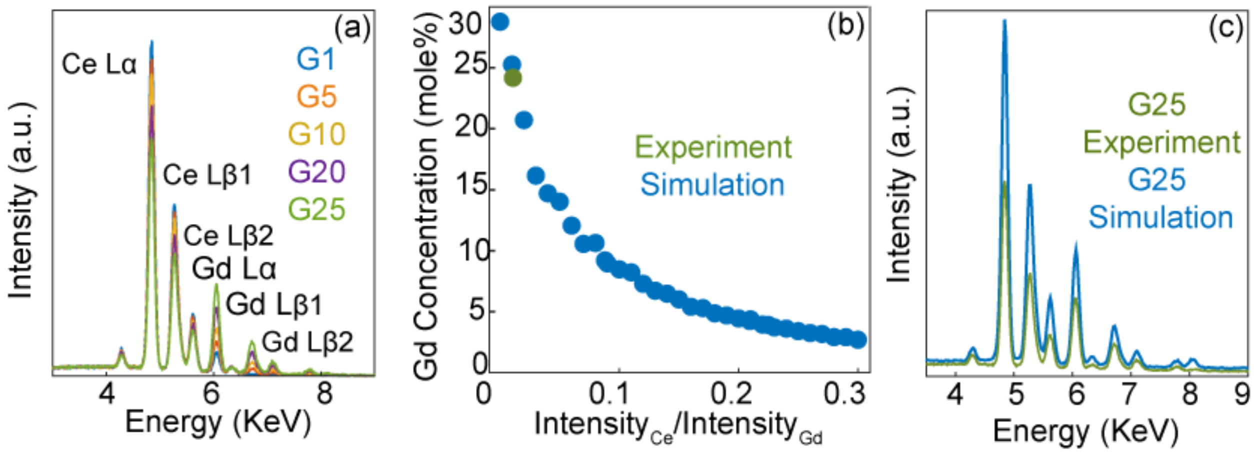

Fig. 4.3. SEM EDS data were simulated for G_XCO as a function of Gd content (a). The simulated EDS spectra of 1-25 mol% GCO, (b) Simulated Ce-to-Gd intensity ratio SEM-EDS signal intensity ratios as a function of Gd dopant in blue with the experimentally measured Ce-to-Gd intensity ratio for G25CO in green. (c) Comparison of experimentally measured EDS with the simulation results to estimate the true Gd concentration of 24.57 ± 1 mol% (labeled as G25CO).

3.5.2. Quantitative chemical analysis of GBs

To elucidate the impact of GB-to-GB local defect chemistry distributions on GB and total electrical conductivity, local concentrations of Gd^{3+}, $Ce^{3+/4+}$ and $V_O^{\bullet\bullet}$ were measured across 5 randomly selected GBs in G25CO using STEM EELS. Fig. 3.4 shows an EELS spectrum containing the core-loss edges used for defect measurements.

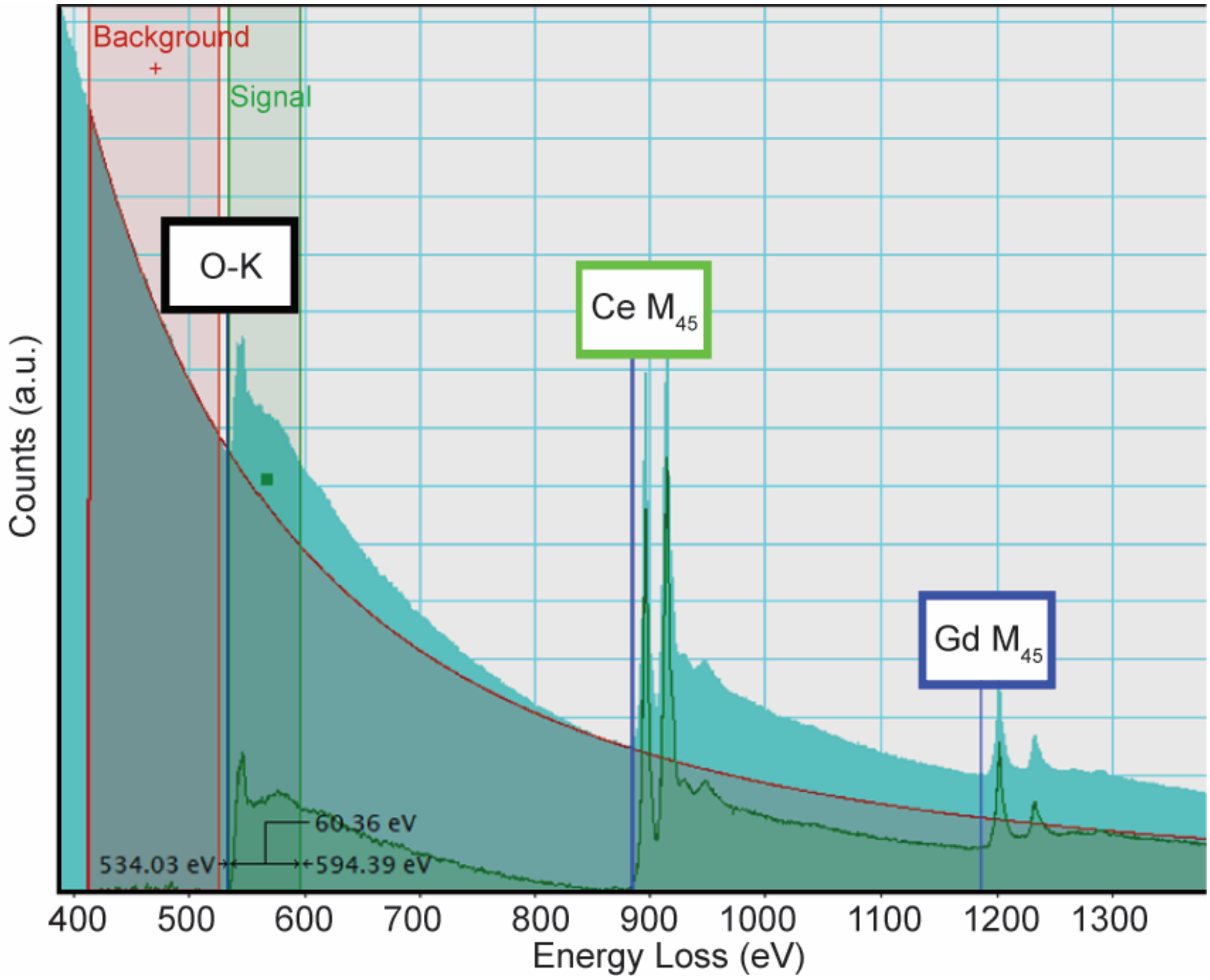

Fig. 3.4. Full EEL spectrum of grain in G25CO showing the O K-edge, Ce and Gd M_{45} edges used for composition quantification. The displayed background fitting window for O K-edge ('background') shows how the background was fit and subtracted from the oxygen signal ('signal').

Fig. 3.5 a shows an SEM image of grains in G25CO polycrystal. A HAADF STEM image of one the selected GBs that was atomically abrupt and free of intergranular phases is shown in Fig. 3.5 b O K, Ce M_{45} and Gd M_{45} EELS edges were used to quantify the local GB point defect concentrations (Fig. 3.5 c-e).

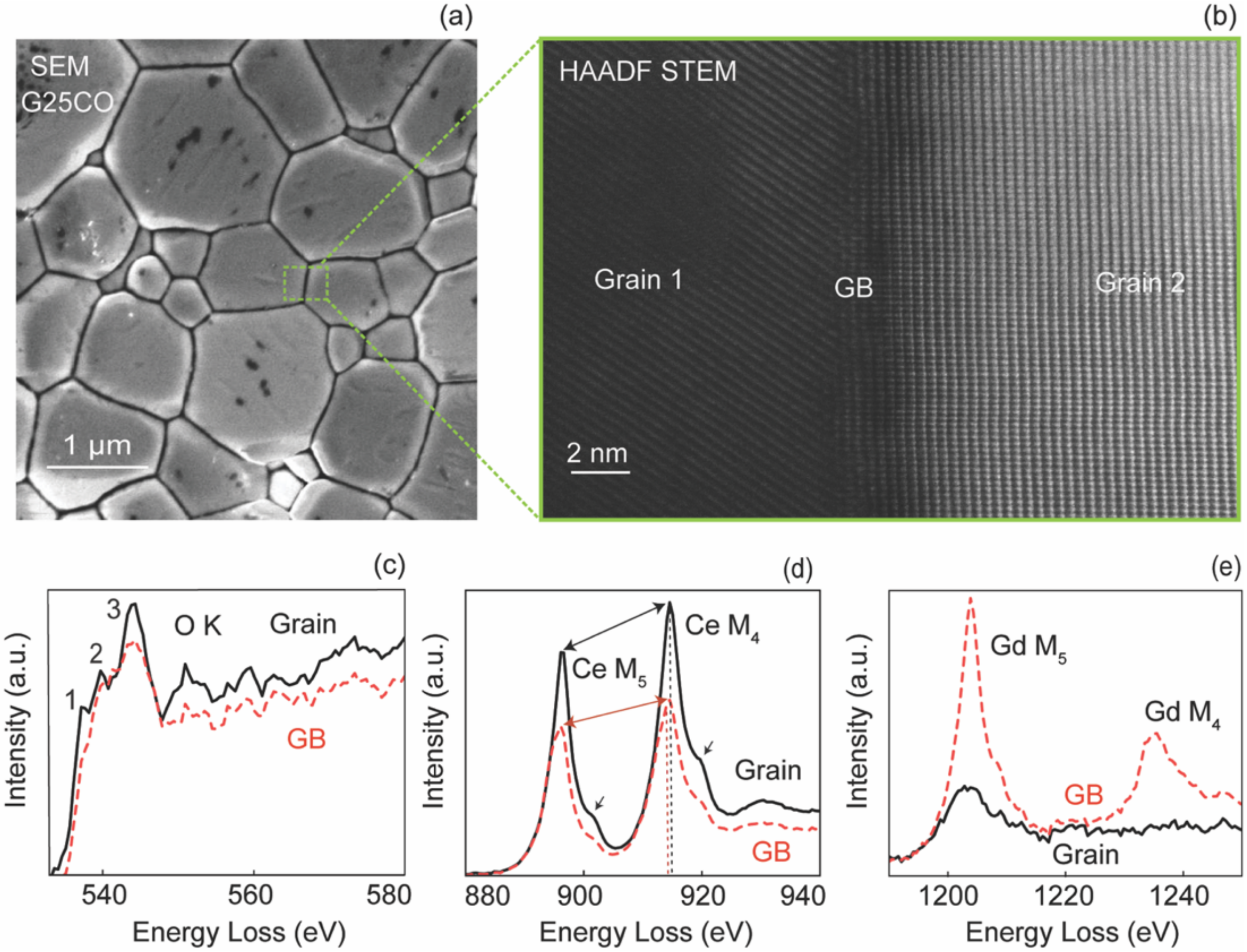

Fig. 3.5 (a) SEM image reveals grains and GBs within the microstructure of G25CO. (b) STEM HAADF image showing the expanded view of a GB plane in this sample. ELNES of (c) O-K (1-3 peaks), (d) Ce M_{45}, and (e) Gd M_{45} collected at the grain and GB, respectively.

The concertation profiles of $V_O^{\bullet\bullet}$, $Ce^{3+/4+}$ and Gd^{3+} across this GB measured are presented in Fig. 3.6 a-d. It was observed that all GBs exhibited decreased local $V_O^{\bullet\bullet}$ concentration (increased oxygen concentration), depletion of Ce^{4+}, and accumulation of Gd^{3+} at/near the GB plane. The GB segregation/depletion chemical widths were ~3 nm at full-width half maximum, as typically observed[130]. We attribute the differences in STEM HAADF and EELS intensity across GBs to electron channeling effects due to the different crystal orientations in neighboring grains[131]. Quantification of defect concentration was done by mirroring the EELS concentration profiles across the GB and calculating the average concentrations.

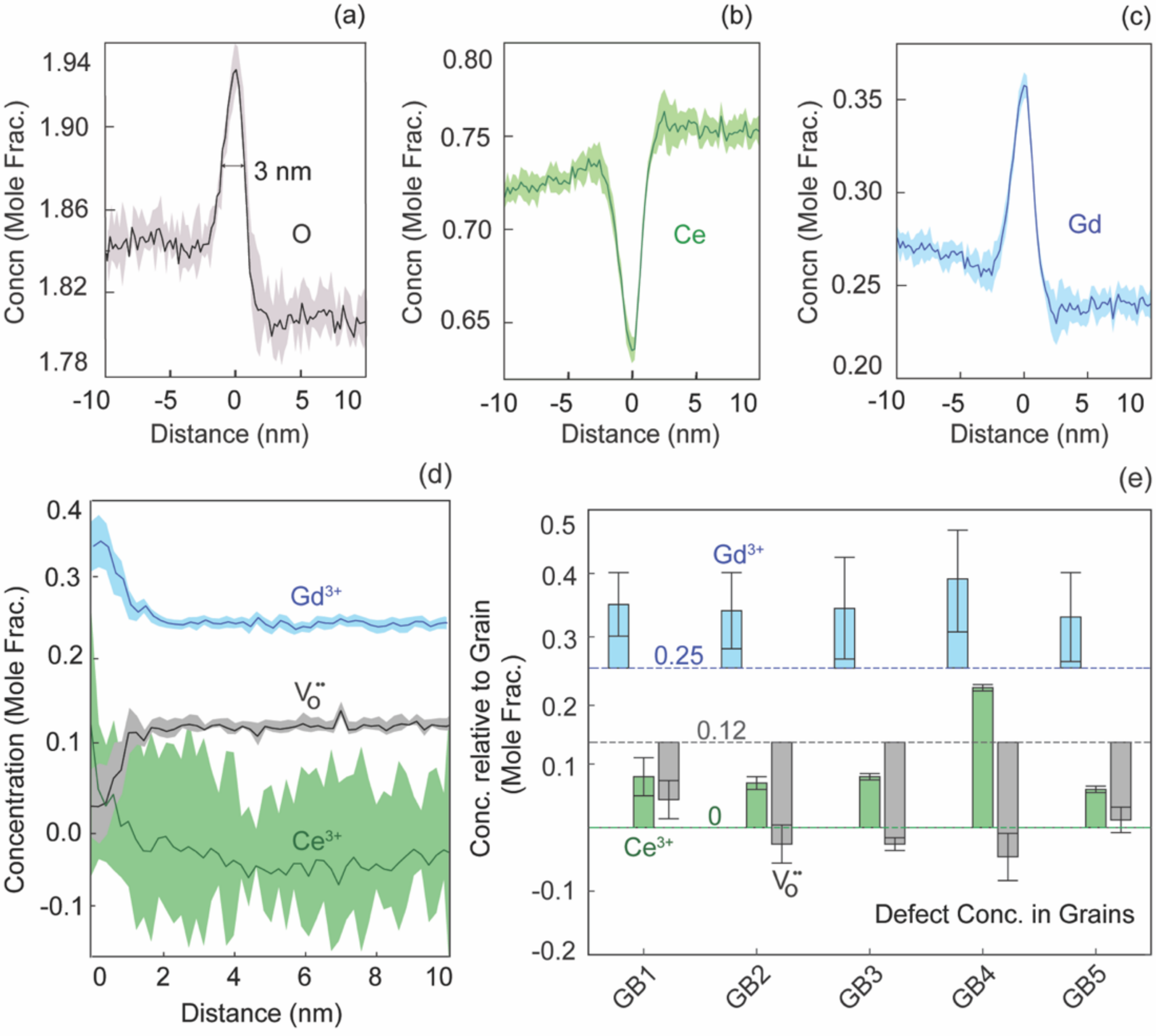

Fig. 3.6. Measured concentration profiles of (a) O, (b) Ce and (c) Gd for the GB in Fig. 1. (d) Measured concentration profile of $V_O^{\bullet\bullet}$, Ce^{3+} and Gd^{3+} for the GB in Fig. 3.4. The standard deviations associated with measuring 5 rows of pixels within the area maps is shown as the

measurement uncertainty in concentrations. (e). Quantified segregation and depletion of Ce^{3+}, Gd^{3+} and $V_O^{\bullet\bullet}$ relative to the grains for GB1-GB5.

The reduction of Ce^{4+} to Ce^{3+} at/near GBs which was observed before,[132,133] can introduce local electrons to the GB, influence local charge compensation and affect GB and total conductivity values by influencing negative charge compensation near positively charge GB cores and complicating defect-defect interactions in the SCL. Therefore, ELNES was used to quantify the Ce^{3+} concentration near the GBs.

The reduction of Ce^{4+} to Ce^{3+} shows up as an decrease in the Ce M_4-to-M_5 peak intensity ratio, the disappearance of high-energy-loss M_5 and M_4 satellite peaks, and a slight shift of Ce M_{45} edges to lower energy-loss values[132,134,135]. Defect concentration profiles of $V_O^{\bullet\bullet}$, Gd^{3+}, and Ce^{3+} measured across the GBs showed that Gd^{3+} and Ce^{3+} concentrations increased at all GBs, whereas $V_O^{\bullet\bullet}$ are depleted (Fig. 3.6 e and Table 3.3). We found depletion of $V_O^{\bullet\bullet}$ by as much as 0.08-0.17 mole fraction, enrichment of Gd^{3+} by 0.09-0.12 mole fraction, and enrichment of Ce^{3+} by 0.01-0.23 mole fraction, qualitatively in line with prior experimental and conventional modelling results describing GB defect chemistry in dilute $Gd_xCe_{1-x}O_{2-\delta}$[136–138].

Table 3.3. Defect concentrations measured at each GB using STEM EELS. Concentration values in this table are absolute values and not relative to the defect concentration at the grain interior.

Concentration (Mole Frac.)	**Gd^{3+}**	**Ce^{3+}**	**$V_O^{\bullet\bullet}$**
GB1	0.35	0.08	0.03
GB2	0.34	0.07	-0.04
GB3	0.34	0.08	-0.04
GB4	0.39	0.22	-0.06

GB5	0.33	0.06	-0.002

Given this significant difference in GB-to-GB local defect chemistry, we set about answering the key question: How does local compositional variability between GBs manifest and influence the overall ionic conductivity through the polycrystalline electrolyte? For instance, one might expect GB1 (Fig. 3.5 e)—with the least-significant $V_O^{\bullet\bullet}$ depletion—to have the highest ionic conductivity, recalling that lower $V_O^{\bullet\bullet}$ depletion is indicative of smaller space charge potential and thus faster O^{2-} hopping across the GB1 [107,114,139]. In contrast, GB4—with the most-significant $V_O^{\bullet\bullet}$ depletion—should then be expected to have the lowest ionic conductivity. The remainder of this work attempts to clarify this by first measuring the grain, GB, and total ionic conductivities of G25CO, and then developing a thermodynamic model capable of predicting ionic conductivity based on our experimental microscopic STEM EELS defect chemistry analysis. By comparing experimental AC electrochemical impedance spectroscopy (EIS) conductivity measurements with model-predicted conductivity (derived from STEM EELS GB defect concentration profiles), we attempt to determine if the volume-averaged EIS conductivity is most reminiscent of one or more of the GBs investigated microscopically, thus indicating which GBs are more/less consequential to the ceramic electrolyte's overall ionic conductivity.

3.5.3. Oxygen-ion conductivity

To provide experimental data against which our predictive conductivity model could be validated, and to ensure that our materials' properties were consistent with the literature, we determined the volume-averaged grain, specific GB, and total ionic conductivities by measuring the G25CO pellet's impedance, which decreased with increasing temperature as expected due to thermally activated O^{2-} mobility. EIS Nyquist plots were fit to calculate conductivities of G25CO (Fig. 3.7 a-b). From 207 °C to 433 °C, the grain and GB arcs were resolved within our measurement frequency range and successfully fit using a 2RQ model. At 477 °C and 521 °C the grain arc was not resolved, so the GB arc was fit alone using a RQ model. The calculated grain and total conductivities were similar across measured temperatures and ranged from 2.6×10^{-2} S cm^{-1} to 5×10^{-8} S cm^{-1} for G25CO (Fig. 3. 7 c). Comparatively, the specific GB conductivity was significantly lower at all measurement temperatures, ranging from 2×10^{-6} S cm^{-1} to 8×10^{-10} S cm^{-1}. By fitting the conductivity Arrhenius plots, conductivity activation energies for grain, total, and specific GB were calculated to be 1.18 eV, 1.19 eV, and 1.09 eV, respectively (Fig. 3. 7 c).

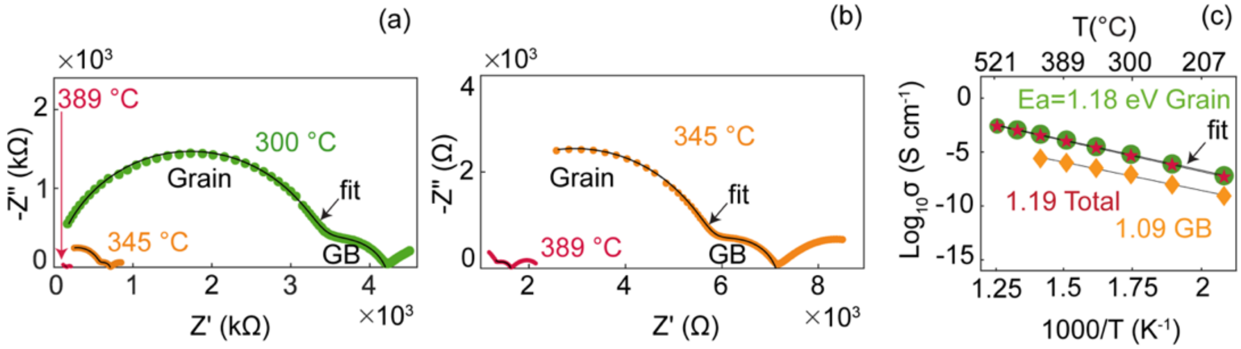

Fig. 2.7. (a) Select EIS data from G25CO measured at 300, 345 and 389 °C. (b) expanded view of EIS data measured at higher temperatures in a. (c) Arrhenius plot showing grain, total and specific GB conductivities along with corresponding conductivity activation energies.

Despite the substantially lower specific GB conductivity, the total conductivity in G25CO was close to the grain conductivity, suggesting the grain size may be large enough to mitigate the negative impact of GBs on the total conductivity though it is unclear why both GB conductivity *and* activation energy are lower than the grain. Because the ionic transport mechanism across GBs with high solute concentration is a topic of current discussion in the literature broadly speaking, to ensure our electrical data align with those already reported, and to potentially shed light on the nanoscale nature of GBs in previous studies, we compared our results with literature[64,95,98,124,140–147]. Our grain, total, and specific GB conductivities closely track the reported values and trends with Gd concentration, confirming that our G25CO sample behaves consistently with materials studied in the field. The grain conductivity activation energy measured here (1.09 eV) is significantly larger than that reported by Zhang *et al,*[146] but is line with an extrapolation of the trend with Gd concentration shown in literature. Importantly, the GB conductivity activation energy is well-aligned with reported data.

3.5.4. Modeling GB defect chemistry to predict ion conductivity

With the goal of identifying which GBs are definitive in overall ionic conductivity, we developed and applied a novel modeling framework which calculates the temperature-dependent conductivity of a hypothetical polycrystalline ceramic solid electrolyte. The model first takes microscopically measured point defect concentration profiles as its primary inputs (e.g., Fig. 3.2 d-e). Thermodynamic quantities governing point defect segregation at GBs are then derived from the data analysis described above. Based on these data and additional grain size measurements (from SEM, e.g., Fig. 3.1 a), a prediction of grain and total conductivity of a hypothetical polycrystalline material is made at varied simulation temperatures using the Martin-Nakayama model[55]. Finally, comparisons between simulated GB conductivities are made to assess which GBs are likely definitive in the overall ionic conductivity.

Experimental data were fit, and subsequently smoothed, using a combination of BSS-ANOVA modeling with physical limitation constraints, and an exponential filtering approach yielding a computational model surrogate for the noisy defect profiles (e.g., Fig. 3.4 a). For each of the 5 GBs, point defect profiles were then used to numerically solve for the electrostatic potential (ϕ) with a finite difference solver and predict the interaction energies (f_{ij}) and gradient energy coefficient (c_i) parameters. To obtain valid electrostatic potential values, the solver required appropriate boundary conditions, which include electroneutrality in the grain/bulk ($\phi_{bulk} = 0$) and a positive interface charge density ($\rho_s > 0$) contribution that is attributed to the existence of charged impurities found at the GB (e.g., Si), such as those reported in other GB electric potential studies found in the literature[84,129,148]. Although the precise concentration of the charged impurities is not explicitly identifiable using this approach, because of the unknown impurity species charge and the combined effect of charged defects, we adjusted the overall surface charge density (SCD) effect for each GB that resulted in optimum convergence for the electrostatic potential solver. The surface charge density (ρ_s) for each GB is tabulated in Table 3.4. and implied from Eq. 3.21.

Table 3.4. Optimized surface charge density values.

GB number	**SCD (ρ_s) [C/m^2]**
GB1	1.0911
GB2	1.8525

GB3	1.0927
GB4	1.6161
GB5	1.9779

$$\rho_s = \frac{F}{\varepsilon_0 \varepsilon_r} z_i n_i [i] \qquad \text{Eq. 3.21}$$

where F is Faraday's constant in C/mol, ε_r the relative permittivity, ε_0 the permittivity of free space, and z_i the charge number, n_i the site density, and $[i]$ the site fraction of defect i, respectively.

Similarly, the model-building routine, using the smoothed defect profile models, was adapted to estimate the dopant-vacancy interaction energy terms and gradient energy coefficients for each GB. Using the configurational entropy and the electrostatic potential energy terms to create a target (Eq. 3.17), the emulator fitted the excess free energy and the gradient energy contributions to the experimental data, as shown in Fig. 3.8 a-c. The parameter values used in running the emulator (Table 3.5) were unchanged for each GB dataset, showing the number of basis function expansion terms (η) that were automatically selected by the routine for the optimum fit for each GB, using forward variable selection. These results were notionally validated by ensuring positive gradient coefficients, whose magnitude resulted in a net secondary order (as opposed to first order main effect) contribution to the overall excess free energy. The resulting gradient energy coefficient averages for each GB dataset are in Table 3.6, with the mean for all 5 GBs.

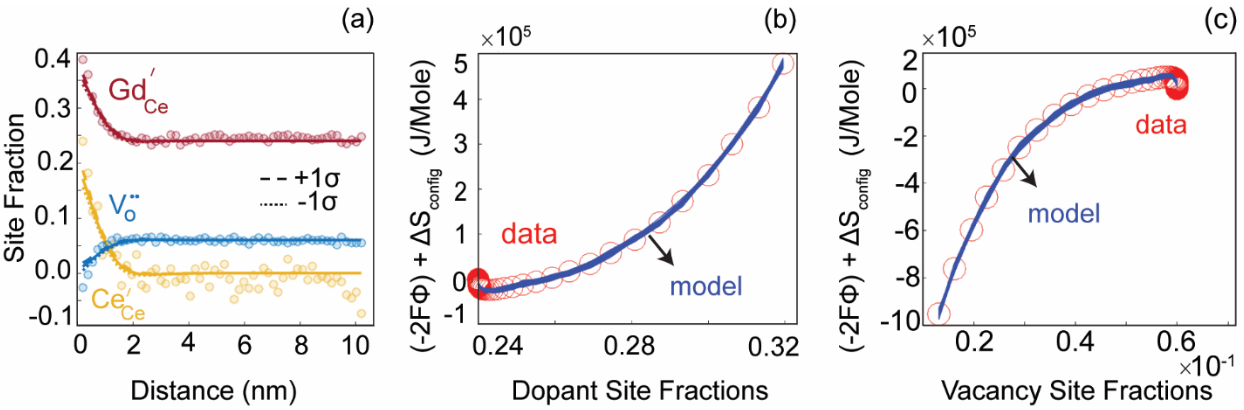

Fig. 3.8. (a) Experimental (circles) and modeled (lines) defect concentration profiles of Ce^{3+}, Gd^{4+} and $V_O^{\bullet\bullet}$ after filtering. Emulator "free energy" data coverage for (b) dopant site fractions and (c) vacancy site fractions in GB5.

Table 3.5. Free energy emulator simulation parameters.

Draws	**a**	**b**	τ_a	τ_b	σ_o^2
50,000	4	0.0024	4	1176	0.0004
	GB1	GB2	GB3	GB4	GB5
# η	26	38	15	13	24

Table 3.6. Modeled dopant and vacancy gradient energy coefficients for each GB dataset.

	c_y **[J/m]**	c_v **[J/m]**
GB1	5.2127×10^{-9}	2.1150×10^{-7}
GB2	3.5221×10^{-7}	1.1803×10^{-6}
GB3	2.0899×10^{-7}	1.4477×10^{-6}

GB4	2.2047×10^{-8}	1.8581×10^{-7}
GB5	1.0074×10^{-6}	5.7945×10^{-6}
Average	3.1917×10^{-7}	1.7640×10^{-6}

The modeled defect interaction energies resulted in contrasting location-dependent profiles for each GB that varied according to the combined concentration of interacting defects found at each location. The defect interaction energy can be plotted as a 2D energy surface with interacting defect concentrations on the axes, showing regions of defect attraction or repulsion (Fig. 3.9). Although the oppositely charged defect interaction energies are mostly negative—implying attraction, there are some unique regions with zero or positive values that suggest areas of repulsion. As a conceptual validation of the modeling framework, we found good evidence to qualitatively support the positive interaction energy values for high concentrations of either defect, which is consistent with previous reports that showed a shift from attractive (negative $\Delta E_{RE\text{-}V}$) to repulsive (positive $\Delta E_{RE\text{-}V}$) defect association energy between the nearest neighbor (1NN) and next-nearest neighbor (2NN). After combining the 5 datasets into a unified weighted average model, the interaction energies were computed from the varying defect concentration profiles (Fig. 3.9 a). The GB interaction energy values for GBs 1 to 5 seem to quantitatively support the results by having similar low values compared to several references that show a range from -0.07 to -0.30 eV for Gd[148,149].

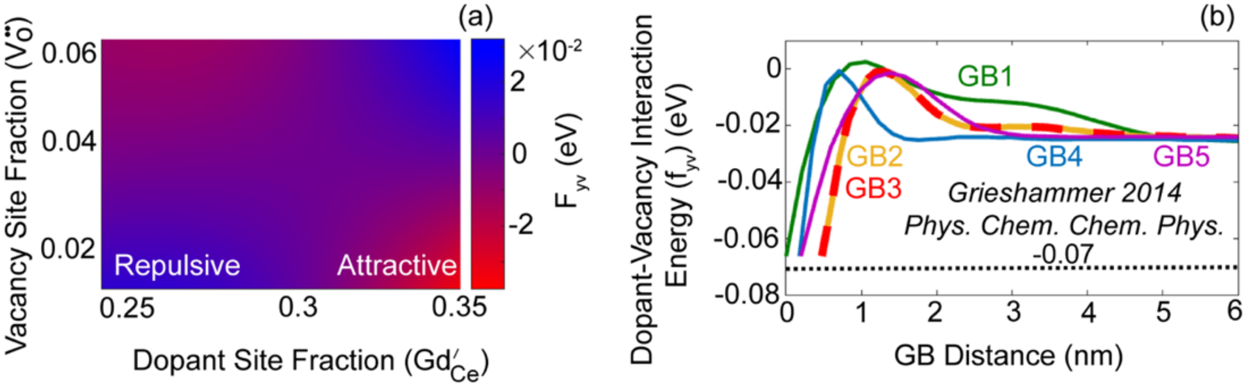

Fig. 3.9. (a) Interaction energy surface for dopant-vacancy defect pair association with varying defect concentrations. (b) Dopant-vacancy defect association energy (f_{yv}) for the 5 measured GBs in addition to a reference.

Given additional information about grain size from SEM imaging, we predicted grain, GB, and total ionic conductivities of hypothetical polycrystalline electrolytes as a function of simulation temperature using the Martin-Nakayama model (Fig. 3.10 a). Each hypothetical electrolyte—containing 1 of the 5 experimentally observed GBs—exhibit varied conductivities and conductivity activation energies that highlight the GBs' relative transport properties, ultimately indicating the GBs' varied contributions to the overall ionic conduction. Significantly, we find strong GB-to-GB variation in both GB conductivity (factor of ~ 3) and GB activation energy (> 0.1 eV), which markedly affects the hypothetical electrolytes' total conductivity and illustrates the importance of understanding GB diversity in solid electrolytes.

Using this framework, we predicted that the hypothetical polycrystalline materials have near-identical grain conductivity and conductivity activation energies, and that the total conductivity is between that of grain and GB, as expected (Fig. 3.10 b). Interestingly, simulated G25CO electrolytes containing "type b" GBs (GB1, GB4 and GB5) have the lowest total and GB conductivity (highest activation energy) of all, whereas simulated electrolytes containing “type b” GBs (GB2 and GB3) exhibit the highest total and GB conductivity (lowest activation energy). This suggests that in the experimental G25CO ceramic fabricated and studied here, type b GBs strongly block the migration of O^{2-} through the polycrystalline electrolyte while type a GBs provide a path of relatively lower resistance. This highlights the power of such predictions, which can identify GBs that are more/less important to the overall ionic conductivity.

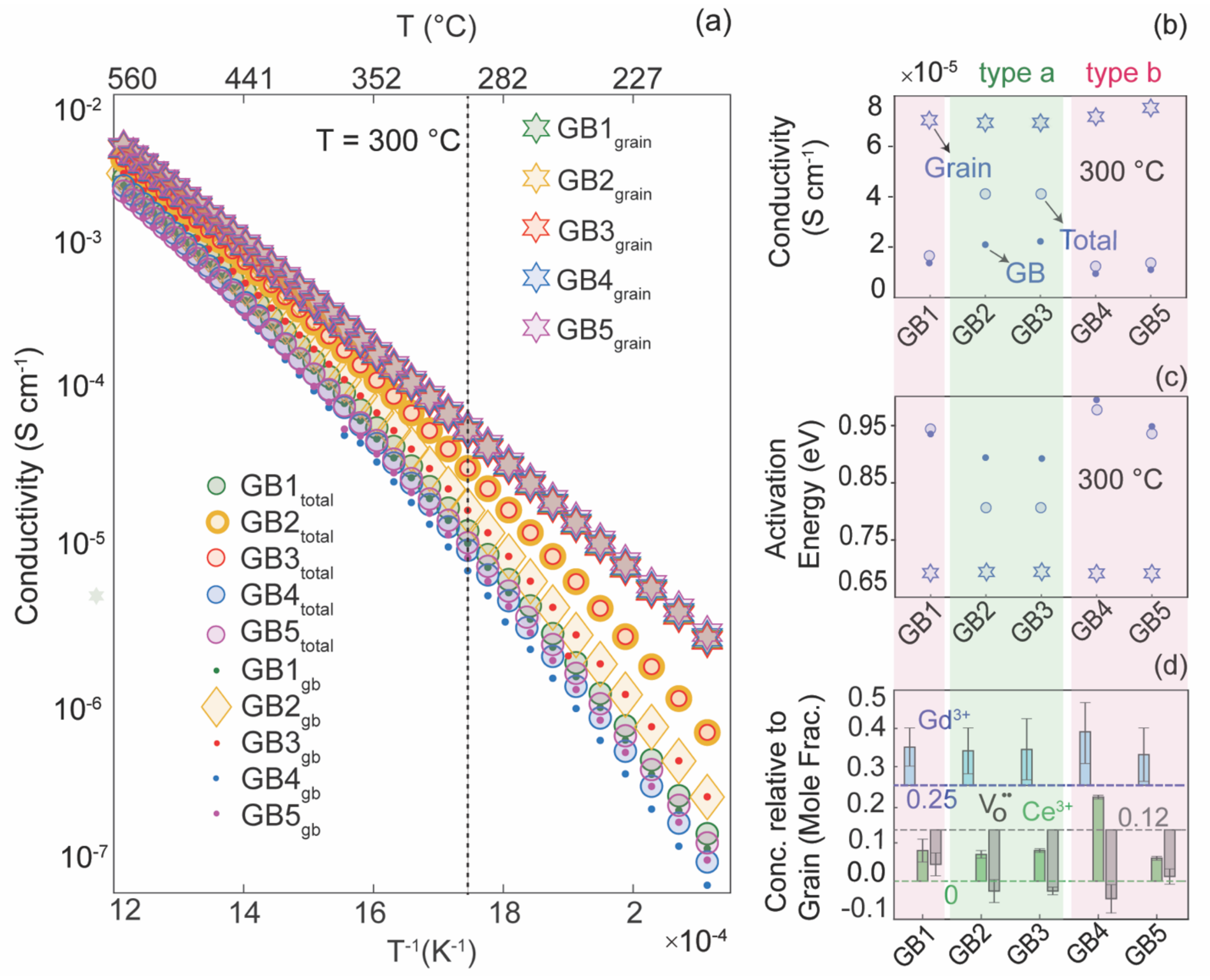

Fig. 3.10. (a) Simulated total (circles), grain (stars), and GB (dots/diamond) conductivities as a function of temperature. (b) Simulated total, grain, and GB conductivity at 300 °C. (c) Total, grain and GB conductivity activation energies calculated at 300 °C from Arrhenius slopes of simulated

conductivities in (a). (d) Concentrations of Gd^{3+}, $V_O^{\bullet\bullet}$ and Ce^{3+} measured by STEM EELS at GBs 1-5; vertical bars indicated the changes relative to the grains.

The differences between grain conductivity predicted in the various hypothetical materials arises from the fact that we are estimating parameters based on spatially resolved characterization of a relatively small STEM specimen (compared with other analytical techniques), in which some grain-to-grain chemical variation is resolvable. The difference in conductivity between grain and total is attributed to the resistance of the GBs, whose conductivity varies from GB-to-GB due to the variation in local defect chemistry. In addition to such variations in real materials, experimental (e.g., grain orientation effects in concentration measurements) and computational measurement errors can exaggerate minimal differences in defect interactions measured in each grain (which vary from one grain to another per Fig. 3.10 b), even though the overall composition of the specimen is G25CO.

Importantly, our GB-resolved experimental defect chemistry measurements and transport property predictions shed new light on the origin of cross-GB resistivity in the concentrated solid electrolyte G25CO. In this case study we concluded that “type b” GBs (GB1, GB4 and GB5) are likely poor ion conductors with relatively high activation energies, while “type a” GBs (GB2 and GB3) are likely better ion conductors with relatively low activation energies. Increased $V_O^{\bullet\bullet}$ depletion is typically cited as the cause of high specific GB resistivity (as exemplified by GB4’s low conductivity and high activation energy, Fig. 3.10 d). However, when considering the entire GB population sampled here, our study suggests the contrary: Minimal or no $V_O^{\bullet\bullet}$ depletion can also lead to high specific GB resistivity (as evidenced by GB1 or GB5). Indeed, if GB resistivity increased monotonically with $V_O^{\bullet\bullet}$ depletion, GB1 and GB5 would be the least resistive and most conductive GBs, which they are not. Importantly, the fact that GB2 and GB3 (with the second and third highest $V_O^{\bullet\bullet}$ depletion) are the most conductive suggests that an optimal amount of $V_O^{\bullet\bullet}$ depletion (~ 0.14 – 0.15 mole fraction) offers low GB resistivity.

Interestingly, neither Gd^{3+} nor Ce^{3+} segregation appear to be independently directly correlated with GB resistivity: For instance, near-equal amounts of both were found in resistive "type b" GBs (GB1 and GB5) and the conductive "type a" GB3. If either Gd^{3+} or Ce^{3+} segregation was directly correlated with GB resistivity, we would expect GB2 and GB3 to behave differently from one another rather than both being type a (and likewise for GB4 and GB5 being type b). Similar arguments hold when considering *both* Gd^{3+} and Ce^{3+} segregation together (i.e., as a charge-compensating pseudo-point-defect complex), allowing us to conclude that a different effect is likely at play in contributing to the local $V_O^{\bullet\bullet}$ depletion. We speculate that this effect is GB character which was not experimentally analysed here; character is the GB atomic structure described by relative grain misorientation angle and plane crystallographic termination, and is known to impact GB space charge potential,[150] conductivity,[84,85] the atomistic pathways of mass transport, and GB solute segregation[151].

3.6 *Conclusions*

We demonstrated a novel experimental-computational framework that predicts which GBs in a polycrystalline solid electrolyte are most likely facilitating ionic conductivity. Our phase-field model is unique in that it its primary inputs are microscopic near-GB point defect concentration profiles—used to predict total, grain, and specific GB ionic conductivity as a function of temperature. Defect-defect interactions in the highly concentrated solid solution are considered, making the framework applicable to other technologically relevant solid electrolytes. In this case, conductivity predictions were powerful in several ways as they identified which experimentally observed GBs are likely ionically resistive (“type b”) and which are conductive (“type a”) and thus facilitate ionic percolation. Model predictions also provided new insights into the cause of GB resistivity, showing that an intermediate amount of $V_O^{\bullet\bullet}$ depletion is directly correlated to maximal GB ion conductivity, in contrast to the idea that GB resistivity increases monotonically with increasing $V_O^{\bullet\bullet}$ depletion. Interestingly neither Gd^{3+} nor Ce^{3+} segregation amount is directly correlated with GB resistivity, suggesting that an additional factor, such as GB character, plays an influential role in defining $V_O^{\bullet\bullet}$ depletion. By elucidating the relationship of GB-to-GB variability in point defect concentrations with ionic conductivity through those GBs, this work lays the foundation for future experimental-computational research and data-driven design of solid electrolytes needed for functional and energy storage/conversion devices.

CHAPTER 4: Reversible Enhancement of Electronic Conduction caused by Phase Transformation and Interfacial Segregation in an Entropy Stabilized Oxide

4.1 Contributions and Acknowledgements

Authors list: Hasti Vahidi[a]*, Alexander D. Dupuy*[a]*, Benjamin X. Lam*[a]*, Justin Cortez*[a]*, Pulkit Garg*[a]*, Timothy J. Rupert*[a]*, Julie M. Schoenung*[a]*, and William J. Bowman*[a]***

[a]*Department of Materials Science and Engineering, University of California, Irvine, Irvine, CA, USA*

Detailed information: HV and WJB devised the study. HV wrote the manuscript and provided the EIS conductivity measurement, STEM characterization data and analysis. BXL contributed to the analysis and interpretation of EIS data. JC, ADD, and JMS provided the pellets, XRD and SEM. PG and TJR performed the DFT simulations and associated calculations. HV and WJB developed the theory and the discussions. All authors reviewed and revised the final manuscript. WJB supervised the study.

Acknowledgements: The authors thank Sossina M. Haile (Northwestern University) and Harry L. Tuller (Massachusetts Institute of Technology) for valuable comments. This research was primarily supported by the National Science Foundation Materials Research Science and Engineering Center program through the UC Irvine Center for Complex and Active Materials (DMR-2011967). WJB and HV acknowledge partial support from the UCI new faculty startup funding. The authors acknowledge the use of facilities and instrumentation at the UC Irvine Materials Research Institute (IMRI) supported in part by the National Science Foundation Materials Research Science and Engineering Center program through the UC Irvine Center for Complex and Active Materials (DMR-2011967).

4.2 Chapter Summary

Entropy stabilized oxide (ESO) research has primarily focused on discovering unprecedented structures, chemistries, and properties in single-phase state. However, few studies discuss the impacts of entropy stabilization and secondary phases on functionality and in particular, electrical conductivity. To address this gap, electrical transport mechanisms in the canonical ESO rocksalt (Co,Cu,Mg,Ni,Zn)O were assessed as a function of secondary phase content. When single-phase, the oxide conducts electrons via Cu^{+}/Cu^{2+} small polarons. After 2 h of heat treatment, Cu-rich tenorite secondary phases form at some grain boundaries (GBs), enhancing grain interior electronic conductivity by tuning defect chemistry towards higher Cu^{+} carrier concentrations. 24 h of heat treatment yields Cu-rich tenorite at all GBs, followed by formation of anisotropic Cu-rich tenorite and equiaxed Co-rich spinel secondary phases in grains, further enhancing grain interior electronic conductivity but slowing electronic transport across the tenorite-rich GBs. Across all samples, the total electrical conductivity increases and decreases reversibly by 4 orders of magnitude with increasing heat-treatment induced phase transformation by tuning the grains' defect chemistry toward higher carrier concentration and lower migration activation energy. This work demonstrates the potential to selectively grow secondary phases in ESO grains and at GBs, thereby tuning the electrical properties using microstructure design, nanoscale engineering, and heat treatment, paving the way to develop many novel materials.

4.3 Introduction

Utilizing configurational entropy as a driving force to stabilize single-phase solid solutions has enabled unprecedented functional materials[152–161] for energy storage/conversion and information technologies[162–168]. Entropy stabilized oxides (ESOs) are a subset of high entropy oxides (HEOs)—themselves a subset of complex concentrated oxides (CCOs)—in which configurational entropy unambiguously governs the stabilization of a single-phase solid solution[169] containing (partially) immiscible constituents[170]. HEOs/ESOs significant promise stems from the compositional complexity and short-range disorder, which offers unique distributions of oxygen-metal bond lengths, bond angles, vibrational frequencies, degree of covalence, and cation coordination numbers,[171] governing functional properties[172,173]. For example, entropy stabilized local disorder was recently shown to create overlapping site energy distributions, facilitating Li^+ mobility through a percolating network[152] in an all-solid-state battery electrolyte.

Despite significant progress, charge transport mechanisms in HEOs/ESOs have not been elucidated given the complexity and many degrees of freedom, particularly for the undoped model systems. While Li-doped ESOs have attracted significant research attention to date, knowledge about transport mechanisms in undoped ESOs is necessary as it underpins the analysis of more complicated doped ESOs. For instance, it is still debated whether the Li-doped $(Co,Cu,Mg,Ni,Zn)_{1-x}Li_xO$ has reasonable electronic conductivity needed for applications including Li^+ battery active electrode materials[166,174].

Additionally, understanding the influence of phase transformations is necessary in elucidating functional properties due to the metastable nature of HEOs/ESOs (i.e., the temperature-dependent competition between entropic and enthalpic phase stabilization), as demonstrated by observed reversible phase transformation in ESOs[159,169]. Balcerzak et al. observed three unique conductivity activation energies in the canonical undoped ESO (Co,Cu,Mg,Ni,Zn)O between 205-875 °C, which was attributed to reversible phase transformations based on lattice parameter changes measured by high-temperature X-ray diffraction (XRD) and phase separation caused by low compatibility of Zn^{2+} and Cu^{2+} with other elements[175]. However, comprehensive understanding of this phenomenon is lacking due to the absence of direct high-spatial-resolution microstructural evidence. Previous XRD results prove that reversible entropic phase transformations can be engineered by varying heat treatment conditions to tune the phase state between the enthalpy dominated multiphase state (comprising Cu-rich tenorite and Co-rich spinel) and the entropy dominated single-phase state[159,169,176,177]. Nonetheless, there are currently no publications explaining how changes in crysal structure, microstructure, and composition influence charge transport and secondary phase particle morphology as an ESO undergoes phase transformations. Moreover, the structure and composition of interfaces such as grain boundaries (GBs) and heterointerfaces (HIs) and their connection with electrical conductivity, as a function of phase transformation, remains unexplored despite the fact that interfacial conductivity is significant for engineering ESO solid electrolytes[130] and thin film transistors[178].

Here, we elucidate the effect of heat-treatment-induced phase transformations on the electrical conductivity of polycrystalline (Co,Cu,Mg,Ni,Zn)O ESO using direct atomic- and nanoscale characterization of structure and chemistry.[179] This composition is a canonical ESO which has been shown to be entropy stabilized by Rost et al.[169] We hypothesized that cations such as Cu or Zn segregate to GBs in the polycrystalline single-phase (Co,Cu,Mg,Ni,Zn)O ESO. This facilitates the formation of (previously reported) secondary phases, which may form at GBs and/or in grain interiors. These secondary phases affect the ESO's electrical transport mechanism(s) though the altered point defect chemistry of grain interiors and GBs. Finally, we hypothesized that the structure and composition of HIs in ESOs is relevant to secondary phase morphology and overall charge transport, and should be considered when designing/fabricating electronic devices such as thin films with optimized HI properties[180].

To test our hypothesis, we used heat treatment to control the formation of a multiphase microstructure comprising ESO grains with inter/intragranular secondary phase particles. We quantified the structure and composition of single-phase and multiphase ESOs, and their GBs and HIs using atomic-resolution scanning transmission electron microscopy (STEM) imaging and (sub-)nanoscale spectroscopy by energy dispersive X-ray spectroscopy (EDS) and electron energy-loss spectroscopy (EELS). While GBs have been recently studied in CCOs,[181,182] to our knowledge this is the first report of sub-nanometer chemical composition and atomic structure of *ESO* GBs and HIs, which is necessary as these planar defects are inevitable in the large-scale production of ceramic oxides[130,183]. Experimental observations of GB segregation were interpreted with the assistance of density functional theory (DFT) calculations, though the complexity of the GBs observed precluded a general fundamental understanding of atomistic segregation mechanisms. Importantly, secondary phase formation influences defect chemistry, which introduces new charge carriers and changes the electrical transport measured here by electrochemical impedance spectroscopy (EIS). Detailed exploration of GBs and HIs revealed that GBs are key in the microstructure formation and conductivity mechanisms while HIs define secondary particle shape within ESO grain interiors. These findings deepen our basic understanding of structure-function-processing relationships in an emerging class of highly promising materials which will guide the design and engineering of ESO compositions with tunable microstructure, electrical conductivity, and composite-derived multifunctionalities for a broad range of applications.

4.4 Materials and Methods

4.4.1. Synthesis and Sintering

(Co,Cu,Mg,Ni,Zn)O ESO nanopowders were synthesized via solid-state methods using CoO (50 nm particle size, 99.7 wt. % purity), CuO (25-55 nm, 99.95 %), MgO (50 nm, 99.95 %), NiO (18 nm, 99.98 %), and ZnO (18 nm, 99.95 %) from US Research Nanomaterials Inc (Houston, TX, USA). Starting constituent oxides were blended in equimolar amounts using a mortar and pestle, followed by planetary ball milling (Fritsch GmbH, Idar-Oberstein, Germany) for 3 h using a silicon nitride jar and milling media with the powder suspended in isopropanol. Conventional and spark plasma sintering (SPS) were used to consolidate the blended oxide nanopowders into fully dense, bulk pellets with varying grain sizes. Conventional sintering was done inside an elevator furnace using 1100 °C for 12 h (CM Furnaces, Bloomfield, NJ, USA). SPS was done using a Fuji model 825 SPS at 900 °C under a pressure of 100 MPa for 2 h. Microstructure and crystal structure of pellets were studied using XRD (Ultima III, Rigaku, Tokyo, Japan) and scanning electron microscopy (SEM) (Magellan 400, Thermo Fisher Scientific, Waltham, Massachusetts).

4.4.2. Heat Treatment

Based on our previous work[159], this ESO forms a single-phase structure when heat treated and quenched from temperatures above 850 °C. If the single-phase ESO is then heat treated and quenched from the temperature range of 650-850 °C, a multiphase ESO forms. It was observed that heat treatments at 700 °C exhibit higher secondary phase content formation, yielding a maximum of ~17 at. % Cu-rich phase and ~11 at. % Co-rich phase[177]. In this study, one pellet was kept in the as-sintered single-phase form and two other pellets were heat treated for 2 and 24 h at 700 °C to produce multiphase ESOs with varying secondary phase content. The pellets are labeled as ESO-single, ESO-2h and ESO-24h.

4.4.3. Electrochemical Impedance Spectroscopy

AC electrochemical impedance spectroscopy (EIS) was used to measure the electrical conductivity and activation energies for ESO-single, ESO-2h, and ESO-24h. We measured conductivity at temperatures 25-200 °C to avoid inducing phase transformations (which occur at higher temperatures) during EIS. O^{2-} non-blocking porous electrodes were fabricated using Ag paste (Fuel Cell Materials, Columbus, OH) that was applied on the polished surfaces of all pellets and annealed at 400 °C for 1 h. EIS was performed in air using a BioLogic SP-200 potentiostat (BioLogic Sciences Instruments, Seyssinet-Pariset, France). An excitation voltage of 50-150 mV over the frequency range of 1 mHz-7 MHz was used. Pellets were heated from 25-200 °C (in 50 °C increments) inside a HFS600E-PB4 probe stage with a T96 system controller (Linkam Scientific Instruments, Redhill, United Kingdom).

Impedance data were collected at each dwelling temperature after the impedance response became stable over time. Nyquist plots were fit to equivalent circuit models containing one or two parallel resistor-constant phase element (RQ) subcircuits (Z-fit mode in BioLogic's EC-Lab). Here, *Q* represents the constant phase element, with each RQ subcircuit corresponding to a specific electrochemical response. The Nyquist plots from ESO-single and ESO-2h were fit to a single RQ circuit model, representing pellet total resistance. The Nyquist plots from ESO-24h were fit to a 2RQ circuit model, representing two different resistance contributions in the form of two overlapping arcs. Eq. 4.1 was used to calculate the total and grain interior conductivity:

$$\sigma = \frac{L}{AR} \qquad \text{Eq. 4.1}$$

where L and A are pellet thickness and cross-section area, respectively. For total conductivity, R is total pellet resistance (i.e., the diameter of the grain interior/bulk arc plus grain boundary arc in Nyquist plots). For grain conductivity, R is the diameter of just the grain interior/bulk arc. The specific GB conductivity for ESO-24h was calculated using Eq. 4.2:

$$\sigma_{GB} = \frac{L}{AR}\left(\frac{g}{G}\right) \qquad \text{Eq. 4.2}$$

where g and G are GB thickness and pellet average grain size, respectively. Conductivity activation energies were calculated using the slopes of the Arrhenius conductivity plots with Eq. 4.3:

$$\sigma = \frac{\sigma_0}{T}\exp\left(\frac{-E_a}{k\,T}\right) \qquad \text{Eq. 4.3}$$

where σ is conductivity, σ_0 is the conductivity pre-exponential factor, E_a is the activation energy of charge transport, k is the Boltzmann constant, and T is absolute temperature.

4.4.4. TEM Sample Preparation

Aberration-corrected STEM was used to characterize the structure and composition of grain interiors and selected GBs in ESO-single, as well as atomic structure, composition, and morphology of the secondary phases formed during heat treatments in ESO-2h and ESO-24h. TEM samples of ESO-single, ESO-2h, and ESO-24h were prepared by focused ion beam (FIB) lift-out in a dual-beam SEM/FIB (Tescan, Kohoutovice, Czech Republic) equipped with Ga^+ focused beam.[184] To protect the TEM sample from ion-beam damage, a 2 µm thick platinum layer was deposited on each surface.

4.4.5. STEM Energy-Dispersive X-ray Spectroscopy and Electron Energy-Loss Spectroscopy

Atomic-resolution scanning transmission electron microscopy (STEM) in high-angle annular dark-field (HAADF), medium-angle annular dark-field (MAADF), and bright-field (BF) modes as well as energy-dispersive X-ray spectroscopy (EDS), and electron energy-loss spectroscopy (EELS) were performed using a JEOL Grand ARM300CF (200-300 KeV, JEOL Tokyo, Japan). Fast Fourier Transform (FFT) patterns calculated from atomic-resolution images were used to identify the crystal structures. Microscope data were processed using Gatan Digital Micrograph (Gatan, Pleasanton, CA). EELS and EDS backgrounds were subtracted using the Hartree-Slater cross-section and Kramers background correction mode in Digital Micrograph, respectively. The following peaks were used for the analysis: O K_α (0.525 keV), Mg K_α (1.254 keV), Ni K_α (7.480 keV), Co K_α (6.931 keV), and K_β (7.649 keV), Cu K_α (8.046 keV) and K_β (8.904 keV), and Zn K_α (8.637 keV) and K_β (9.570 keV). STEM EDS is used to identify the chemical composition of bulk and GBs in ESO-single, as well as secondary phase particles and GBs in ESO-2h and ESO-24h. STEM EELS is used to quantify the stoichiometry of secondary phase particles and the distribution of cations across HIs.

4.4.6. Density Functional Theory Calculations

First-principles calculations were performed within the DFT framework using the Vienna ab initio simulation package (VASP)[185,186] within the generalized gradient approximation (GGA) using the Perdew−Burke−Ernzerhof for solids (PBEsol) exchange−correlation functional.[187] Projector augmented wave (PAW) pseudopotentials with a plane-wave cutoff energy of 600 eV were used for all the calculations. The magnetism of Co, Cu, and Ni was treated with the PBEsol collinear spin density approximation in the GGA with a Hubbard U (GGA + U) scheme[188–190]. The Coulomb parameter (U) was applied for these elements to account for the increased Coulomb repulsion between the semi-filled 3d states. U = 6 was used, as this value can obtain correct ground state phases for the oxides of transition metals considered here. Spin-polarized calculations were performed where the magnetic moments of Co, Cu, and Ni in the rocksalt phase were initiated in the antiferromagnetic II type state. The equilibrium bulk ESO rocksalt structure was determined using the Monkhorst-pack k-point mesh[191] with convergence energy of 10^{-5} eV atom^{-1} and convergence atomic force of 0.01 eV Å^{-1}. The computed lattice parameter of bulk ESO rocksalt is 4.23 Å, which matches very well with our experimentally observed value of 4.1-4.2 Å.

To understand the experimentally observed clustering of Cu at GBs in rocksalt (Co,Cu,Mg,Ni,Zn)O ESO, a Σ5 (310) GB is examined in the ESO rocksalt. This interface was chosen as a model boundary because it has multiple different potential segregation sites and has been commonly examined to understand different GB properties in a variety of metals[192–197] and metal oxides[198–200] due to its high symmetry and low energy structure. The simulation cell had dimensions of $41.78 \times 4.26 \times 6.85$ Å^3 and contained 120 atoms including 60 metal atoms in equiatomic concentration and 60 oxygen atoms. The atoms were relaxed at their positions using a gamma-pack k-point mesh to an energy convergence of $<10^{-5}$ eV while maintaining a constant volume and shape of the GB sample. The GB energy (E_{gb}) was calculated as the difference between the energy of the GB simulation cell (E) and the energy of equilibrium ESO rocksalt (E_{bulk}) with the same number of atoms per unit area of the GB plane (S) using Eq. 4.4:

$$E_{gb} = \frac{E - E_{bulk}}{2S} \qquad \text{Eq. 4.4}$$

To examine the clustering of Cu ions at the GB, different GB samples were prepared with 16.66, 33.33 and 50 at. % Cu-ions in the GB region while maintaining an equiatomic concentration of metal ions in the overall simulation cell. GB concentration is calculated as the number of Cu-ions divided by the total number of metal ions in the GB region. Each of the samples was energetically relaxed to obtain an equilibrium structure, followed by GB energy calculation using Eq. 4.3.

4.5 Results and Discussion

4.5.1. Homogeneous Bulk Composition and Copper Segregation to the Grain Boundaries in Single-phase ESO

It is well known that GBs can play a governing role in a ceramic's overall electrical properties[4,6,130,183,201,202]. To shed light on the conduction mechanisms in single-phase (Co,Cu,Mg,Ni,Zn)O, atomic/nano scale structure and chemical composition of grain interior and GBs were investigated. We first confirmed the homogeneity of all cations and O^{2-} in grain interior using XRD, SEM, and STEM EDS (Fig. 4.1 a-c). Next, segregation of Cu and a Si- and Ca-rich amorphous phase to the GB was detected, which is a common result of ceramic fabrication. A representative elemental distribution profile across a GB demonstrates two ~ 1 nm thick layers of Cu segregated to the two sides of the GB planes, while the amorphous phase segregates to the GB core (Fig. 4.1 d). CuO is not stable in the rocksalt structure due to a degeneracy in the electronic configuration and prefers to crystallize into a tenorite crystal structure. This degeneracy leads to a Jahn-Teller effect and a distortion in the (Co,Cu,Mg,Ni,Zn)O crystal structure,[203,204] causing some Cu ions to segregate from grain interiors to GBs to minimize the free energy, allowing the entropy-stabilization of a single-phase rocksalt ESO. Our DFT results support this claim by showing that GB energy decreases as the Cu ions in the crystal interior preferred to occupy the distorted GB sites in a single-phase rocksalt ESO. While this is not an exact simulation of the experimentally observed interface (the complex structure of an amorphous Si-rich film cannot be captured with DFT), it demonstrates that Cu ions prefer to occupy crystallographically disordered defect sites which is consistent with the observation of Cu ions adjacent to the GB in the TEM measurements. The amorphous GB phase at the GBs is made of raw material impurities, which is typically observed to block ion transport in polycrystalline ceramics[205]. However, as discussed below, importantly we do not observe any impedance response attributable to this intergranular phase, and thus we assume the GBs in ESO-single do not contribute an impedance response to the sample's overall response.

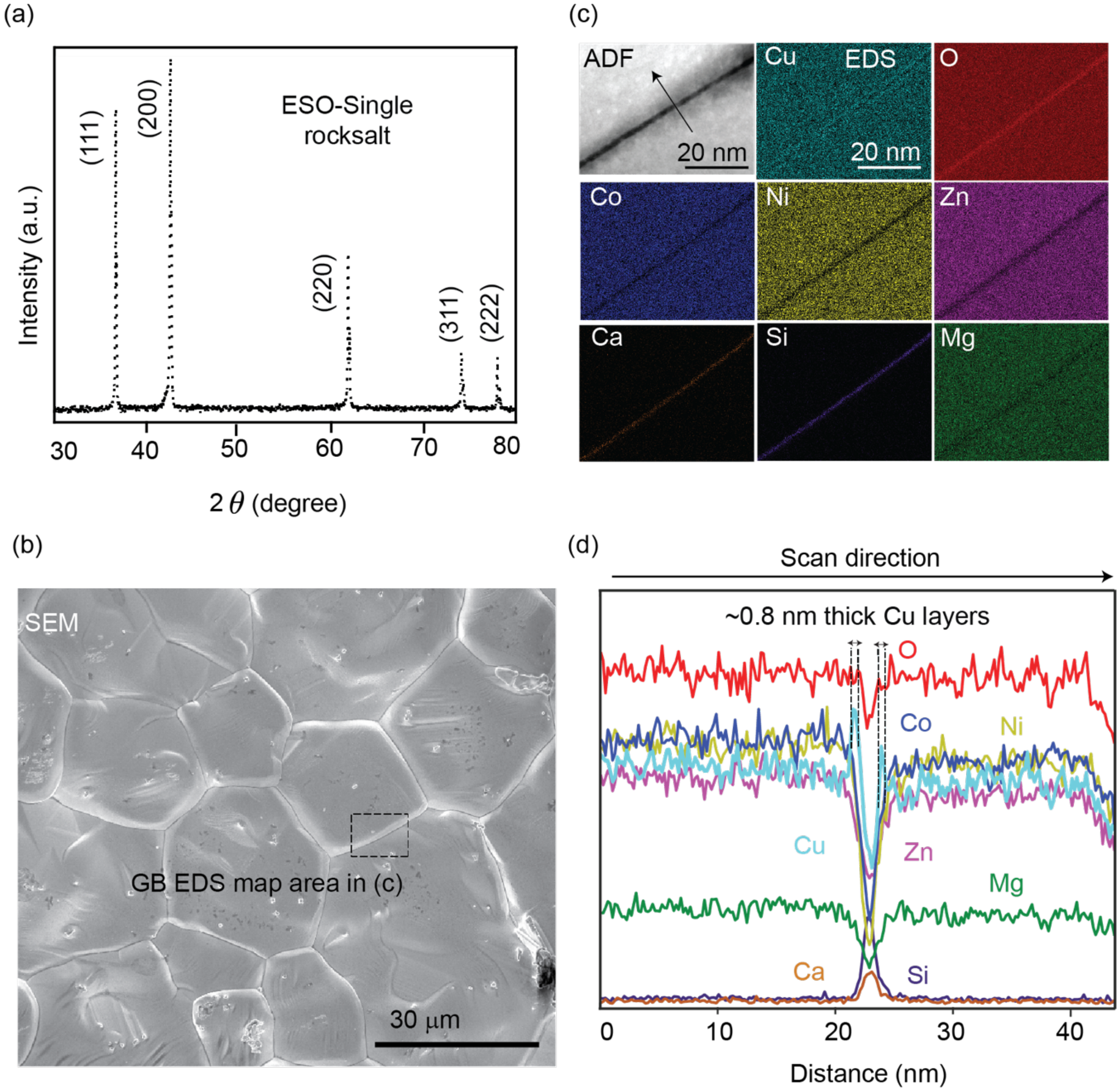

Fig. 4.1. Segregation of Cu to GBs in single-phase ESO. a) XRD shows that ESO-single has a rocksalt crystal structure: Fm$\bar{3}$m (225) ICSD – 52026. b) SEM image of ESO-single. c) STEM-EDS chemical mapping of a GB demonstrating Cu and Si-rich GB phase. d) Elemental distribution across the GB mapped in b.

4.5.2. Formation of Intragranular and Intergranular Secondary Phase Particles in Heat Treated ESOs

ESOs undergo a reversible phase transformation during heat treatment, forming Cu-rich and Co-rich oxide particles[206]. The heat treatment temperature used to form the multiphase state (700 °C) is low enough that the Gibbs free energy of the single-phase state is insufficient to overcome the Gibbs free energy of the multiphase state. We therefore propose that our multiphase samples are enthalpy stabilized, while our single-phase sample is entropy stabilized. To understand the effect of heat treatments on the atomic/nanoscale composition, structure, and morphological features of the secondary phases, 2 h and 24 h heat treated ESO pellets were explored using XRD, STEM imaging, EDS, EELS in Fig. 4.2. In the ESO-2h, XRD shows secondary phase peaks related to tenorite and spinel structures (Fig. 4.2 a). Using STEM-EDS, we observed the formation of nanoscale intergranular Cu-rich oxide particles at some GB sites, as well as the homogeneous distribution of all elements in the grain interiors, Fig. 4.2 b. The Cu-rich particles mainly consist of Cu and O, with some Mg and Zn, quantified using STEM-EELS (section 4.5.3). Cu segregating was still observed at the GBs not covered with secondary phases suggesting that as the ESO is annealed, Cu segregates to the GBs, facilitating the formation of the entropy stabilized single-phase ESO. The formation of Cu-rich secondary phases is also expected to produce adjacent Cu depletion zones in the grains[176,207].

The XRD results from ESO-24h show a larger number of secondary phase peaks with higher intensities (with respect to ESO rocksalt primary peaks) related to tenorite and spinel structures (Fig. 4.2 c). Additionally, intragranular Cu-rich and Co-rich oxide particles form in the grain interiors, Fig. 4.2 d. It is hypothesized that after Cu layer formation, Cu-rich secondary phase particles cover all the GBs, creating Cu depletion zones in the grains directly adjacent to particle-covered GBs[176,207]. Cu-rich secondary phase particles continue to nucleate and grow throughout grain interiors, where Cu has not been depleted. For the Co-rich particles, it is hypothesized that Co can fill the Cu vacancies ($V_{Cu}^{//}$) created during the formation of Cu-rich particles, which increases local Co concentration and enables the nucleation of Co-rich particles. As discussed below, Cu-rich, and Co-rich oxide particles grow into anisotropic needle-like and equiaxed morphologies, respectively.

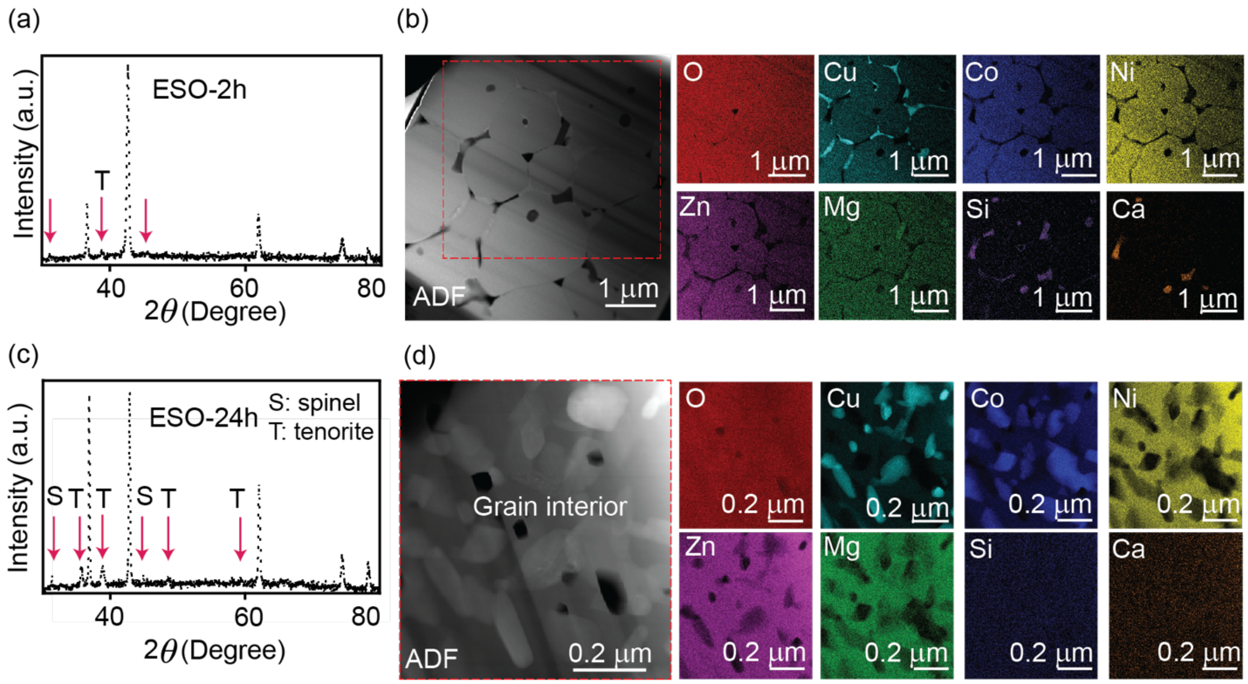

Fig. 4.5. Formation of Cu-rich and Co-rich oxide secondary particles in multiphase ESOs. a) XRD of ESO-2h showing peaks of secondary phases (CuO tenorite: $Fm\bar{3}m$ (225) ICSD – 52026 and Co_3O_4 Spinel: $Fd\bar{3}mS$ (227) ICSD – 36256). b) ADF STEM and EDS chemical maps of grains indicating the homogenous distribution of cations and oxygen and intergranular Cu-rich tenorite particles in ESO-2h. c) XRD of ESO-24h showing more visible peaks of secondary phases. d) ADF STEM and EDS chemical maps of a grain interior showing Cu-rich and Co-rich secondary phase particles inside grains after 24 h of heat treatment at 700 ºC.

The crystal structure of phases was determined by atomic-resolution HAADF imaging performed at a triple junction of ESO grain interior/Cu-rich oxide phase/Co-rich oxide phase in

ESO-24h, Fig 4.3 a. FFT patterns calculated from the HAADF image confirm that Cu-rich and Co-rich secondary phases have tenorite and spinel crystal structures, Figure 3b-d.

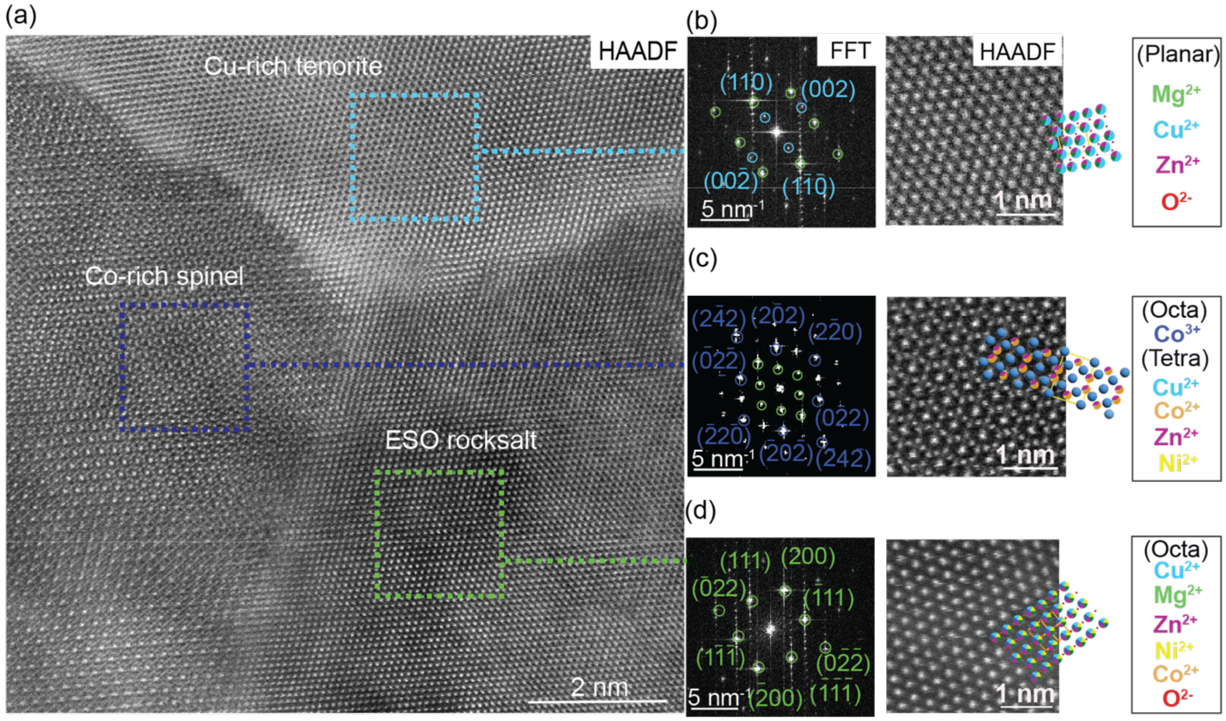

Fig. 4.6. Atomic structure of a triple junction in ESO-24h. a) HAADF STEM image of ESO grain interior/Cu-rich tenorite/Co-rich spinel triple junction. b-d) Indexed FFT patterns, atomic-resolution HAADF micrographs, and atomic model overlays of b) Cu-rich tenorite, c) Co-rich spinel and d) ESO rocksalt grain interior.

4.5.3. Structure and Chemical Composition of Heterointerfaces and Their role in Secondary Phase Particle Morphology

To reveal the role of HIs in the phase transformation and conductivity, the atomic structure and chemical composition of the ESO-24h HIs were investigated. We observed that Cu-rich tenorite phase often adopts a needle-like morphology, with straight sides and curved tips (Fig. 4.4). Given the differences in the crystal structure and atomic arrangements of Cu-rich tenorite and grain interior ESO rocksalt (cubic), misfit strain is expected at both HIs. Atomic-resolution HAADF STEM images confirmed that needle tips were semi-coherent and curved, with a lattice mismatch of ~5% (Fig. 4.4 c). This value agrees with the misfit values reported for semi-coherent HIs in metals[208] and ceramics[209]. The higher lattice mismatch at needle tips compared to the sides is compensated for by the formation of edge dislocations. Edge dislocations allow for faster cation diffusion across needle tips compared to the sides, elongating the needle-like morphology as the secondary phases grow. Two sets of edges dislocations were detected at this HI using MAADF and BF imaging. The first dislocation set with the Burgers vector, $\overrightarrow{\boldsymbol{b1}}$, is parallel to the HI with a dislocation spacing of 5 nm. The second dislocation with the Burgers vector, $\overrightarrow{\boldsymbol{b2}}$, is perpendicular to the HI with a dislocation spacing of 4 nm. The existence of two non-parallel sets of dislocations partly relieves the interfacial coherency strain, while maintaining the residual long-range strain[210]. The incoherent (distorted) areas are the dark regions visible in the STEM BF micrograph.

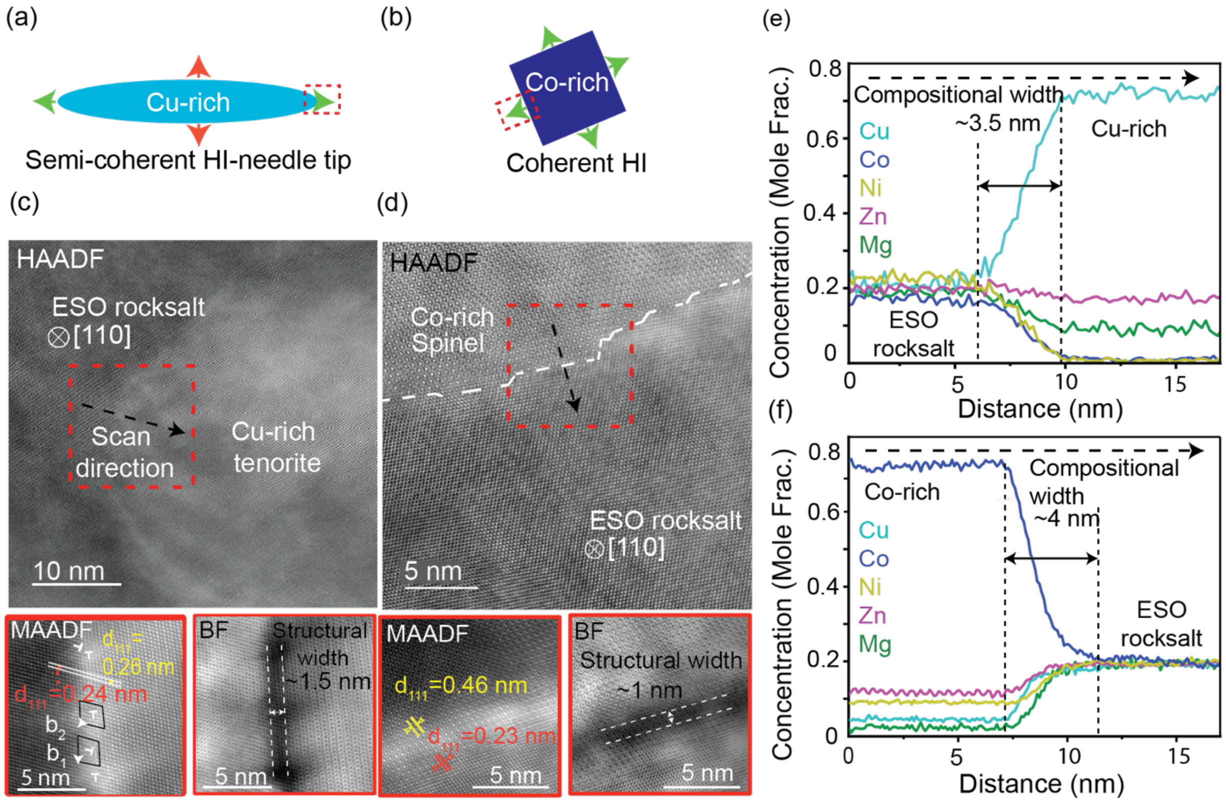

Fig. 4.4. Coherent and semi-coherent HIs with no elemental segregation or depletion in ESO-24h. Atomic structure and composition of two HIs and their correlation to secondary phase particle

morphology. a) The needle-like morphology of a Cu-rich tenorite particle. b) The equiaxed morphology of a Co-rich spinel particle. c) HAADF/BF STEM images of a tenorite/ESO HI at a needle tip, with expanded views of the red dashed zone. d) HAADF STEM image of a spinel/ESO HI with expanded views of red dashed zone in MAADF and BF modes. e) STEM-EDS cation composition profile across the tenorite/ESO HI at needle tip f) STEM-EDS cation composition profile across the spinel/ESO HI.

Unlike Cu-rich tenorite needles, Co-rich spinel particles form equiaxed morphologies with one HI type (Fig. 4.4 b), which is a coherent HI with some lattice misfit strain. Even though the Co-rich spinel and ESO rocksalt phases are both cubic, differences in lattice parameters and atomic arrangements cause a misfit strain of ~1 %. Therefore, variations in contrast observed at this HI in MAADF and BF modes (diffraction and strain contrast), suggest the existence of misfit-induced elastic strain (Fig. 4.4 d).

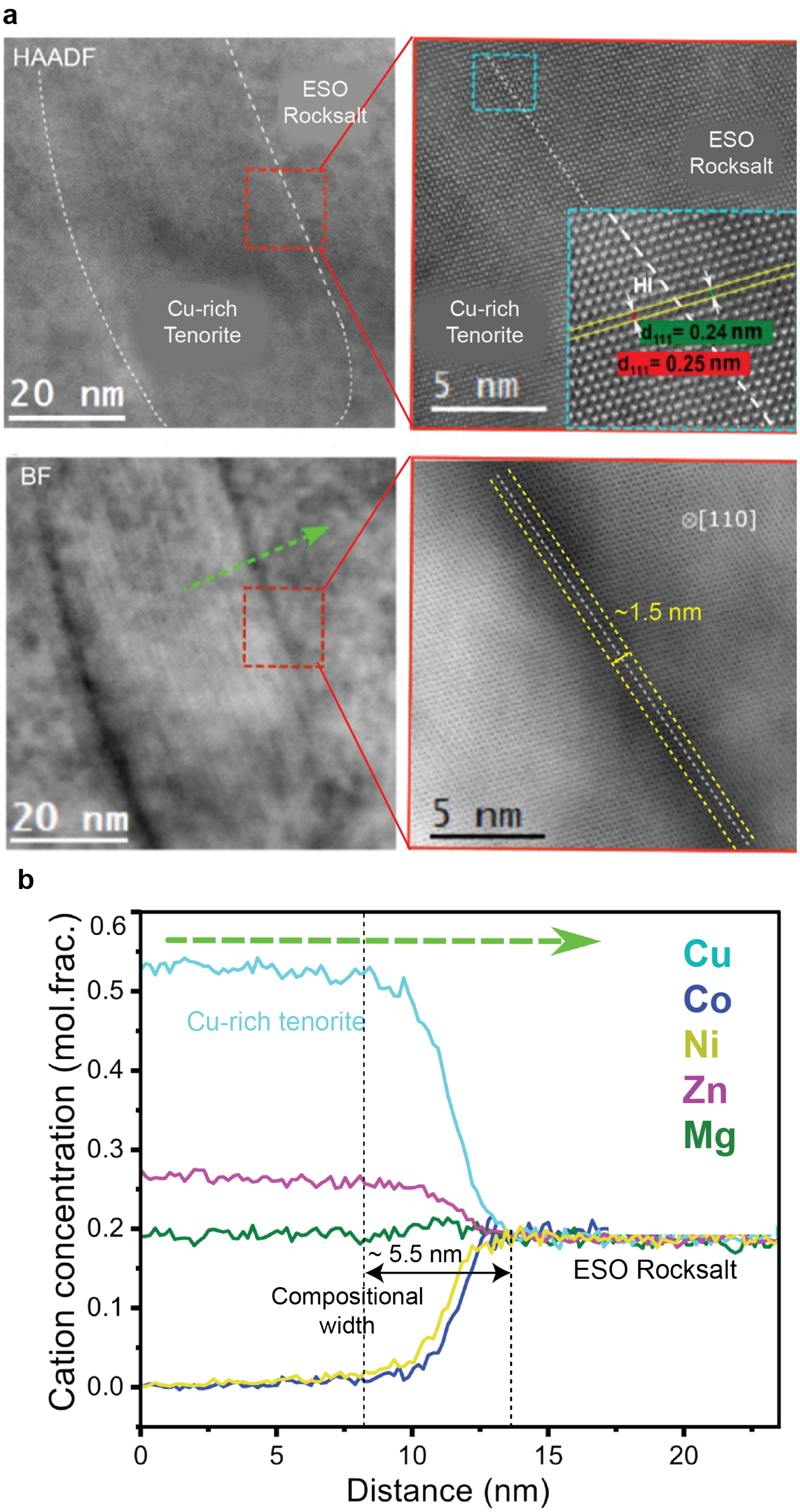
a
HAADF
ESO
Rocksalt
Cu-rich
Tenorite
20 nm
ESO
Rocksalt
Cu-rich
Tenorite
5 nm
HI
d_{111}= 0.24 nm
d_{111}= 0.25 nm
BF
20 nm
⊗[110]
~1.5 nm
5 nm
b
Cation concentration (mol.frac.)
0.6
0.5
0.4
0.3
0.2
0.1
0.0
Cu
Co
Ni
Zn
Mg
Cu-rich tenorite
~ 5.5 nm
Compositional
width
ESO Rocksalt
0
5
10
15
20
Distance (nm)

Fig. 4.5. Coherent HIs with no elemental segregation or depletion. (a) Atomic-resolution HAADF and BF micrographs of HI at needle sides. (b) STEM-EDS cation composition profile across Cu-rich tenorite/ESO rocksalt HI at needle side.

No segregation or depletion of cations is detected at either HI using STEM EELS, suggesting a smooth transition from one phase to the other at the needle tip (Fig. 4.4 e), spinel/ESO HI (Fig. 4.4 f), and needle side (Fig. 4.5). Therefore, we conclude that the contrast variations are solely related to lattice distortion. All HIs observed in this study have wider (~3-5.5 nm) compositional widths—the distance over which there is a composition gradient, than structural widths (1-2 nm)—the distance over which there is lattice distortion caused by the interface (Fig. 4.4 c). The considerably larger compositional width is a known characteristic of diffuse HIs seen in phase transformed CCMs such as precipitate-hardened high-temperature alloys[211,212]. The wider compositional widths at the ESO HIs are attributed to the longer range diffusion of ions in ESOs due to the distorted nature of the crystal structure at the atomic level[213].

Using STEM EELS, the stoichiometry of the Cu-rich tenorite phase at the needle tip was measured to be $Cu_{0.78}Mg_{0.09}Zn_{0.19}O$, which we speculate forms by simultaneous co-segregation of Cu, Mg and Zn. The stoichiometry measured at the needle side was $Cu_{0.53}Mg_{0.2}Zn_{0.27}O$, suggesting slight changes in Mg and Zn dissolution in CuO leading to a composition gradient across the needle-like particle, which we attribute to the interaction between strain, cation solubility, and diffusivity across the HI;[193,196,212,214] while this has not been elucidated in the literature, it could provide additional degrees of secondary phase tunability. Negligible signals detected from Co and Ni suggest their absence in the tenorite phase. The stoichiometry of the Co-rich spinel phase was measured to be $Co_{2.54}Cu_{0.02}Ni_{0.06}Zn_{0.38}O_4$. For quantified stoichiometries of secondary phase particles, see Table 4.1.

Table 4.1. Stoichiometry of cations (mole %) in Cu-rich tenorite side/tip and Co-rich spinel secondary phases measured using STEM-EELS

Cation	Cu-rich needle tip (mole %)	Cu-rich needle side (mole %)	Co-rich (mole %)
Cu	73	53	0.6
Co	—	—	81.6
Ni			1.8
Zn	19	27	12.6
Mg	8	2	—

4.5.4. Changes in Electrical Conductivity and Activation Energy with Heat-Treatment-Induced Phase Transformations

To investigate the relationship between microstructure and conduction mechanism, the electrical conductivity of ESO-single, ESO-2h, and ESO-24h pellets were determined using AC impedance spectroscopy and equivalent circuit model fitting. Porous O^{2-} permeable fired Ag paste was used as electrodes. The Nyquist plots of ESO-single only exhibit one “RQ” arc, attributed to the total impedance response of the pellet (grains and GBs), Fig. 4.6.

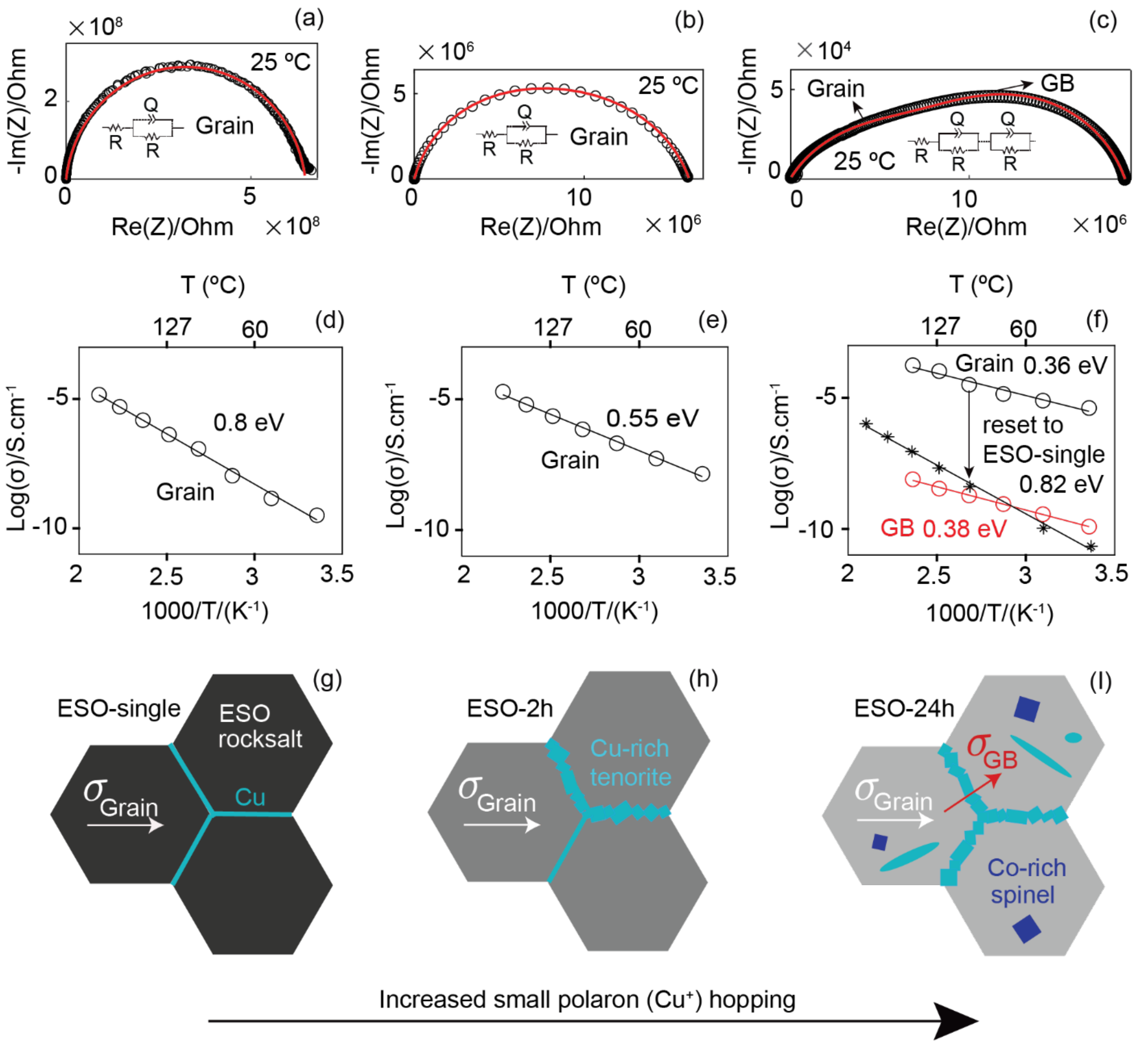

Fig. 4.6. Electrical conductivity of single and multiphase ESOs with respect to the atomic/nano-scale structure and composition. Representative Nyquist plots collected from a) ESO-single, b) ESO-2h and c) ESO-24h at 25°C. Log_{10}(conductivity) as a function of temperature for all three pellets, with Ag electrode for d) ESO-single and e) ESO-2h and f) ESO-24h. Proposed conductivity pathways in g) ESO-single, h) ESO-2h and i) ESO-24 h.

This suggests that the GBs (Fig. 4.1) do not form a space charge layer that would show up as a second distinct arc. Based on the slope of the conductivity as a function of inverse temperature (Fig. 4.6 d), an activation energy of 0.80 eV is calculated for charge transport in the distorted rocksalt grain interiors from Arrhenius plots of conductivity (Fig. 4.7).

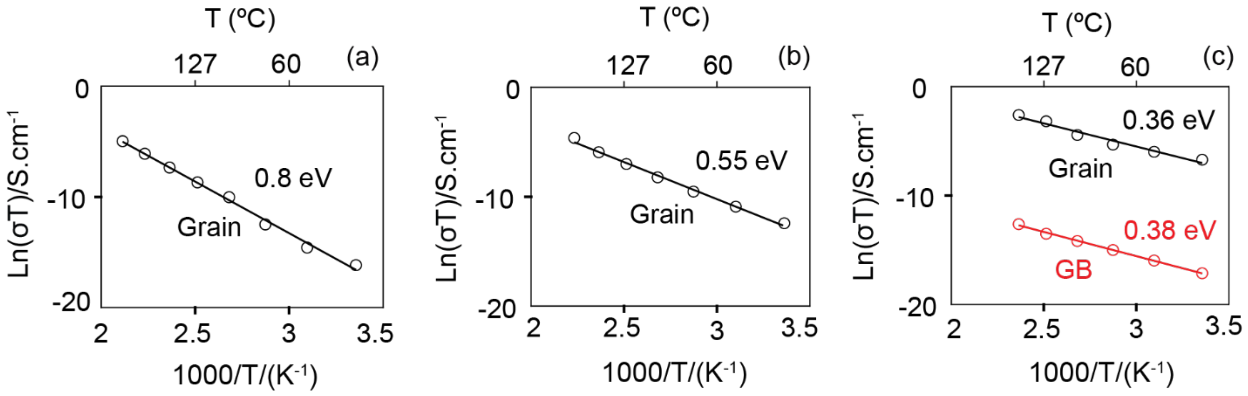

Fig. 4.7. Arrhenius plot of conductivity as a function of inverse temperature for all three pellets, with Ag electrode for a) ESO-single and b) ESO-2h and c) ESO-24h.

We attribute conductivity in this sample to electronic hopping between reduced Cu polarons, Cu'_{Cu} which are known from DFT to accommodate oxygen sub-stoichiometry[215]. Compositional complexity in ESOs is known to facilitate the formation of localized charges. For example, Cu^+ is known to exist in this rocksalt ESO given the relatively weak Cu-O bonds, according to DFT, X-ray photoelectron spectroscopy (XPS) and anion sublattice distortion measurements[215,213,216]. Moreover, the starting binary oxides are strongly insulating (MgO)[217] or p-type (CuO[218,219], CoO[220], NiO[221,222]) and n-type (ZnO)[223] semiconductors within the 25-200 °C temperature range used for conductivity measurements in this work (Table 4.2), supporting our assumption that transport is electronic. As shown below, the 0.8 eV conductivity activation energy for Cu^+/Cu^{2+} polaron hopping in ESO-single is relatively high compared to the 2h and 24h samples (Fig. 4.6 e-f), which we believe stems from the relatively low Cu^+ polaron concentration and concomitant relatively large polaron separation distance, as well as defect association effects between Cu^+ and oxygen vacancies that increase the polaron migration barrier.[224] To assess the possible impact of entropy stabilization on electronic conductivity, the ESO's electronic conductivity is compared to that of the starting binary oxides, Table 4.2. ESO-single's conductivity is within the range of values for the binary oxides, suggesting that entropy stabilization does not play a decisive role in governing the electronic conductivity of this ESO.

Table 4.2. Electrical conductivity and conductivity activation energy values measured for ESO and small polaron hopping in binary transition metal oxides from literature.

Oxide (carrier)	**Conductivity (S/cm)**	**Activation energy (eV)**	**Temperature (°C)**	**References**
ESO (Cu^{+}/Cu^{2+} n-type small polaron)	3×10^{-10}	0.8	25	This work
CuO (p-type semi.)	4×10^{-2}	0.21, 0.31 0.27 across GB	30	Singh, *Appl. Surf. Sci.* (2011) Younas, *Appl. Phys. Lett.* (2012)
CoO (p-type semi.)	6.3×10^{-10}	0.68	25 (extrapolated)	Lange, *Ber. Buns. Phys. Chem.* (2010)
NiO (p-type semi.)	10^{-5}	0.46	25 (extrapolated)	Qiao, *Europhys. Lett.* (2011) Mitoff, *J. Chem. Phys.* (1961)
ZnO (n-type semi.)	5×10^{-9}		1100	Wang, *Powder Tech.* (2013)
MgO	10^{-15}	2.8	227	Lewis, *J. Phys. D* (1968)

Like ESO-single, the ESO-2h Nyquist plots were best fit to an R-RQ circuit model (Fig. 4.6 b) attributed to the rocksalt grain interior contribution. A conductivity activation energy of 0.55

eV is calculated for ESO-2h (Fig. 4.6 e), which is consistent with that of Cu^{+}/Cu^{2+} small polaron hopping reported previously in this ESO (Table 4.2)[225–227]. In ESO-2h, formation of Cu-rich tenorite particles at GBs requires the formation of copper vacancies, $V_{Cu}^{//}$, in the grains that are charge compensated by oxygen vacancies, $V_{O}^{\cdot\cdot}$, which are known (from DFT[215]) to form preferentially as nearest neighbors to Cu^{+}. Increasing the $V_{O}^{\cdot\cdot}$ concentration in the ESO grains thus increases the concentration of Cu^{+} and lowers the small polaron site separation distance, leading to a measured electronic conductivity enhancement of ~2 orders of magnitude at 25 °C.

For ESO-24h, the two overlapping arcs detected at higher and lower frequencies are fit to a series R-RQ-RQ circuit, with each RQ corresponding to grain interior or GBs, respectively (Fig. 4.6 c). The measured grain interior conductivity activation energy is 0.36 eV (Fig. 4.6 f), attributed to Cu^{+} small polaron hopping caused by further increased $V_{O}^{\cdot\cdot}$ concentration as in the ESO-2h. This is due to further depletion of Cu and Co upon secondary phase formation. Assuming the intensity of main XRD peaks are proportional to the volume fraction of each phase, the formation of Cu-rich tenorite particles at GBs and Cu-rich tenorite and Co-rich spinel particles in grain interiors may increase the concentration of Cu site vacancies by up to 6 % and the Co site vacancies by up to 2 % relative to the pristine ESO rocksalt. We believe the Cu-rich and Co-rich particles do not contribute to the grain interior conductivity because they are isolated within the grains and facilitate charge carriers of the opposite charge (p-type in CuO and CoO versus n-type in ESO[218,220]). Therefore, we conclude that the enhanced ESO grain interior electronic conductivity of ~ 4 orders of magnitude compared to ESO-single is due to changes in grain interior defect chemistry caused by additional Cu-rich tenorite formation at GBs, as well as Cu-rich tenorite and Co-rich spinel secondary phase particles in grains[228].To demonstrate the defective state of grain interiors in ESO-24h, we used the relative intensities of the primary peaks in XRD of ESO-24h

(Fig. 4.8) to calculate the amount of Cu and Co atoms that leave the grain interior upon formation of secondary phase particles.

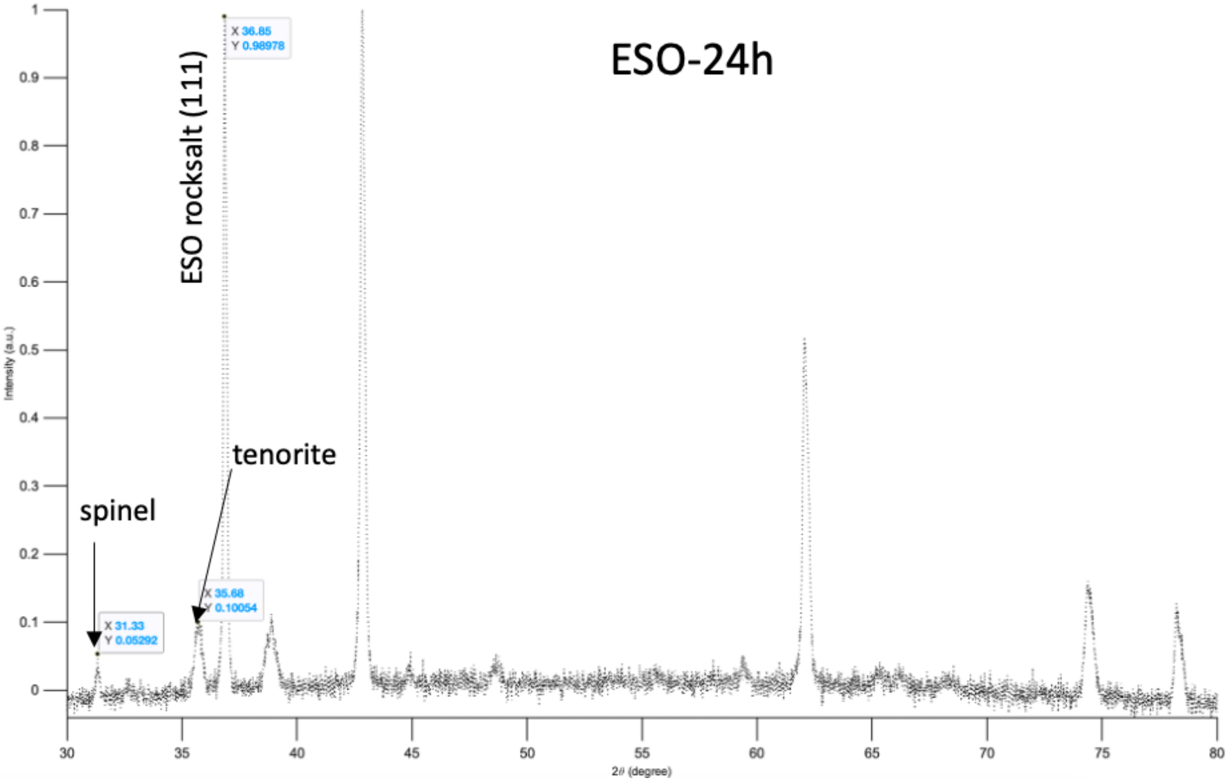

Fig. 4.8. XRD of ESO-24 showing main peaks of spinel, tenorite, and rocksalt phases used to estimate the maximum amount of Cu and Co vacancies created in the rocksalt by secondary phase formation.

Assuming the XRD main peak intensities are proportional to the phase volume,

$$\frac{I_{CuO}}{I_{ESO}} = \frac{0.1005\ (cm^3)}{0.989\ (cm^3)} \times \frac{6.31\ \left(\frac{g}{cm^3}\right)}{6.12\ \left(\frac{g}{cm^3}\right)} \times \frac{\frac{1}{79.5}\,(mol/g)}{\frac{1}{70.12}\,(mol/g)} \times \frac{1\ (mol\ Cu\ in\ CuO\ particles)}{0.2\ (mol\ Cu\ in\ ESO\ matrix)}$$
$$= \frac{92}{200}$$

Therefore, approximately 31.5 % (=92/292) of the Cu atoms initially in the rocksalt ESO leave during heat treatment to form CuO tenorite secondary phases, yielding ~ 6.3 at % of $V_{\mathrm{Cu}}^{//}$ in the rocksalt. Some of these $V_{Cu}^{//}$ help nucleate Co-rich particles based on our hypothesis and previous finding in the literature[207], so are thus likely filled by Co. A similar analysis for Co vacancies estimates ~ 2.3 at % of $V_{Co}^{//}$. This assumes CuO tenorite and Co-rich $ZnCo_2O_4$ which is in line with our atomic-resolution STEM imaging and EDS mapping results of rocksalt matrix and secondary phase particles following heat treatment. The calculated defect values are reasonable considering our EDS maps show that Cu and Co remain in the grain interior.

For the GB conductivity, we observe a single thermally activated conduction mechanism at 25-175 °C with an activation energy of 0.38 eV, attributed to the local electron hopping across the GBs containing Cu-rich tenorite particles. The specific GB conductivity values are ~4 orders of magnitude lower than that of the grain interior, suggesting very poor electron conduction through CuO tenorite particles at the GB. Schematics in Fig. 6 g-i show the correlation between microstructure and electrical conductivity as a function of heat treatment-induced phase transformations in ESO-single, 2h and 24h. The total conductivity values measured for ESO-24h (grain interior plus GBs) increased compared to that measured for ESO-single and ESO-2h, demonstrating enhanced electrical conduction in this ESO caused by heat treatment-induced phase transformations. Additional heat treatment of ESO-24h at 900 °C returns the electronic conductivity and conductivity activation energy to the single-phase value (Fig. 6 f). This highlights the exciting prospect of designing resistive switching devices by balancing enthalpy stabilized secondary phase formation with entropy stabilized second phase annihilation.

4.6 Conclusions

The origin of reversible enhancements in electronic conduction in a single-phase ESO and two multiphase ESOs (heat treated at 700 °C for 2 and 24 h) were detailed with respect to secondary phase content, atomic/nano-scale structure and composition, and defect chemistry. We found that the single-phase ESO has two Cu layers at the surfaces of the ESO crystals forming GBs, stabilizing a single-phase ESO rocksalt solid solution with homogeneous distribution of all elements in the grain interiors. EIS conductivity activation energy measurements suggest that ESO-single is conducting Cu^{+} small polarons by hopping through the rocksalt structure. It is observed that the GBs do not have a specific impact on electronic conduction in this sample. By comparing ESO-single's electronic conductivity to that of the constituent binary oxides, entropy stabilization seems to have little governing effect on electronic transport in this ESO. Upon 2 h of heat treatment, Cu^{2+} leaves the ESO, forming intergranular Cu-rich tenorite particles covering some but not all the GBs. The added $V_{Cu}^{//}$ are compensated by the formation of $V_{O}^{\bullet\bullet}$, facilitating reduction of Cu^{2+} to Cu^{+} in the grains, and enhancing electronic conduction up to ~2 orders of magnitude with a decreased activation energy to 0.55 eV. After 24 h of heat treatment, Cu-rich tenorite phase is assumed to cover all GBs, followed by the nucleation and growth of intragranular Cu-rich tenorite and Co-rich spinel particles in the grain interiors. While Cu-rich tenorite particles at the GBs slow cross-GB electron conduction, Cu^{+} small polaron conduction is shown to further enhance conductivity of grain interiors by 2-3 additional orders of magnitude, due to the extensive formation of $V_{Cu}^{//}$ and $V_{Co}^{//}$ which are charge compensated by $V_{O}^{\bullet\bullet}$. Overall total conductivity in ESO-24h is higher compared to ESO-single and ESO-2h which is attributed to heat treatment-induced phase transformations. The impact of high entropy and entropy stabilization on electronic transport in this material appears to be an indirect one, in that the ESO offers tunable defect chemistry (through heat treatment induced secondary phase formation) which subsequently enhances conductivity. Importantly, the reversibility of the conductivity enhancement points towards the possibility of designing resistive switching materials by balancing entropy stabilized single phases with enthalpy-stabilized composites.

Probing the cation composition profiles across the HIs formed between ESO and secondary phases (in ESO-24h) revealed diffuse interfaces with a relatively large transitional compositional width. On the other hand, atomic structures observed suggest the formation of coherent and semi-coherent HIs with misfit strain. Unlike the equiaxed Co-rich spinel particles, intragranular Cu-rich tenorite particles form in anisotropic needle-like morphologies due to the existence of misfit dislocation at needle tips, allowing faster diffusion and growth in this direction. Our findings suggest the negligible (if any) role of HIs in the conduction mechanisms of the ESO. This work demonstrates the ability to reversibly tune the electrical transport mechanism of ESOs via multiphase design, providing additional degrees of freedom to engineer a wider range of microstructures and compositions which will lead to novel complex concentrated materials.

CHAPTER 5: Outlook and Recommended Future Work

In summary, this work demonstrates the potential for tuning the electrical conductivity of complex oxide materials through altering chemistry and structure of GBs and grain down to the atomic scale.

In the first project, we show that cross-GB oxygen-ion conductivity in a concentrated gadolinium-doped ceria (> 1 mol% dopant) does not solely depend on the concentrations of oxygen vacancies (charge carriers in this oxide) at the space charge layer, unlike previously described for dilute solid solutions. The types and concentrations of other defects (Gd acceptor dopant and local electrons) as well as their interactions with oxygen vacancies play a determining role in cross-GB conductivity by influencing charge carrier concentration and mobility near the GB. Distributions of such defects is dictated by the factors including bulk stoichiometry, structure, and chemo mechanical effects[229] at the GB. While many materials researchers continuously aim to push the boundaries of material design by introducing new structures and/or compositions with enhanced cross-GB ion conductivity. Tuning cross-GB conductivity in gadolinium-doped ceria via alteration of bulk dopant concentration has reached its capacity, as cross-GB conductivity plateaus around ~20 mol% gadolinium dopant.[98] As a result, scientists began incorporating more than 1 dopant (e.g., co-doping with gadolinium and samarium[230]) or triple doping[231] to further increase cross-GB ionic conductivity by the tuning space charge layer defect chemistry. Another impactful area of research aims to connect the relationship between GB structure/character and cross-GB conductivity, which can impact charge transport via influencing factors not limited to defect concentrations (e.g., structure-dependent segregation in GB), migration enthalpies, electrostatic forces and strain fields near charge carrying oxygen vacancies. More research is required to establish an effective connection between GB structure and conductivity.

Another area of GB conductivity research requiring more attention is the discovery and incorporation of oxide sintering and processing strategies that can result in precise engineering of GB composition and structure in bulk and thin films. So far, several methods have shown promises in that they can tune defect concentrations at the GBs, such as cold sintering[18] and radiation-assisted GB segregation[232].

The second project explores the changes in grain and GB electrical conductivity in a (Co,Cu,Mg,Ni,Zn)O entropy stabilized oxide (ESO) via heat treatment-induced phase transformation. As described before, entropy stabilization design strategy introduces a wide range of material systems with unique functionality. This is due to the compositional complexity and chemical disorder, which can influence not only the bulk but also GB properties, such as conductivity.

The composition of GBs down to nm-scale is revealed for the first time in a polycrystalline ESO. It was shown that Cu leaves the rocksalt grains and segregates to the GB, along with an amorphous phase containing Si, Ca, and oxygen. Interestingly, the electronic conductivity results do not reveal a GB specific conductivity based on EIS. It is concluded that the space charge potential at the GBs is insignificant and does not separately contribute to conductivity. More detailed studies with 4D-STEM can help calculate the space charge potential at the GBs of ESOs aiming to connect that to observed or expected electrical conductivity.

Another area of interest is the concept of high entropy grain boundaries (HEGBs) which was introduced in high entropy alloys in 2016[233]. Importance of HEGBs in oxides was recently demonstrated by Lu *et al*[234], suggesting that HEGBs can open a wide range of material structures and properties, owing to the complicated nature of GBs and their ability to sponsor significant type and/or concentrations of point defects, unlike the bulk with the limited concentration of interstitial or substitutional defects due to specific crystal structures.

Another less-described finding of this work, is the relatively large chemical width of heterointerfaces measured using STEM-EELS (compared to structural width, visually demonstrated by HAADF STEM). These heterointerfaces are detected in between rocksalt grain interior and secondary phase particles forming by heat treatment. We conclude that the variations in strain at the heterointerfaces affects secondary phase particle growth rate and therefore, morphology. Heterointerfaces with larger chemical width were previously detected in high entropy alloys and seem to form due to the higher diffusivity of elements in ESO grains compared to binary oxide grains, or in other words, the ability of grains to accommodate GB chemical ordering.

Lastly, we observed an interesting property the (Co,Cu,Mg,Ni,Zn)O ESO studied here. During our electrical conductivity measurements (EIS), ESO is heated to and equilibrated at 25 – 200 °C (50 °C increments), and conductivity is measured at each temperature step. The previous reports claim that phase transformation in this ESO begins at around 600 °C, varying by average grain size. Our EIS data reveals that heat treatment for long periods of time (e.g., > 5 h), leads to phase transformations occurring at much lower temperatures (below 200 °C), suggesting the thermal instability of this ESO compared to initially proposed temperatures of 600 °C and above. As a result, to confidently measure and report the conductivity and activation energy of ESOs (to minimize the risk of phase transformation during measurements), we minimized the time of experiment and the voltage values used in EIS. This is an important discovery, as it brings up yet another interesting question: are ESOs stable enough under practical operation environments? As an example, if ESOs are to be used as active battery materials, will the phase transformation occur as the batteries operate? Is that a beneficial characteristic or will it degrade the battery properties? Answers to such questions are important, as we continue to expand the investment of research on ESOs or similar entropy-stabilized materials. Additionally, we noticed that applying large voltages (> 1 Volt) to the sample, accelerates phase transformation and changes electrical conductivity, proposing the resistive switching potential of this material for ReRAM devices, which has recently been explored in a $(Cr,Mn,Fe,Co,Ni)_3O_4$ spinel that transforms to a rocksalt structure once an electric field is applied[235]

APPENDIX A: Additional Experimental Data on Ionic Conductivity Measurements and Calculated Dopant-Vacancy Interaction Energies in Gadolinium-doped Ceria.

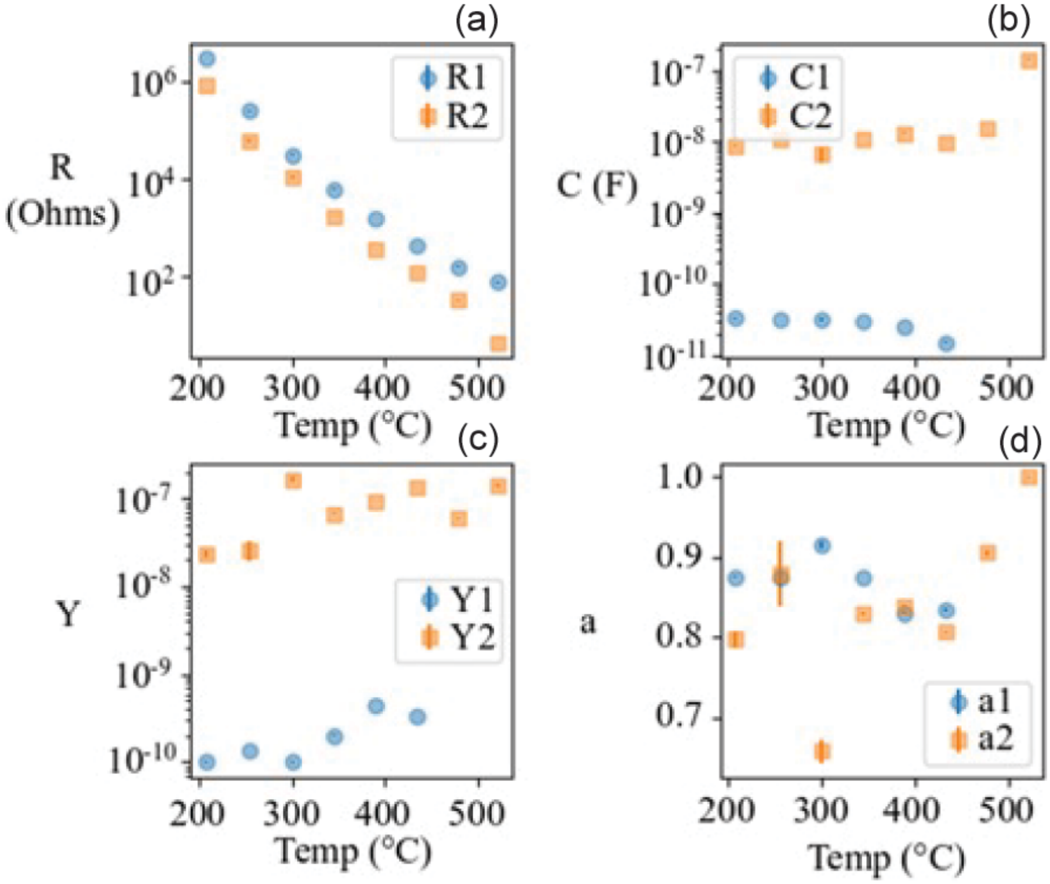

Fig. A.1. R_1 (a), C_1 (b), Y_1 (c), and a_1 (d) correspond to the grain arc in G25CO derived from EIS data fitting. R_2 (a), C_2 (b), Y_2 (c), and a_2 (d) correspond to the GB arc.

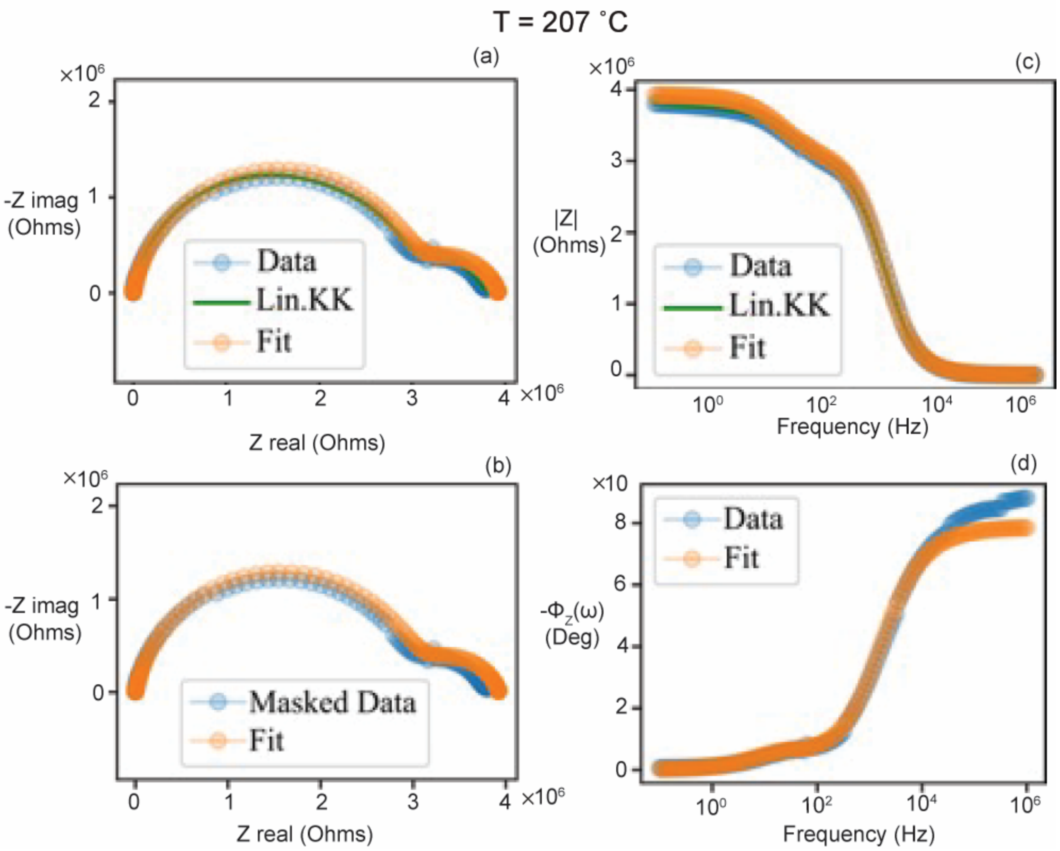

Fig. A.2. G25CO EIS data measured at 207°C. (a) Nyquist plot and (b) Bode plot of measured raw data (“Data”), with fit to linear Kramers-Kronig model (“Lin. KK”), and an equivalent circuit model (“Fit”). (c) The raw data were masked (“Masked data”) prior to equivalent circuit fitting (“Fit”) to avoid fitting the low-frequency electrode contribution. (d) The phase angle plotted against frequency showing the raw data (“Data”) and the fit to the masked data (“Fit”).

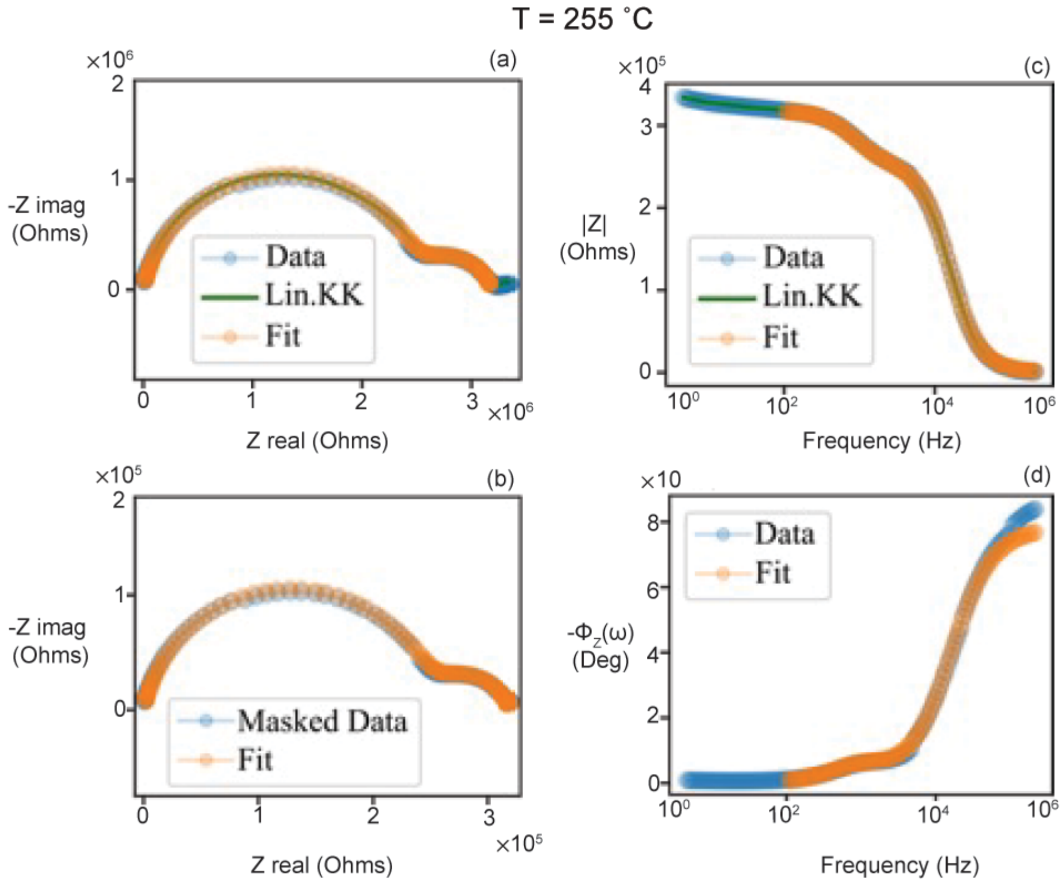

Fig. A.3. G25CO EIS data measured at 255°C. (a) Nyquist plot and (b) Bode plot of measured data (“Data”), with fit to linear Kramers-Kronig model (“Lin. KK”), and an equivalent circuit model (“Fit”). (c) The raw data were masked (“Masked data”) prior to equivalent circuit fitting (“Fit”) to avoid fitting the low-frequency electrode contribution. (d) The phase angle plotted against frequency showing the raw data (“Data”) and the fit to the masked data (“Fit”).

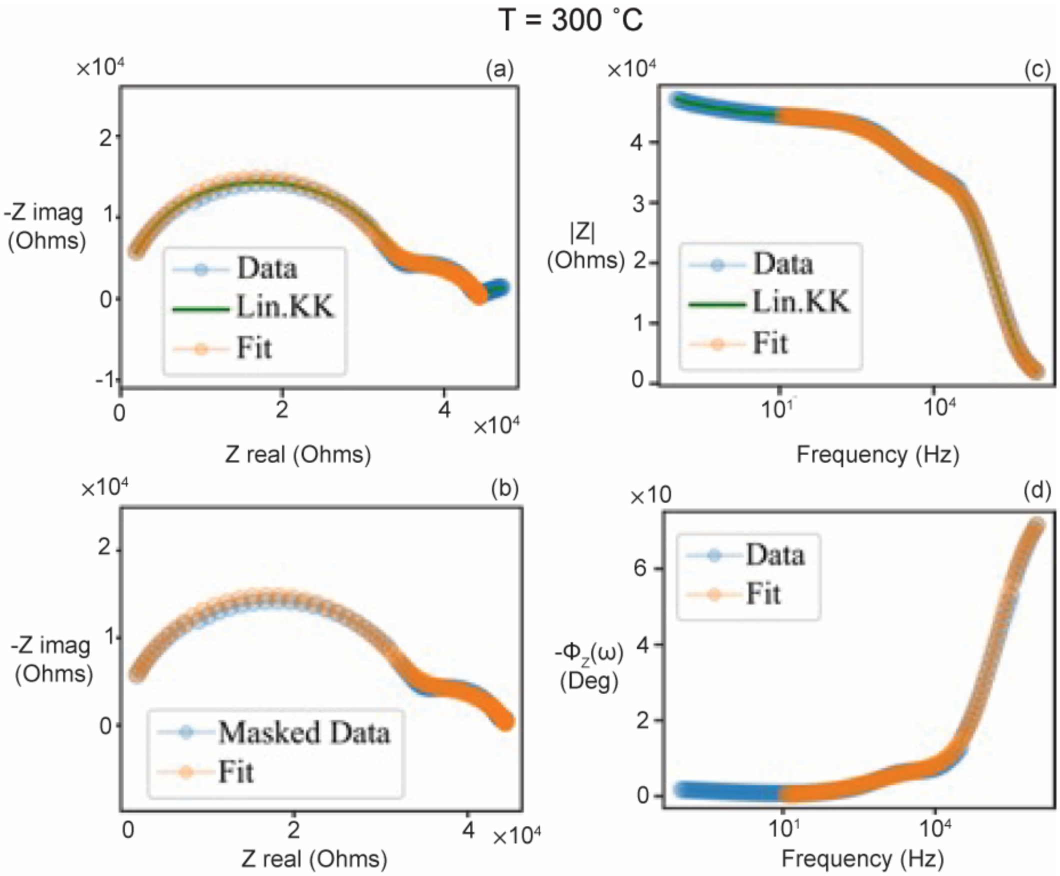

Fig. A.4. G25CO EIS data measured at 300°C. (a) Nyquist plot and (b) Bode plot of measured data ("Data"), with fit to linear Kramers-Kronig model ("Lin. KK"), and an equivalent circuit model ("Fit"). (c) The raw data were masked ("Masked data") prior to equivalent circuit fitting ("Fit") to avoid fitting the low-frequency electrode contribution. (d) The phase angle plotted against frequency showing the raw data ("Data") and the fit to the masked data ("Fit").

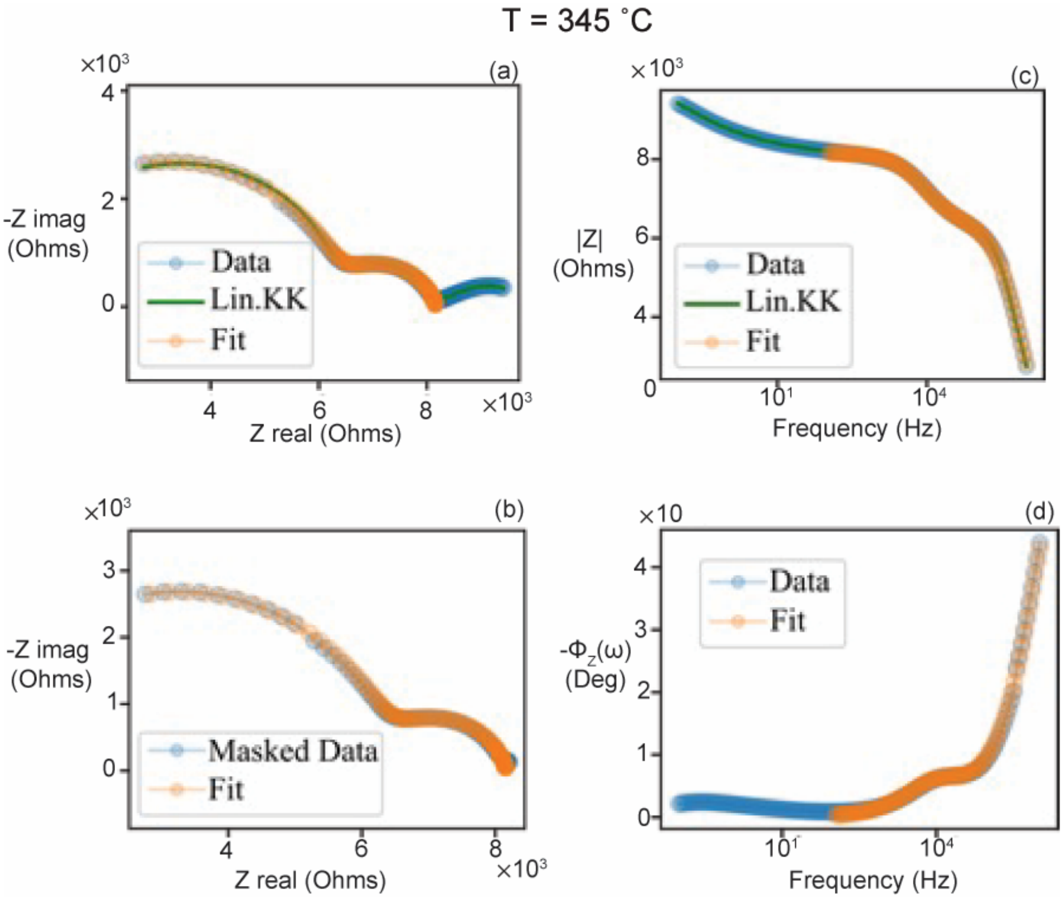

Fig. A.5. G25CO EIS data measured at 345°C. (a) Nyquist plot and (b) Bode plot of measured data ("Data"), with fit to linear Kramers-Kronig model ("Lin. KK"), and an equivalent circuit model ("Fit"). (c) The raw data were masked ("Masked data") prior to equivalent circuit fitting ("Fit") to avoid fitting the low-frequency electrode contribution. (d) The phase angle plotted against frequency showing the raw data ("Data") and the fit to the masked data ("Fit").

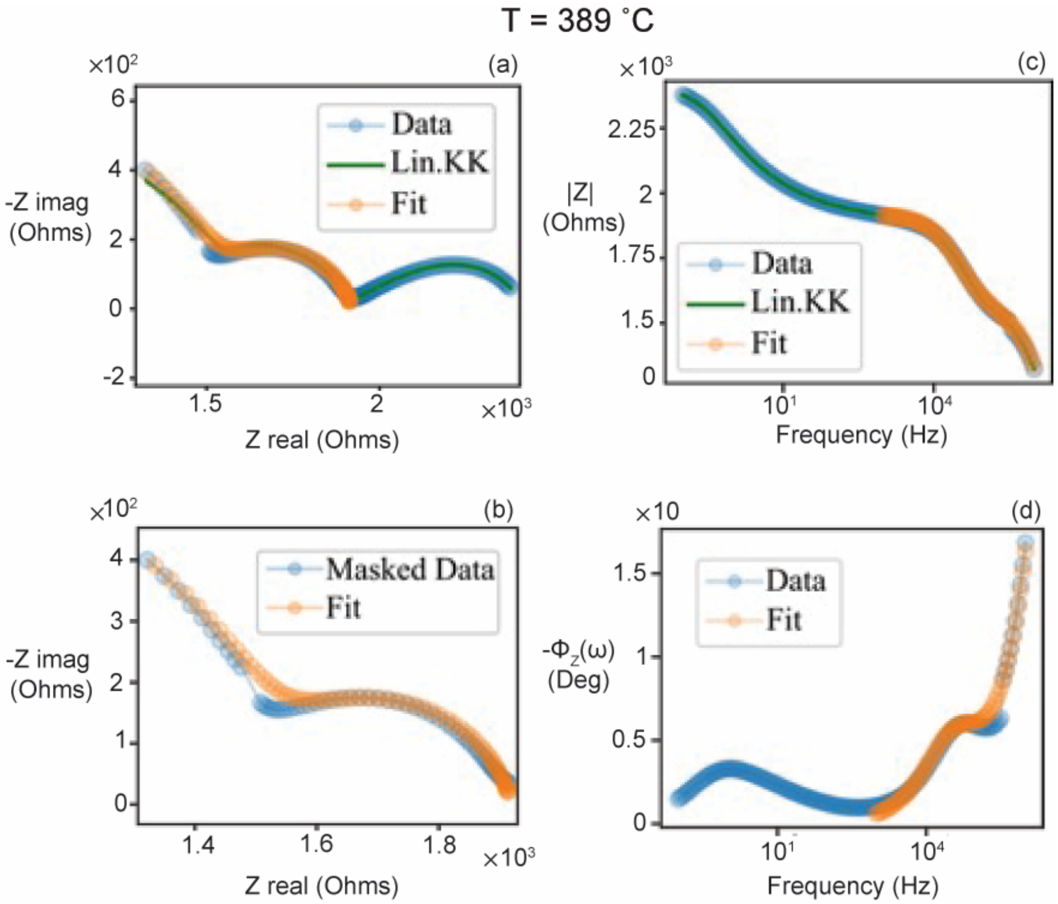

Fig. A.6. G25CO EIS data measured at 389°C. (a) Nyquist plot and (b) Bode plot of measured data ("Data"), with fit to linear Kramers-Kronig model ("Lin. KK"), and an equivalent circuit model ("Fit"). (c) The raw data were masked ("Masked data") prior to equivalent circuit fitting ("Fit") to avoid fitting the low-frequency electrode contribution. (d) The phase angle plotted against frequency showing the raw data ("Data") and the fit to the masked data ("Fit").

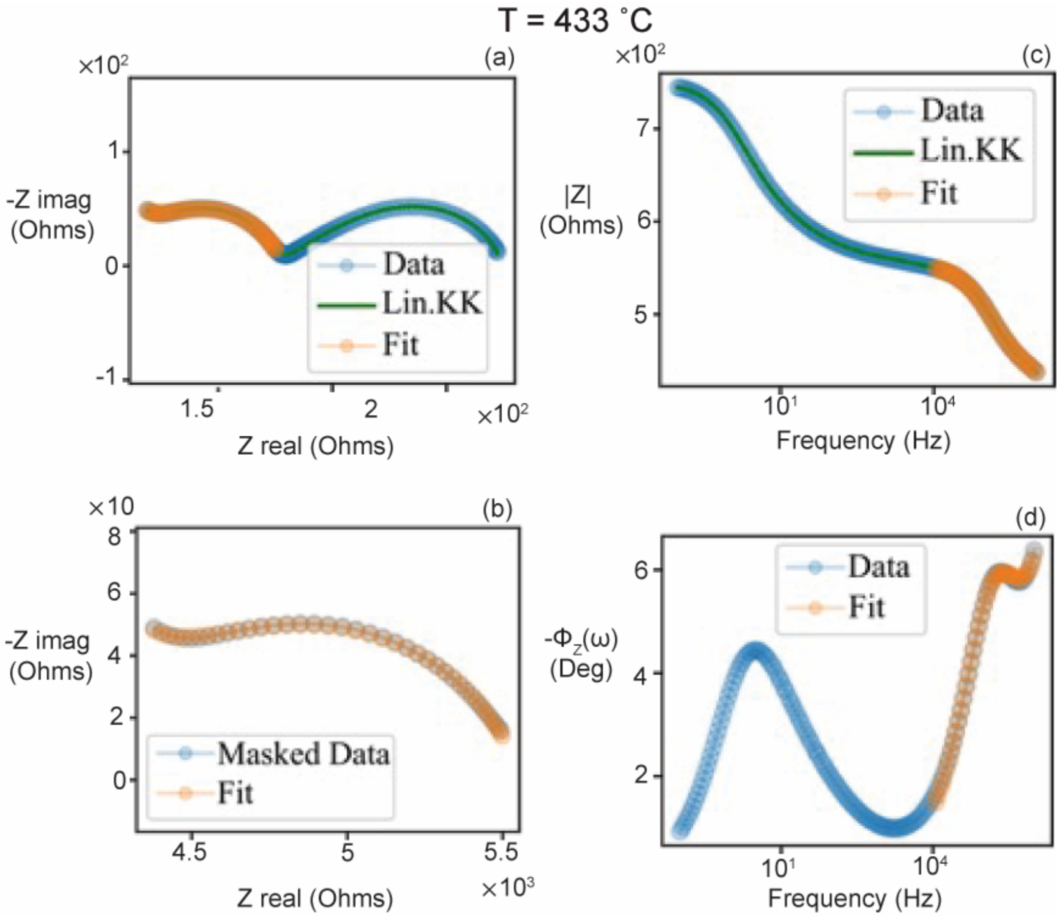

Fig. A.7. G25CO EIS data measured at 433°C. (a) Nyquist plot and (b) Bode plot of measured data ("Data"), with fit to linear Kramers-Kronig model ("Lin. KK"), and an equivalent circuit model ("Fit"). (c) The raw data were masked ("Masked data") prior to equivalent circuit fitting ("Fit") to avoid fitting the low-frequency electrode contribution. (d) The phase angle plotted against frequency showing the raw data ("Data") and the fit to the masked data ("Fit").

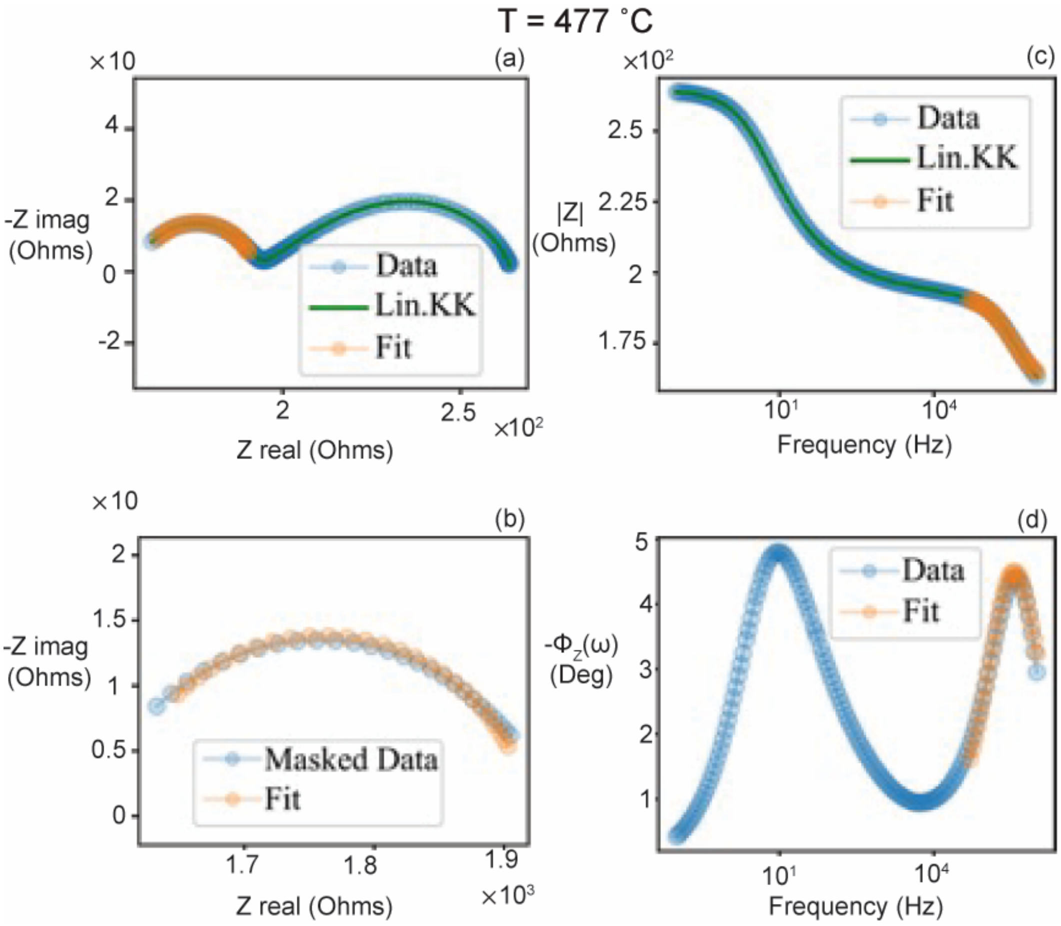

Fig. A.8. G25CO EIS data measured at 477°C. (a) Nyquist plot and (b) Bode plot of measured data ("Data"), with fit to linear Kramers-Kronig model ("Lin. KK"), and an equivalent circuit model ("Fit"). (c) The raw data were masked ("Masked data") prior to equivalent circuit fitting ("Fit") to avoid fitting the low-frequency electrode contribution. (d) The phase angle plotted against frequency showing the raw data ("Data") and the fit to the masked data ("Fit").

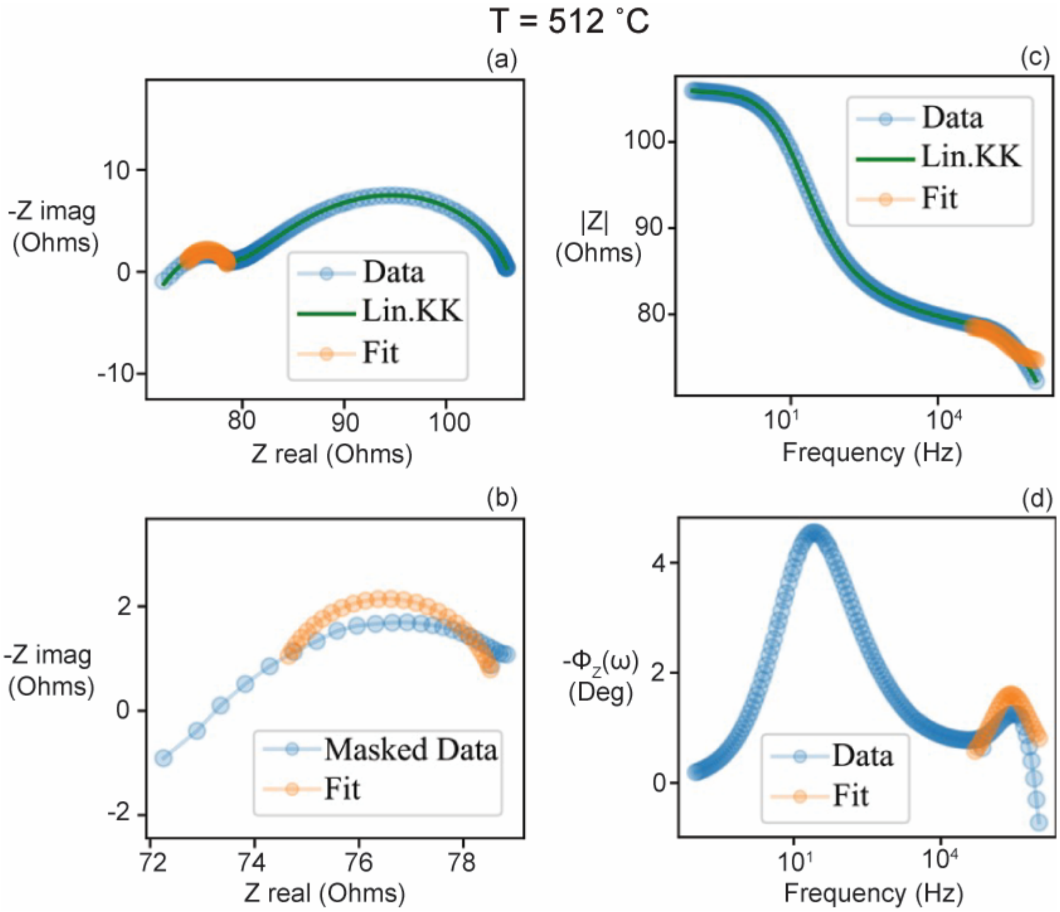

Fig. A.9. G25CO EIS data measured at 521°C. (a) Nyquist plot and (b) Bode plot of measured data (“Data”), with fit to linear Kramers-Kronig model (“Lin. KK”), and an equivalent circuit model (“Fit”). (c) The raw data were masked (“Masked data”) prior to equivalent circuit fitting (“Fit”) to avoid fitting the low-frequency electrode contribution. (d) The phase angle plotted against frequency showing the raw data (“Data”) and the fit to the masked data (“Fit”).

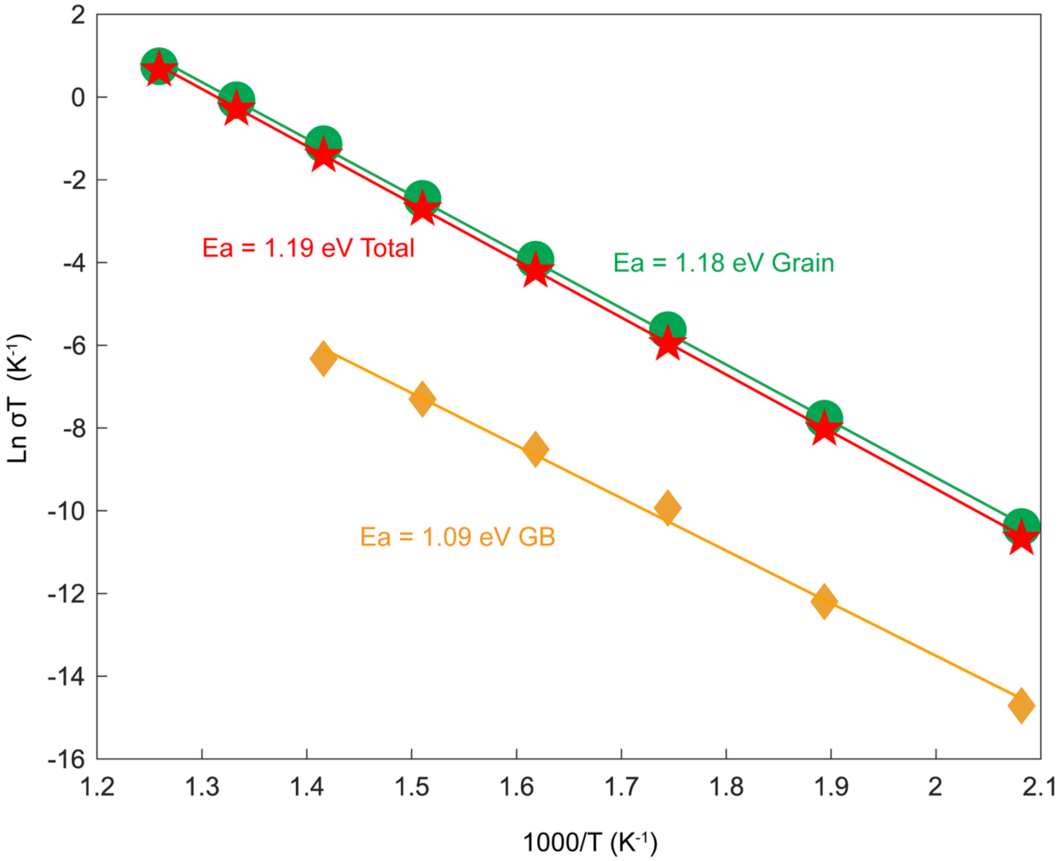

Fig. A.10. Arrhenius plot of bulk (grain), grain boundary and total conductivity used to calculate the activation energies of conductivity in G25CO.

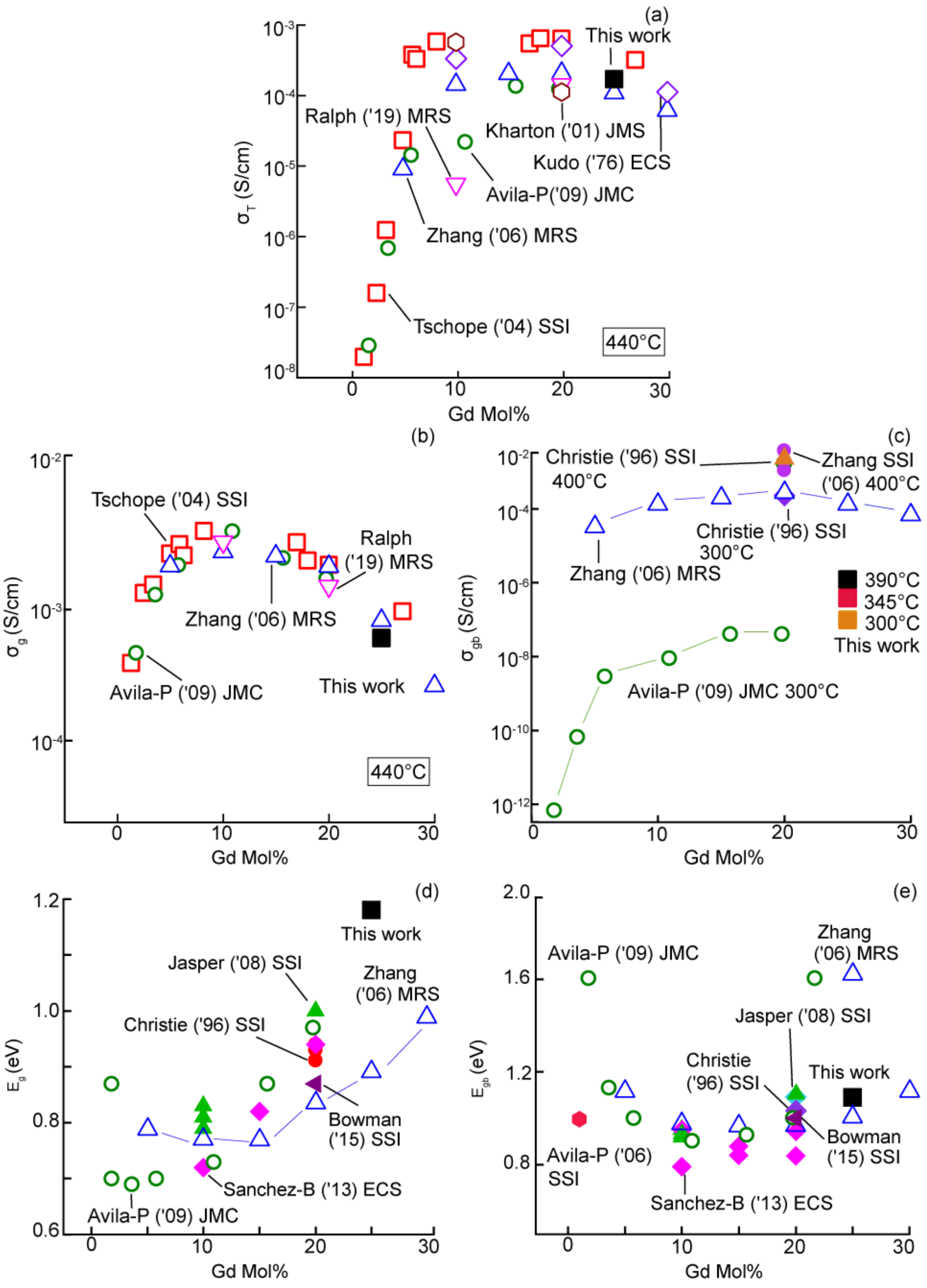

Fig. A.11. Conductivity and conductivity activation energy comparison with literature data at various temperatures. (a) total conductivity at 440°C (b) grain conductivity at 440°C, (c) specific GB conductivity at 300 - 400°C, (d) grain conductivity activation energy, (e) specific GB conductivity activation energy[64,95,98,124,140–147].

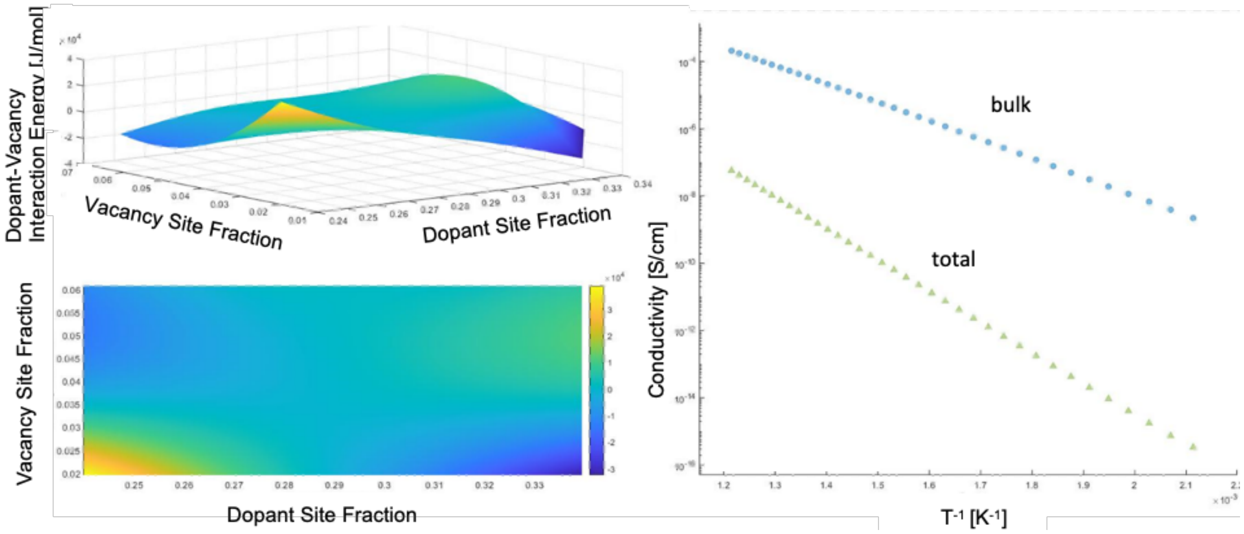

Fig. A.12. (a) 3D map of defect interactions as a function of vacancy site fraction and dopant site fraction in GB1. (b) Total and bulk conductivity (S cm^{-1}) calculated using the model as a function of inverse temperature (K^{-1}).

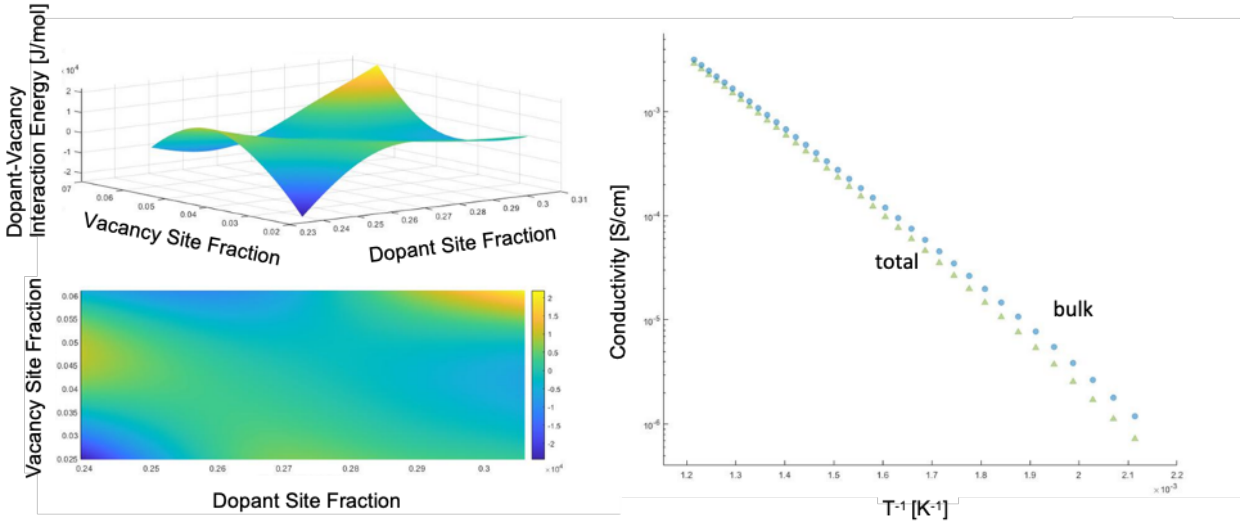

Fig. A.13. (a) 3D map of defect interactions as a function of vacancy site fraction and dopant site fraction in GB2. (b) Total and bulk conductivity (S cm^{-1}) calculated using the model as a function of inverse temperature (K^{-1}).

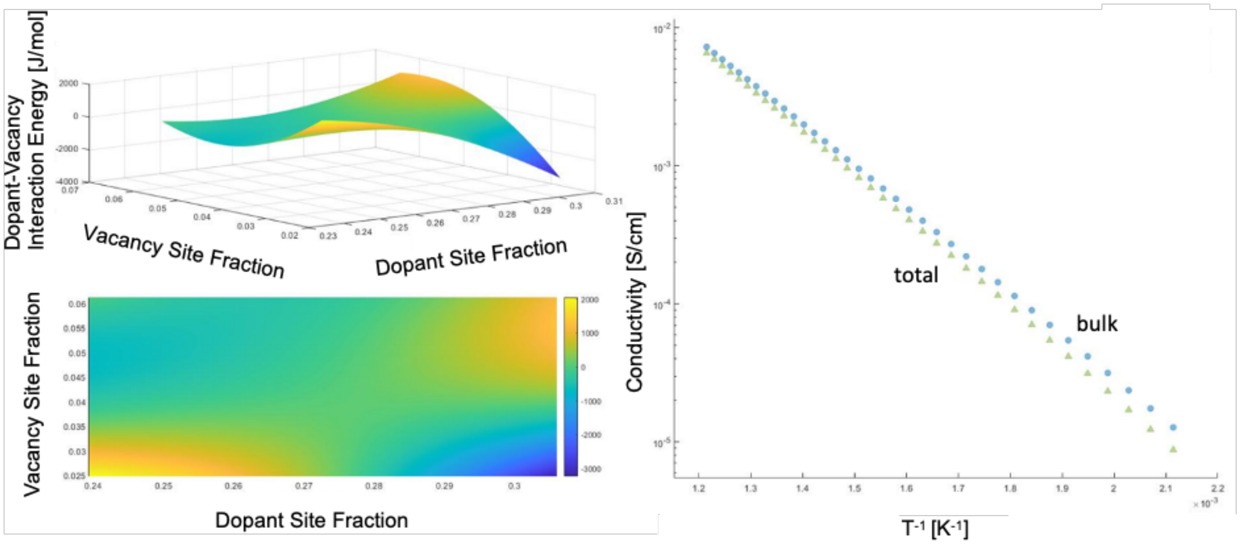

Fig. A.14. (a) 3D map of defect interactions as a function of vacancy site fraction and dopant site fraction in GB3. (b) Total and bulk conductivity (S cm^{-1}) calculated using the model as a function of inverse temperature (K^{-1}).

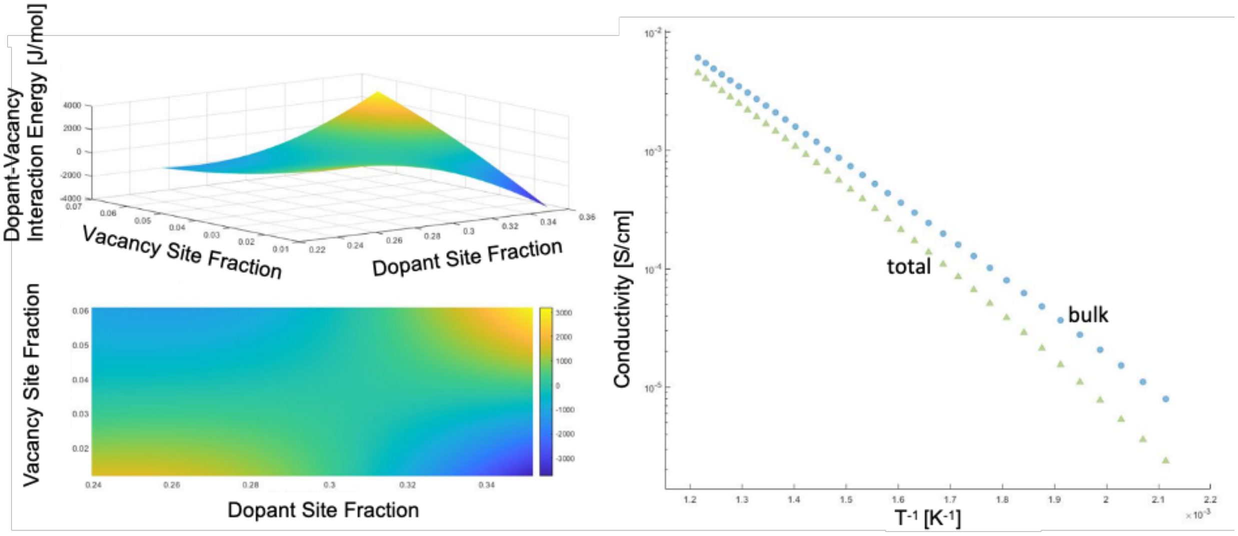

Fig. A.15. (a) 3D map of defect interactions as a function of vacancy site fraction and dopant site fraction in GB4. (b) Total and bulk conductivity (S cm^{-1}) calculated using the model as a function of inverse temperature (K^{-1}).

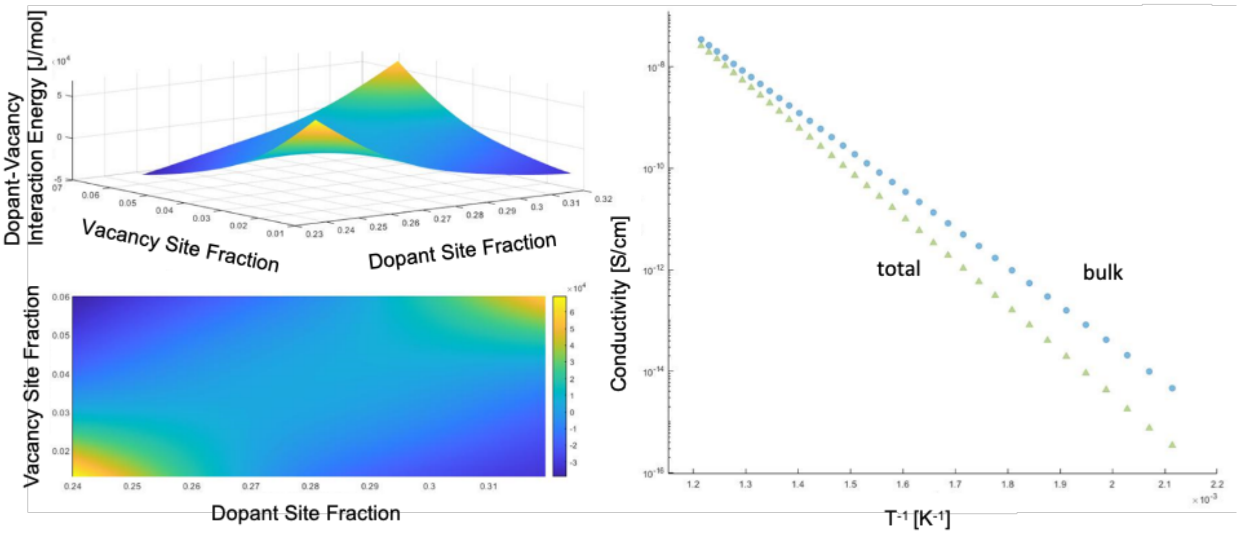

Fig. A.16. (a) 3D map of defect interactions as a function of vacancy site fraction and dopant site fraction in GB5. (b) Total and bulk conductivity (S cm^{-1}) calculated using the model as a function of inverse temperature (K^{-1}).

APPENDIX B: Additional Experimental Data on Structure and Composition of Grain and Grain Boundaries in Single phase (Co,Cu,Ni,Zn,Mg)O Entropy Stabilized Oxides

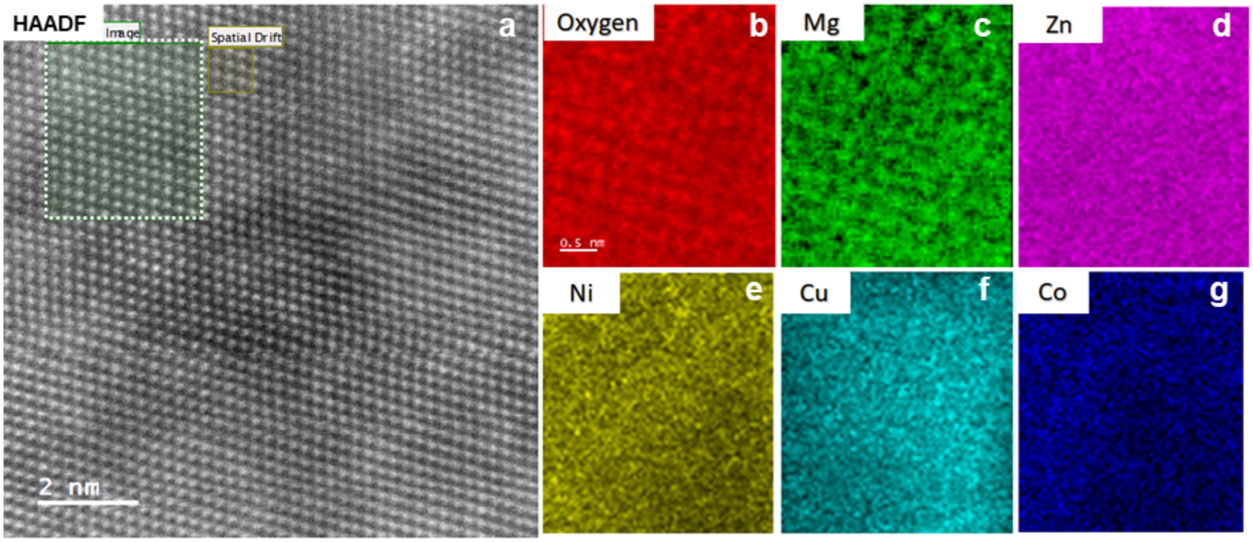

Fig. B.1. Atomic-resolution STEM EDS intensity map of ESO rocksalt. (a) HAADF STEM micrograph. (b-g) correspond to O, Mg, Zn, Ni, Cu and Co, respectively.

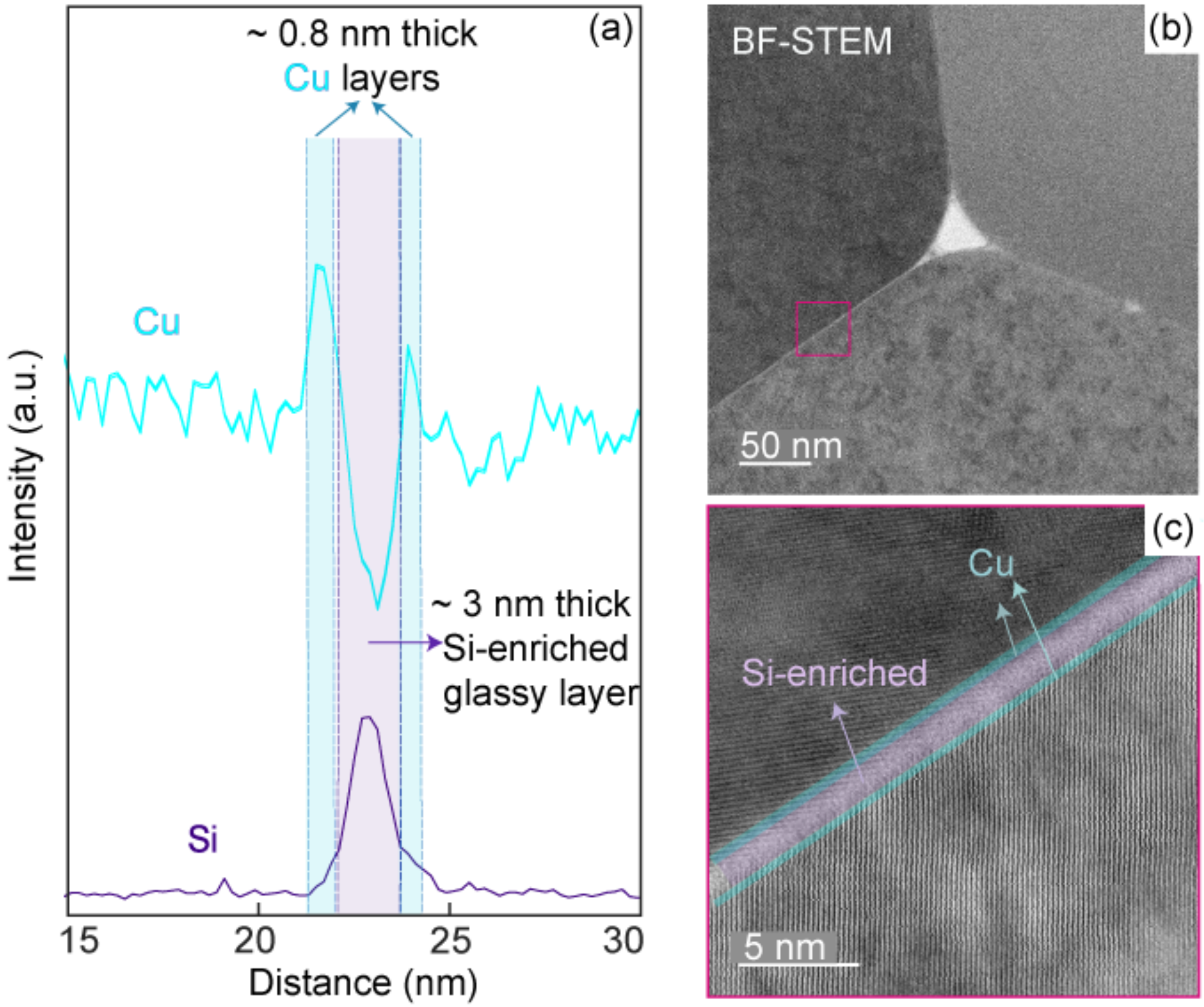

Fig. B. 2. Segregation of Cu layers at the edge of Si-enriched glassy phase at the GB. (a) Cu and Si intensity line profiles across the GB show in (b, c). Purple and blue highlighted areas correspond to the locations of the Si-enriched and Cu layers segregation at this GB. (b) STEM-BF image of a triple junction in ESO-single specimen. (c) zoomed-in view of this GB, with highlighted areas referring to Si-enriched and Cu layers.

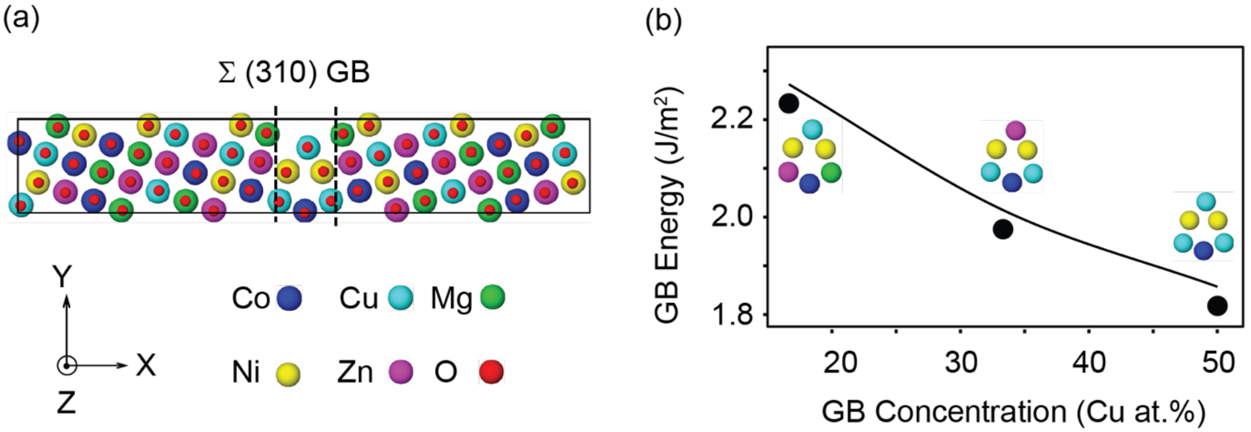

Fig. B.3. a) Simulated atomic structure of a Σ5 (310) GB with 50 at. % Cu using DFT. b) Calculated GB energy as a function of Cu-ion concentration at the Σ5 (310) GBs.

Table B.1. Stoichiometry of cations (mole %) in Cu-rich tenorite side/tip and Co-rich spinel secondary phases measured using STEM-EELS

Cation	Cu-rich needle tip (mole %)	Cu-rich needle side (mole %)	Co-rich (mole %)
Cu	73	53	0.6
Co	—	—	81.6
Ni			1.8
Zn	19	27	12.6
Mg	8	2	—

APPENDIX C: Additional Experimental on Measuring Electrical Conductivity of Single Phase and Multiphase Entropy Stabilized Oxides

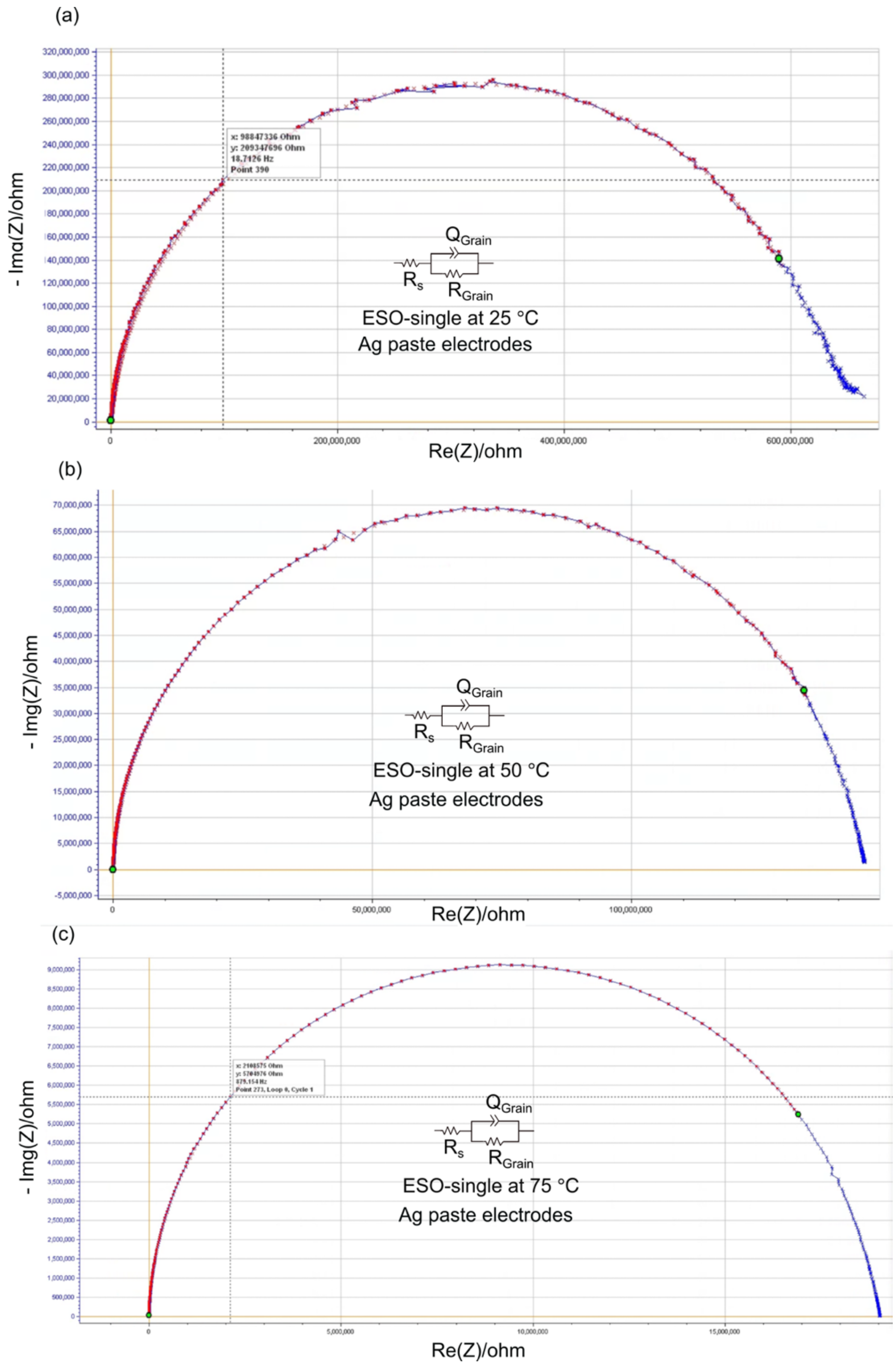

Fig. C.1. Nyquist plots collected from ESO-single with Ag paste electrodes from (a-c) 25-75 °C.

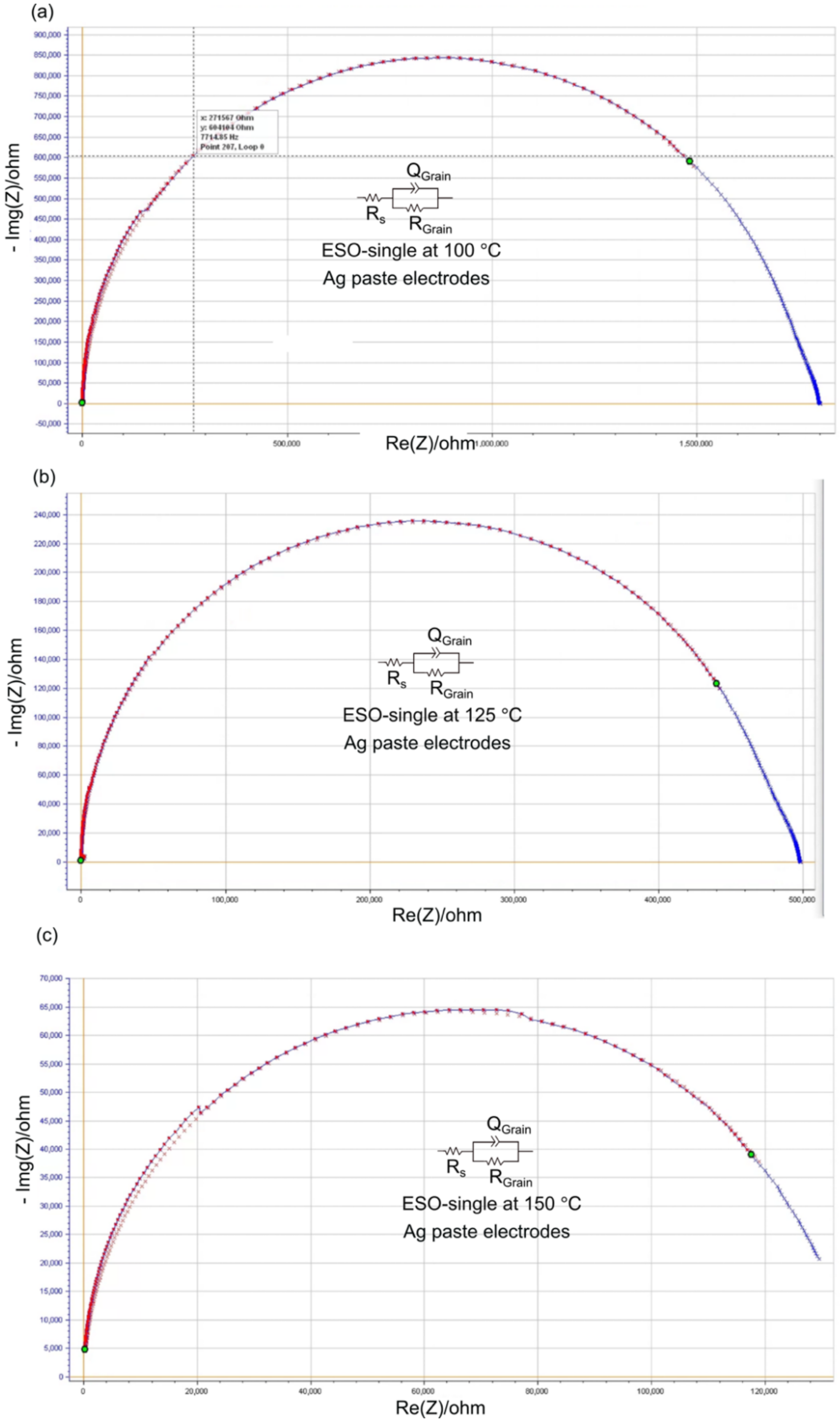

Fig. C.2. Nyquist plots from ESO-single with Ag paste electrodes from (a-c) 100-150 °C.

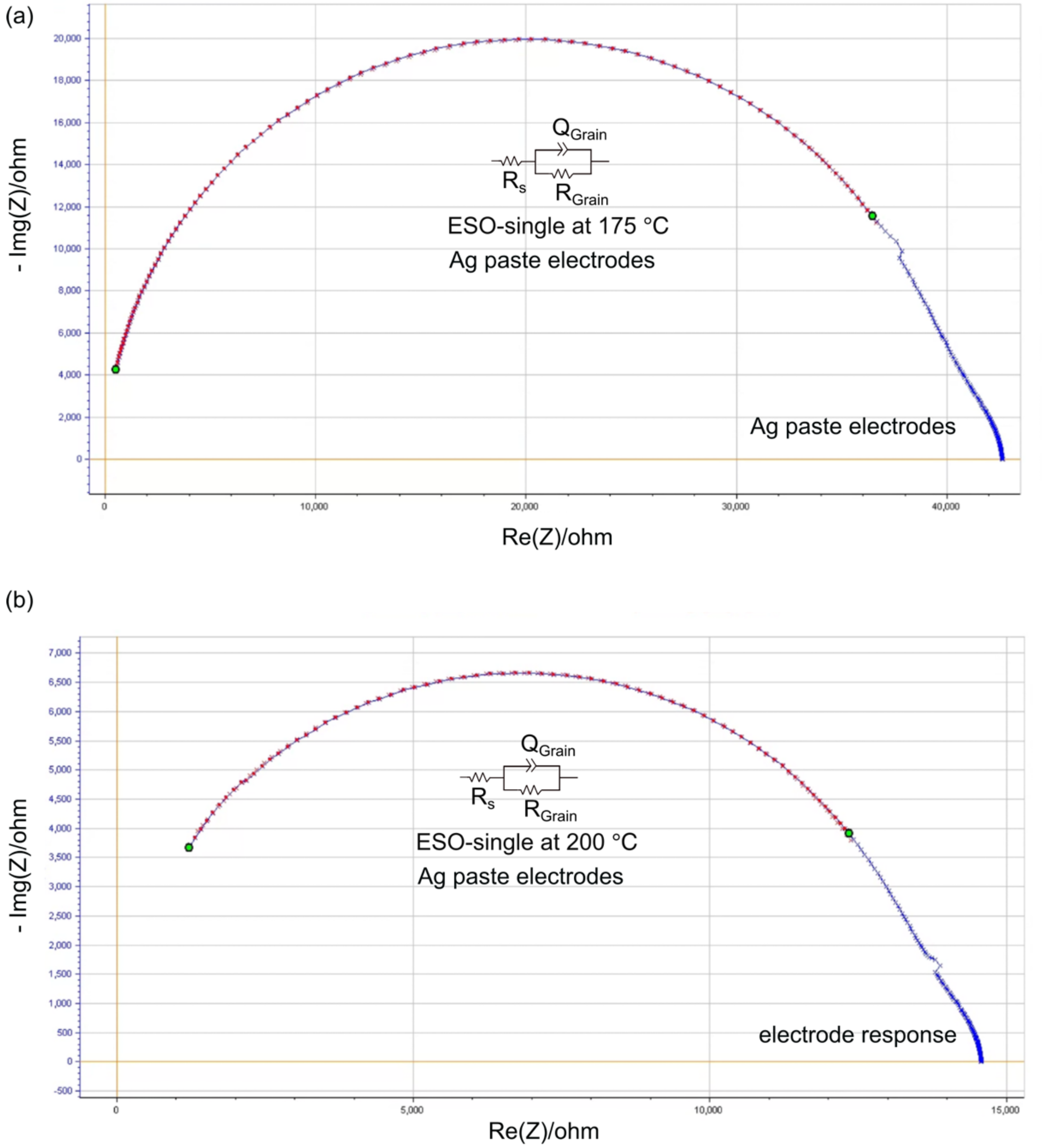

Fig. C.3. Nyquist plots collected from ESO-single with Ag paste electrodes from (a-b) 175-200 °C.

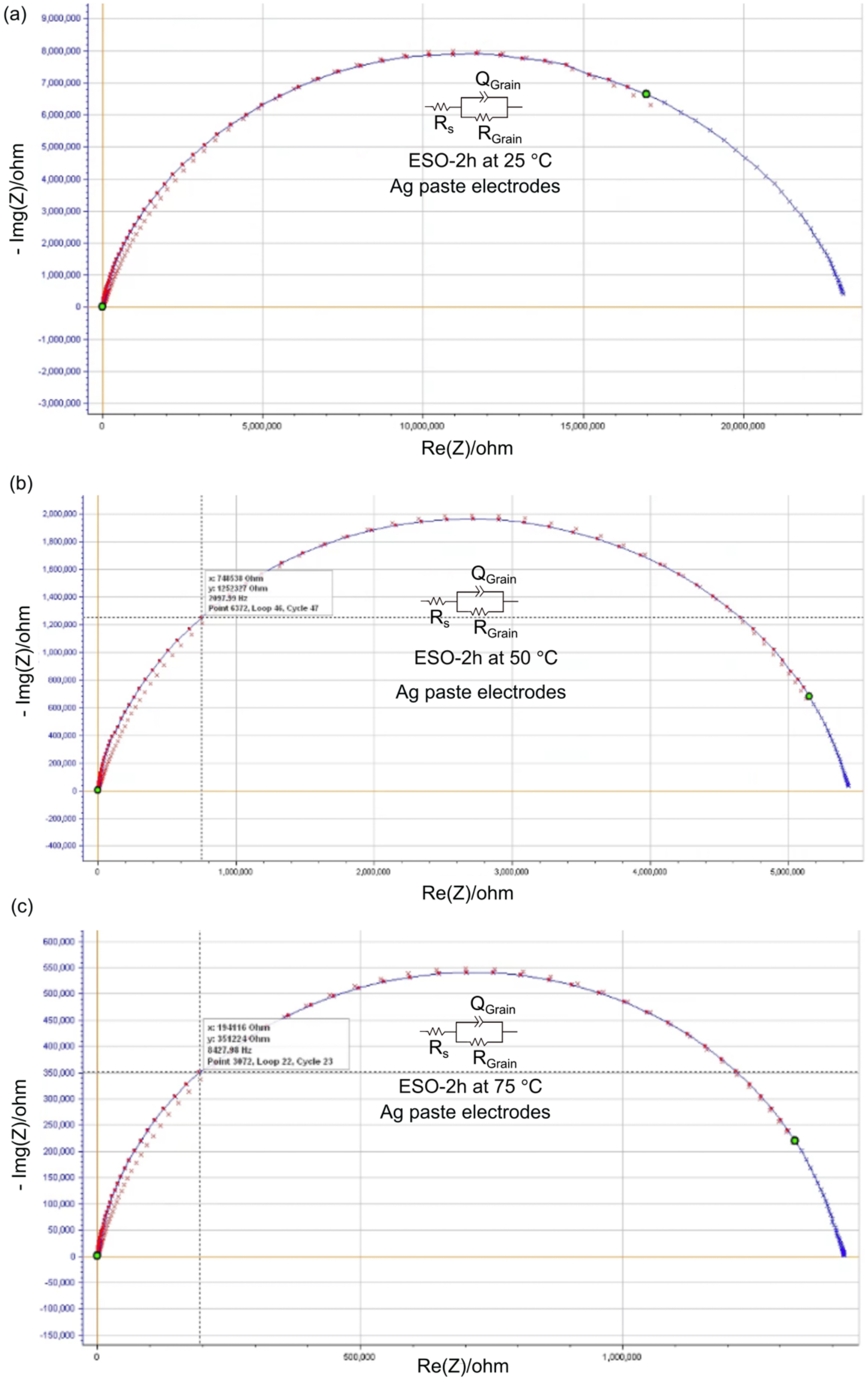

Fig. C.4. Nyquist plots collected from ESO-2h with Ag paste electrodes from (a-c) 25-75 °C.

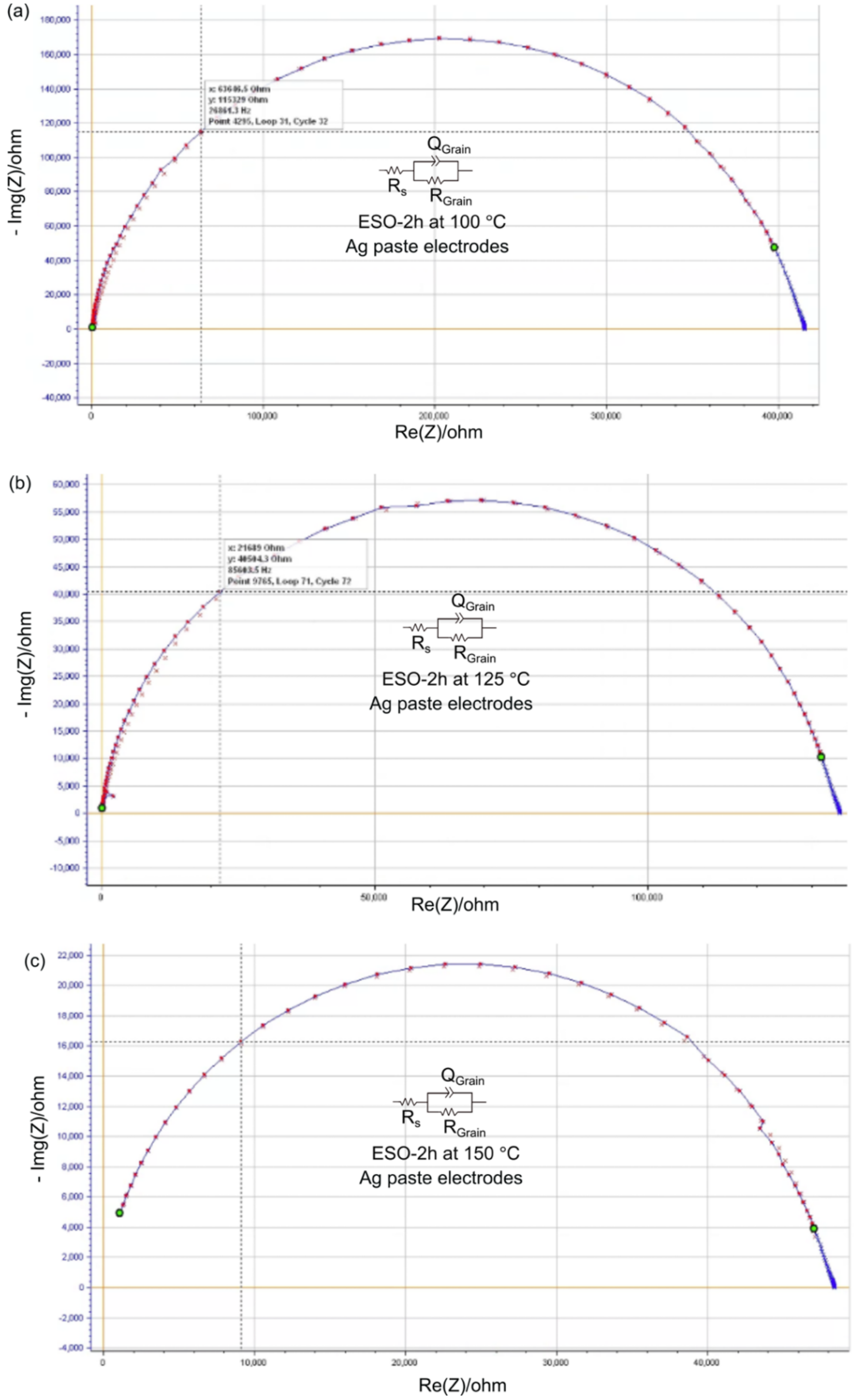

Fig. C.5. Nyquist plots collected from ESO-2h with Ag paste electrodes from (a-c) 100-150 °C.

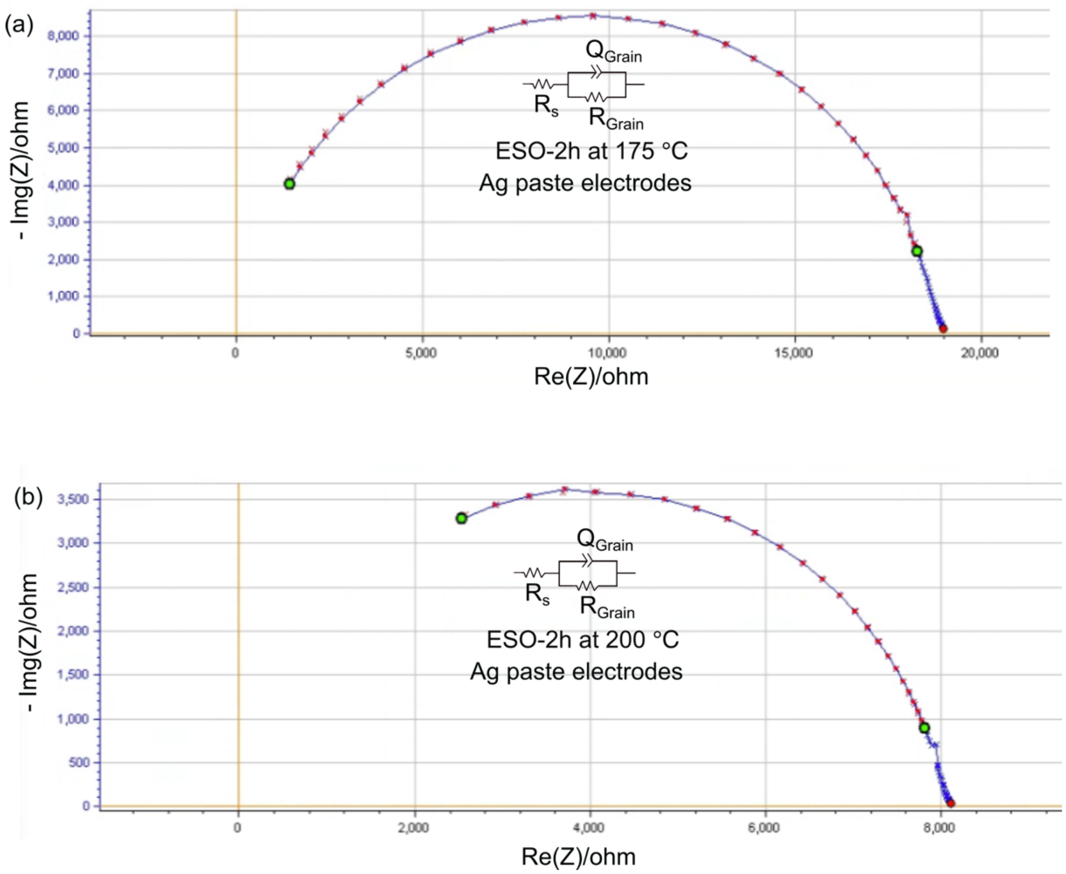

Fig. C.6. Nyquist plots collected from ESO-2h with Ag paste electrodes from (a-c) 175-200 °C.

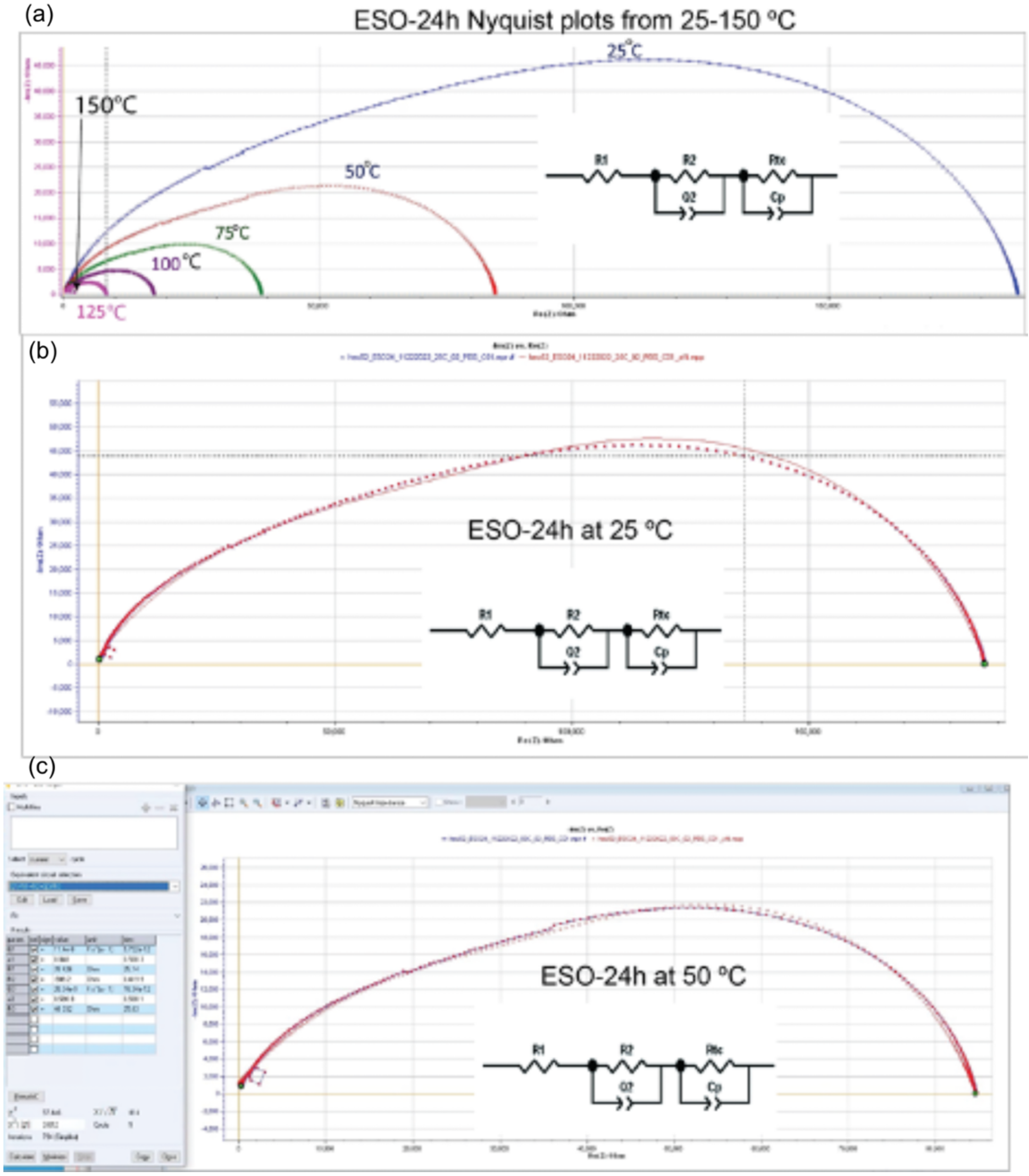

Fig. C.7. Nyquist plots collected from ESO-24h with Ag paste electrodes from (a-c) 25-50 °C.

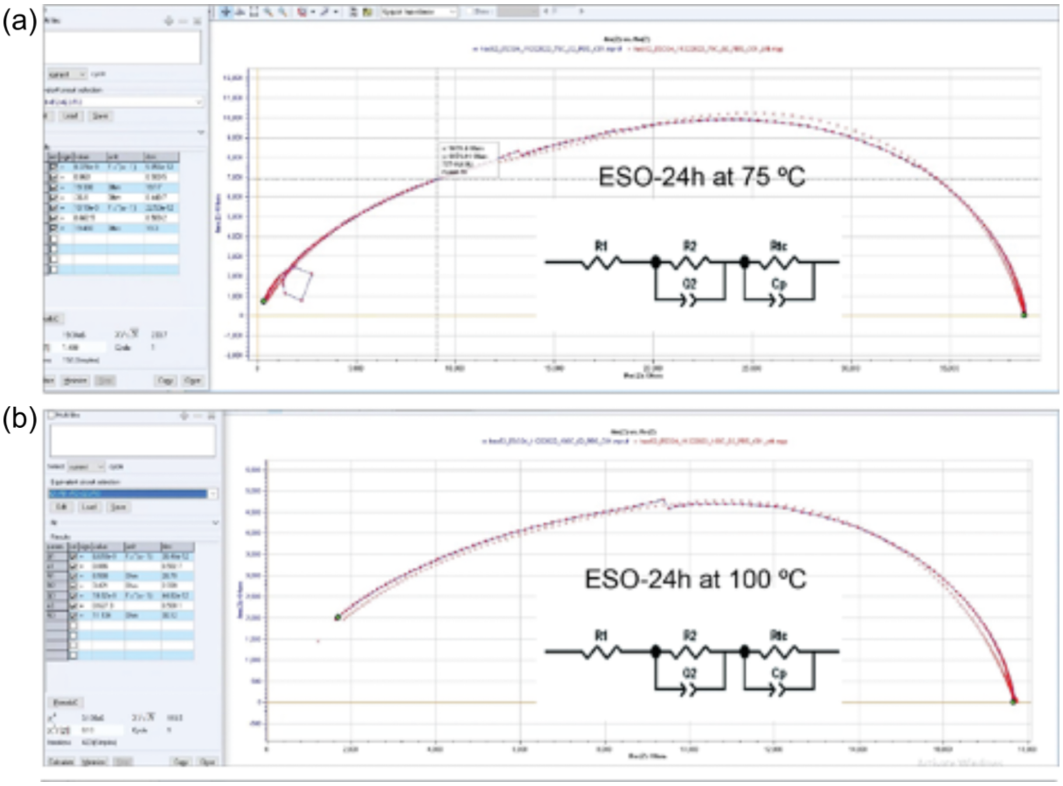

Fig. C.8. Nyquist plots collected from ESO-24h with Ag paste electrodes from (a-b) 75-100 °C.

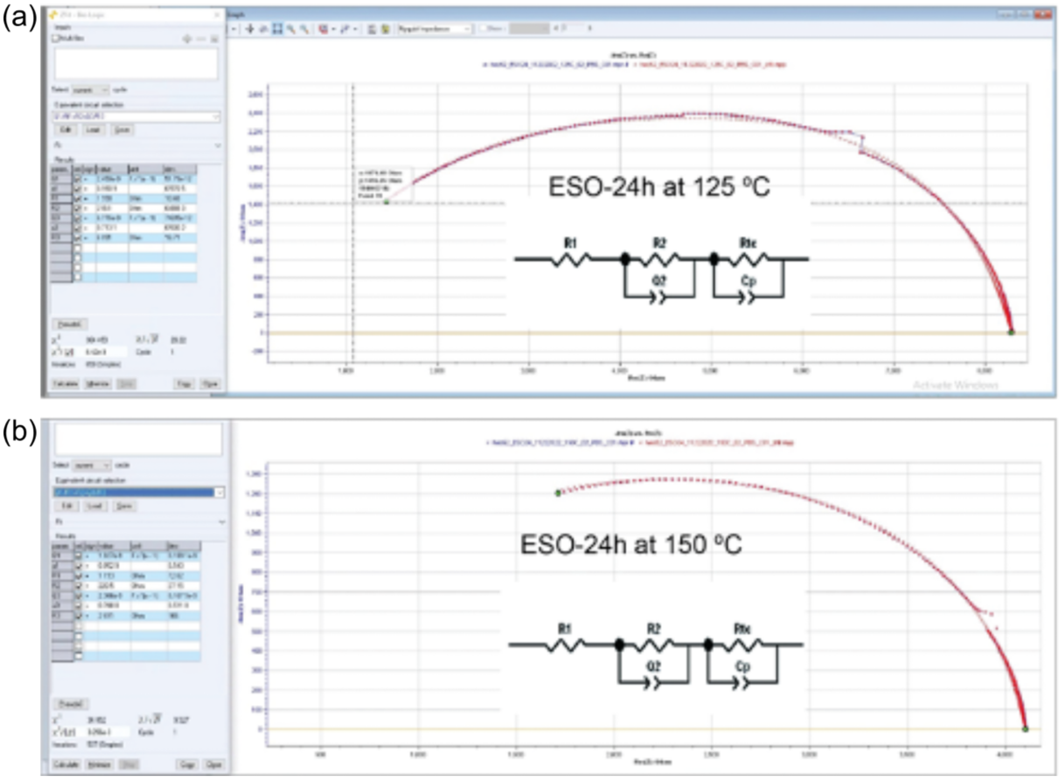

Fig. C.9. Nyquist plots collected from ESO-24h with Ag paste electrodes from (a-b) 125-150 °C.

Table C.1. Calculating capacity values for grain in ESO-single, 2h and 24h and for grain boundary in ESO-24h.

Sample	**Capacity [F]**
ESO-Single	(29-34) e^{-12}
ESO-2h	(37-80) e^{-12}
ESO-24h grain	(0.1-0.24) e^{-9}
ESO-24h GB	(1.3-5.7) e^{-9}

References

1. Ma, C. *et al.* Atomic-scale origin of the large grain-boundary resistance in perovskite Li-ion-conducting solid electrolytes. *Energy Environ. Sci.* **7**, 1638–1642 (2014).

2. Wynblatt, P. & Chatain, D. Anisotropy of segregation at grain boundaries and surfaces. *Metall Mater Trans A* **37**, 2595–2620 (2006).

3. Tuller, H. L. & Bishop, S. R. Point Defects in Oxides: Tailoring Materials Through Defect Engineering. *Annual Review of Materials Research* **41**, 369–398 (2011).

4. Bowman, W. J., Zhu, J., Sharma, R. & Crozier, P. A. Electrical conductivity and grain boundary composition of Gd-doped and Gd/Pr co-doped ceria. *Solid State Ionics* **272**, 9–17 (2015).

5. Pryds, N. & Esposito, V. When two become one: An insight into 2D conductive oxide interfaces. *J Electroceram* **38**, 1–23 (2017).

6. Syed, K. *et al.* Correlations of grain boundary segregation to sintering techniques in a three-phase ceramic. *Materialia* **14**, 100890 (2020).

7. Haile, S. M., West, D. L. & Campbell, J. The role of microstructure and processing on the proton conducting properties of gadolinium-doped barium cerate. *Journal of Materials Research* **13**, 1576–1595 (1998).

8. Epp, J. 4 - X-ray diffraction (XRD) techniques for materials characterization. in *Materials Characterization Using Nondestructive Evaluation (NDE) Methods* (eds. Hübschen, G.,

Altpeter, I., Tschuncky, R. & Herrmann, H.-G.) 81–124 (Woodhead Publishing, 2016). doi:10.1016/B978-0-08-100040-3.00004-3.

9. Rosenberg, N. The Role of Electricity in Industrial Development. *The Energy Journal* **19**, 7–24 (1998).
10. Ritchie, H., Rosado, P. & Roser, M. Fossil fuels. *Our World in Data* (2024).
11. World – World Energy Balances: Overview – Analysis. *IEA* https://www.iea.org/reports/world-energy-balances-overview/world.
12. Nevitt, M. Assessing COP28: The New Global Climate Deal in Dubai. SSRN Scholarly Paper at https://papers.ssrn.com/abstract=4667941 (2023).
13. Campanari, S., Mastropasqua, L., Gazzani, M., Chiesa, P. & Romano, M. C. Predicting the ultimate potential of natural gas SOFC power cycles with CO2 capture – Part A: Methodology and reference cases. *Journal of Power Sources* **324**, 598–614 (2016).
14. High-temperature Solid Oxide Fuel Cells: Fundamentals, Design and Applications - 1st Edition. https://shop.elsevier.com/books/high-temperature-solid-oxide-fuel-cells-fundamentals-design-and-applications/singhal/978-1-85617-387-2.
15. Avila-Paredes, H. J. & Kim, S. The effect of segregated transition metal ions on the grain boundary resistivity of gadolinium doped ceria: Alteration of the space charge potential. *Solid State Ionics* **177**, 3075–3080 (2006).

16. Guo, X., Sigle, W. & Maier, J. Blocking Grain Boundaries in Yttria-Doped and Undoped Ceria Ceramics of High Purity. *Journal of the American Ceramic Society* **86**, 77–87 (2003).

17. Biesuz, M., Grasso, S. & Sglavo, V. M. What's new in ceramics sintering? A short report on the latest trends and future prospects. *Current Opinion in Solid State and Materials Science* **24**, 100868 (2020).

18. Kindelmann, M. *et al.* Highly conductive grain boundaries in cold-sintered barium zirconate-based proton conductors. *J. Mater. Chem. A* (2023) doi:10.1039/D3TA07076J.

19. Browning, N. D., Klie, R. F. & Lei, Y. Vacancy Segregation at Grain Boundaries in Ceramic Oxides. in *Mixed Ionic Electronic Conducting Perovskites for Advanced Energy Systems* (eds. Orlovskaya, N. & Browning, N.) 15–25 (Springer Netherlands, Dordrecht, 2004). doi:10.1007/978-1-4020-2349-1_2.

20. Kim, S. & Maier, J. On the conductivity mechanism of nanocrystalline ceria. *Journal of the Electrochemical Society* **149**, J73–J83 (2002).

21. Guo, X. & Waser, R. Space charge concept for acceptor-doped zirconia and ceria and experimental evidences. *Solid State Ionics* **173**, 63–67 (2004).

22. Mebane, D. S. & Souza, R. A. D. A generalised space-charge theory for extended defects in oxygen-ion conducting electrolytes: from dilute to concentrated solid solutions. *Energy Environ. Sci.* **8**, 2935–2940 (2015).

23. Kröger, F. A. & Vink, H. J. Relations between the Concentrations of Imperfections in Crystalline Solids. in *Solid State Physics* (eds. Seitz, F. & Turnbull, D.) vol. 3 307–435 (Academic Press, 1956).

24. Maier, J. Ionic conduction in space charge regions. *Progress in Solid State Chemistry* **23**, 171–263 (1995).

25. Kim, S., Fleig, J. & Maier, J. Space charge conduction: Simple analytical solutions for ionic and mixed conductors and application to nanocrystalline ceria. *Phys. Chem. Chem. Phys.* **5**, 2268–2273 (2003).

26. Tong, X., Mebane, D. S. & Souza, R. A. D. Analyzing the grain-boundary resistance of oxide-ion conducting electrolytes: Poisson-Cahn vs Poisson-Boltzmann theories. *Journal of the American Ceramic Society* **103**, 5–22 (2020).

27. Vikrant, K. S. N., Chueh, W. C. & García, R. E. Charged interfaces: Electrochemical and mechanical effects. *Energy and Environmental Science* **11**, 1993–2000 (2018).

28. Boland, T. M., Rez, P., Crozier, P. A. & Singh, A. K. Impact of Aliovalent Alkaline-Earth metal solutes on Ceria Grain Boundaries: A density functional theory study. *Acta Materialia* **205**, 116481 (2021).

29. Carter, C. B. & Norton, M. G. *Ceramic Materials: Science and Engineering*. (Springer, New York, NY, 2013). doi:10.1007/978-1-4614-3523-5.

30. Burgers, J. M. Geometrical considerations concerning the structural irregularities to be assumed in a crystal. *Proc. Phys. Soc.* **52**, 23 (1940).

31. Yeh, J. W., Chen, Y. L., Lin, S. J. & Chen, S. K. High-Entropy Alloys – A New Era of Exploitation. *Materials Science Forum* **560**, 1–9 (2007).

32. Cantor, B., Chang, I. T. H., Knight, P. & Vincent, A. J. B. Microstructural development in equiatomic multicomponent alloys. *Materials Science and Engineering: A* **375–377**, 213–218 (2004).

33. Rost, C. M. *et al.* Entropy-stabilized oxides. *Nature Communications* **6**, (2015).

34. Microstructural evolution and mechanical properties of (Mg,Co,Ni,Cu,Zn)O high-entropy ceramics - Hong - 2019 - Journal of the American Ceramic Society - Wiley Online Library. https://ceramics.onlinelibrary.wiley.com/doi/full/10.1111/jace.16075.

35. Sarkar, A. *et al.* High-Entropy Oxides: Fundamental Aspects and Electrochemical Properties. *Advanced Materials* **31**, 1806236 (2019).

36. Wang, J. *et al.* Lithium containing layered high entropy oxide structures. *Sci Rep* **10**, 18430 (2020).

37. Wang, Q. *et al.* High entropy oxides as anode material for Li-ion battery applications: A practical approach. *Electrochemistry Communications* **100**, 121–125 (2019).

38. Sarkar, A. *et al.* High entropy oxides for reversible energy storage. *Nat Commun* **9**, 3400 (2018).

39. Albedwawi, S. H., AlJaberi, A., Haidemenopoulos, G. N. & Polychronopoulou, K. High entropy oxides-exploring a paradigm of promising catalysts: A review. *Materials & Design* **202**, 109534 (2021).

40. Oses, C., Toher, C. & Curtarolo, S. High-entropy ceramics. *Nat Rev Mater* **5**, 295–309 (2020).

41. Sarkar, A. *et al.* High entropy oxides for reversible energy storage. *Nature Communications* **9**, (2018).

42. Qiu, N. *et al.* A high entropy oxide (Mg0.2Co0.2Ni0.2Cu0.2Zn0.2O) with superior lithium storage performance. *Journal of Alloys and Compounds* **777**, 767–774 (2019).

43. Wei, X.-F. *et al.* High entropy carbide ceramics from different starting materials. *Journal of the European Ceramic Society* **39**, 2989–2994 (2019).

44. Castle, E., Csanádi, T., Grasso, S., Dusza, J. & Reece, M. Processing and Properties of High-Entropy Ultra-High Temperature Carbides. *Sci Rep* **8**, 8609 (2018).

45. Han, X. *et al.* Improved creep resistance of high entropy transition metal carbides. *Journal of the European Ceramic Society* **40**, 2709–2715 (2020).

46. Harrington, T. J. *et al.* Phase stability and mechanical properties of novel high entropy transition metal carbides. *Acta Materialia* **166**, 271–280 (2019).

47. Feng, L., Fahrenholtz, W. G. & Hilmas, G. E. Processing of dense high-entropy boride ceramics. *Journal of the European Ceramic Society* **40**, 3815–3823 (2020).

48. Gild, J. *et al.* High-Entropy Metal Diborides: A New Class of High-Entropy Materials and a New Type of Ultrahigh Temperature Ceramics. *Sci Rep* **6**, 37946 (2016).

49. Qin, M., Yan, Q., Liu, Y. & Luo, J. A new class of high-entropy M3B4 borides. *J Adv Ceram* **10**, 166–172 (2021).

50. Shibata, N. *et al.* Rare-earth adsorption at intergranular interfaces in silicon nitride ceramics: Subnanometer observations and theory. *Phys. Rev. B* **72**, 140101 (2005).

51. Moskovskikh, D. *et al.* Extremely hard and tough high entropy nitride ceramics. *Sci Rep* **10**, 19874 (2020).

52. Dippo, O. F., Mesgarzadeh, N., Harrington, T. J., Schrader, G. D. & Vecchio, K. S. Bulk high-entropy nitrides and carbonitrides. *Sci Rep* **10**, 21288 (2020).

53. Gabriel, E. *et al.* Heterostructure engineering in electrode materials for sodium-ion batteries: Recent progress and perspectives. *eScience* **3**, 100139 (2023).

54. Zhao, C. *et al.* Heterointerface engineering for enhancing the electrochemical performance of solid oxide cells. *Energy & Environmental Science* **13**, 53–85 (2020).

55. Nakayama, M. & Martin, M. First-principles study on defect chemistry and migration of oxide ions in ceria doped with rare-earth cations. *Phys. Chem. Chem. Phys.* **11**, 3241–3249 (2009).

56. Gu, Y., Li, G., Meng, G. & Peng, D. Sintering and electrical properties of coprecipitation prepared Ce0.8Y0.2O1.9 ceramics. *Materials Research Bulletin* **35**, 297–304 (2000).

57. Inaba, H., Nakajima, T. & Tagawa, H. Sintering behaviors of ceria and gadolinia-doped ceria. *Solid State Ionics* **106**, 263–268 (1998).

58. Lobo, L. S. & Ruban Kumar, A. Structural and electrical properties of ZnCo2O4 spinel synthesized by sol-gel combustion method. *Journal of Non-Crystalline Solids* **505**, 301–309 (2019).

59. Anselmi-Tamburini, U., Gennari, S., Garay, J. E. & Munir, Z. A. Fundamental investigations on the spark plasma sintering/synthesis process: II. Modeling of current and temperature distributions. *Materials Science and Engineering: A* **394**, 139–148 (2005).

60. Hulbert, D. M. *et al.* The absence of plasma in "spark plasma sintering". *Journal of Applied Physics* **104**, 033305 (2008).

61. Wang, S., Kobayashi, T., Dokiya, M. & Hashimoto, T. Electrical and Ionic Conductivity of Gd-Doped Ceria. *J. Electrochem. Soc.* **147**, 3606 (2000).

62. Xiong, Y.-P. *et al.* Electronic conductivity of pure ceria. *Solid State Ionics* **192**, 476–479 (2011).

63. Guo, X. & Maier, J. Grain Boundary Blocking Effect in Zirconia: A Schottky Barrier Analysis. *J. Electrochem. Soc.* **148**, E121 (2001).

64. Jasper, A., Kilner, J. A. & McComb, D. W. TEM and impedance spectroscopy of doped ceria electrolytes. *Solid State Ionics* **179**, 904–908 (2008).

65. Bonanos, N., Steele, B. C. H. & Butler, E. P. Applications of Impedance Spectroscopy. in *Impedance Spectroscopy* 205–537 (John Wiley & Sons, Ltd, 2005). doi:10.1002/0471716243.ch4.

66. Inkson, B. J. 2 - Scanning electron microscopy (SEM) and transmission electron microscopy (TEM) for materials characterization. in *Materials Characterization Using Nondestructive Evaluation (NDE) Methods* (eds. Hübschen, G., Altpeter, I., Tschuncky, R. & Herrmann, H.-G.) 17–43 (Woodhead Publishing, 2016). doi:10.1016/B978-0-08-100040-3.00002-X.

67. Langford, R. M. Focused ion beams techniques for nanomaterials characterization. *Microscopy Research and Technique* **69**, 538–549 (2006).

68. Williams, D. B. & Carter, C. B. The Transmission Electron Microscope. in *Transmission Electron Microscopy: A Textbook for Materials Science* (eds. Williams, D. B. & Carter, C. B.) 3–17 (Springer US, Boston, MA, 1996). doi:10.1007/978-1-4757-2519-3_1.

69. Pennycook, S. J. A Scan Through the History of STEM. in *Scanning Transmission Electron Microscopy: Imaging and Analysis* (eds. Pennycook, S. J. & Nellist, P. D.) 1–90 (Springer, New York, NY, 2011). doi:10.1007/978-1-4419-7200-2_1.

70. Scanning Transmission Electron Microscopy | SpringerLink. https://link.springer.com/chapter/10.1007/978-3-030-00069-1_2.

71. Thomas, J. & Gemming, T. *Analytical Transmission Electron Microscopy: An Introduction for Operators*. (Springer Science & Business, 2014).

72. Hren, J. *Introduction to Analytical Electron Microscopy*. (Springer Science & Business Media, 2013).

73. Shindo, D. & Oikawa, T. *Analytical Electron Microscopy for Materials Science*. (Springer Japan, Tokyo, 2002). doi:10.1007/978-4-431-66988-3.

74. Zou, X., Hovmöller, S. & Oleynikov, P. *Electron Crystallography: Electron Microscopy and Electron Diffraction*. (Oxford University Press, 2011). doi:10.1093/acprof:oso/9780199580200.001.0001.

75. Egerton, R. F. An Introduction to EELS. in *Electron Energy-Loss Spectroscopy in the Electron Microscope* 1–28 (Springer US, 2011).

76. Menon, N. K. & Krivanek, O. L. Synthesis of Electron Energy Loss Spectra for the Quantification of Detection Limits. *Microscopy and Microanalysis* **8**, 203–215 (2002).

77. Bacon, N. J. *et al.* Nion UltraSTEM: An Aberration-Corrected STEM for Imaging and Analysis. *Microscopy and Microanalysis* **11**, 1422–1423 (2005).

78. Krivanek, O. L. & Paterson, J. H. Elnes of 3d transition-metal oxides. I. Variations across the periodic table. *Ultramicroscopy* **32**, 313–318 (1990).

79. Manoubi, T., Colliex, C. & Rez, P. Quantitative electron energy loss spectroscopy on M45 edges in rare earth oxides. *Journal of electron spectroscopy and related phenomena* **50**, 1–18 (1990).

80. Botton, G. & Prabhudev, S. Analytical Electron Microscopy. in *Springer Handbook of Microscopy* (eds. Hawkes, P. W. & Spence, J. C. H.) 345–453 (Springer International Publishing, Cham, 2019). doi:10.1007/978-3-030-00069-1_7.

81. Fop, S. *et al.* High oxide ion and proton conductivity in a disordered hexagonal perovskite. *Nat. Mater.* **19**, 752–757 (2020).

82. Poletayev, A. D., Dawson, J. A., Islam, M. S. & Lindenberg, A. M. Defect-driven anomalous transport in fast-ion conducting solid electrolytes. *Nat. Mater.* **21**, 1066–1073 (2022).

83. Schweiger, S., Pfenninger, R., Bowman, W. J., Aschauer, U. & Rupp, J. L. M. Designing Strained Interface Heterostructures for Memristive Devices. *Advanced Materials* **29**, 1605049 (2017).

84. Xu, X. *et al.* Variability and origins of grain boundary electric potential detected by electron holography and atom-probe tomography. *Nat. Mater.* **19**, 887–893 (2020).

85. Xu, X. *et al.* Local Multimodal Electro-Chemical-Structural Characterization of Solid-Electrolyte Grain Boundaries. *Advanced Energy Materials* **11**, 2003309 (2021).

86. Gregori, G., Merkle, R. & Maier, J. Ion conduction and redistribution at grain boundaries in oxide systems. *Progress in Materials Science* **89**, 252–305 (2017).

87. Zhang, Z. & Nazar, L. F. Exploiting the paddle-wheel mechanism for the design of fast ion conductors. *Nat Rev Mater* **7**, 389–405 (2022).

88. Takeiri, F. *et al.* Hydride-ion-conducting K2NiF4-type Ba–Li oxyhydride solid electrolyte. *Nat. Mater.* **21**, 325–330 (2022).

89. Butz, B. *et al.* Correlation between microstructure and degradation in conductivity for cubic Y2O3-doped ZrO2. *Solid State Ionics* **177**, 3275–3284 (2006).

90. Butz, B., Schneider, R., Gerthsen, D., Schowalter, M. & Rosenauer, A. Decomposition of 8.5mol.% Y2O3-doped zirconia and its contribution to the degradation of ionic conductivity. *Acta Materialia* **57**, 5480–5490 (2009).

91. Butz, B. *et al.* Accelerated degradation of 8.5mol% Y2O3-doped zirconia by dissolved Ni. *Solid State Ionics* **214**, 37–44 (2012).

92. Kilner, J. A. Fast oxygen transport in acceptor doped oxides. *Solid State Ionics* **129**, 13–23 (2000).

93. Badwal, S. P. S. *et al.* Structural and microstructural stability of ceria – gadolinia electrolyte exposed to reducing environments of high temperature fuel cells. *J. Mater. Chem. A* **1**, 10768–10782 (2013).

94. Chourashiya, M. G., Bhardwaj, S. R. & Jadhav, L. D. Fabrication of 10%Gd-doped ceria (GDC)/NiO–GDC half cell for low or intermediate temperature solid oxide fuel cells using spray pyrolysis. *J Solid State Electrochem* **14**, 1869–1875 (2010).

95. Tschöpe, A., Kilassonia, S. & Birringer, R. The grain boundary effect in heavily doped cerium oxide. *Solid State Ionics* **173**, 57–61 (2004).

96. Ebert, J. N., Jennings, D., Schäfer, L.-A., Sebold, D. & Rheinheimer, W. Bulk and grain boundary conductivity in doped BaZrO3: Bulk contribution dominates at operating temperatures. *Scripta Materialia* **241**, 115852 (2024).

97. Verkerk, M. J., Middelhuis, B. J. & Burggraaf, A. J. Effect of grain boundaries on the conductivity of high-purity ZrO2□Y2O3 ceramics. *Solid State Ionics* **6**, 159–170 (1982).

98. Avila-Paredes, H. J., Choi, K., Chen, C.-T. & Kim, S. Dopant-concentration dependence of grain-boundary conductivity in ceria: A space-charge analysis. *J. Mater. Chem.* **19**, 4837–4842 (2009).

99. Kliewer, K. L. & Koehler, J. S. Space Charge in Ionic Crystals. I. General Approach with Application to NaCl. *Phys. Rev.* **140**, A1226–A1240 (1965).

100. Maier, J. Ionic conduction in space charge regions. *Progress in Solid State Chemistry* **23**, 171–263 (1995).

101. Hojo, H. *et al.* Atomic Structure of a CeO2 Grain Boundary: The Role of Oxygen Vacancies. *Nano Lett.* **10**, 4668–4672 (2010).

102. McNealy, B. E. & Hertz, J. L. On the use of the constant phase element to understand variation in grain boundary properties. *Solid State Ionics* **256**, 52–60 (2014).

103. Bowman, W. J., Kelly, M. N., Rohrer, G. S., Hernandez, C. A. & Crozier, P. A. Enhanced ionic conductivity in electroceramics by nanoscale enrichment of grain boundaries with high solute concentration. *Nanoscale* **9**, 17293–17302 (2017).

104. Defferriere, T., Klotz, D., Gonzalez-Rosillo, J. C., Rupp, J. L. M. & Tuller, H. L. Photo-enhanced ionic conductivity across grain boundaries in polycrystalline ceramics. *Nat. Mater.* **21**, 438–444 (2022).

105. R. Diercks, D. *et al.* Three-dimensional quantification of composition and electrostatic potential at individual grain boundaries in doped ceria. *Journal of Materials Chemistry A* **4**, 5167–5175 (2016).

106. Neuhaus, K. & Wiemhöfer, H.-D. Electrochemical characteristics of grain boundaries in gadolinium and aluminum co-doped ceria and ceria-alumina composites. *Solid State Ionics* **371**, 115771 (2021).

107. Usler, A. L. & Souza, R. A. D. A Critical Examination of the Mott–Schottky Model of Grain-Boundary Space-Charge Layers in Oxide-Ion Conductors. *J. Electrochem. Soc.* **168**, 056504 (2021).

108. Lee, H. B., Prinz, F. B. & Cai, W. Atomistic simulations of grain boundary segregation in nanocrystalline yttria-stabilized zirconia and gadolinia-doped ceria solid oxide electrolytes. *Acta Materialia* **61**, 3872–3887 (2013).

109. Kim, S. K., Khodorov, S., Lubomirsky, I. & Kim, S. A linear diffusion model for ion current across blocking grain boundaries in oxygen-ion and proton conductors. *Phys. Chem. Chem. Phys.* **16**, 14961–14968 (2014).

110. Shibata, N., Ikuhara, Y., Oba, F., Yamamoto, T. & Sakuma, T. Atomic structure and solute segregation of a $\Sigma = 3$, [110]/111 grain boundary in an yttria-stabilized cubic zirconia bicrystal. *Philosophical Magazine Letters* **82**, 393–400 (2002).

111. Boland, T. M., Rez, P., Crozier, P. A. & Singh, A. K. Impact of Aliovalent Alkaline-Earth metal solutes on Ceria Grain Boundaries: A density functional theory study. *Acta Materialia* **205**, 116481 (2021).

112. N. Vikrant, K. S., C. Chueh, W. & Edwin García, R. Charged interfaces: electrochemical and mechanical effects. *Energy & Environmental Science* **11**, 1993–2000 (2018).

113. Lund, J., Vikrant, K. S. N., Bishop, C. M., Rheinheimer, W. & García, R. E. Thermodynamically consistent variational principles for charged interfaces. *Acta Materialia* **205**, 116525 (2021).

114. S. Mebane, D. & Souza, R. A. D. A generalised space-charge theory for extended defects in oxygen-ion conducting electrolytes: from dilute to concentrated solid solutions. *Energy & Environmental Science* **8**, 2935–2940 (2015).

115. Tong, X., Bowman, W. J., Mejia-Giraldo, A., Crozier, P. A. & Mebane, D. S. New Data-Driven Interacting-Defect Model Describing Nanoscopic Grain Boundary Compositions in Ceramics. *J. Phys. Chem. C* **124**, 23619–23625 (2020).

116. Tong, X., Mebane, D. S. & De Souza, R. A. Analyzing the grain-boundary resistance of oxide-ion conducting electrolytes: Poisson-Cahn vs Poisson-Boltzmann theories. *Journal of the American Ceramic Society* **103**, 5–22 (2020).

117. Higashi, K., Sonoda, K., Ono, H., Sameshima, S. & Hirata, Y. Synthesis and sintering of rare-earth-doped ceria powder by the oxalate coprecipitation method. *Journal of Materials Research* **14**, 957–967 (1999).

118. Ritchie, N. W. Standards-Based Quantification in DTSA-II—Part I. *Microscopy Today* **19**, 30–36 (2011).

119. Cliff, G. & Lorimer, G. W. The quantitative analysis of thin specimens. *Journal of Microscopy* **103**, 203–207 (1975).

120. Lorimer, G. W. Quantitative X-ray microanalysis of thin specimens in the transmission electron microscope; a review. *Mineralogical Magazine* **51**, 49–60 (1987).

121. Prieto, C. *et al.* X-ray absorption spectroscopy of the continuous change from Ce(IV) to Ce(III). *Journal of Physics and Chemistry of Solids* **53**, 233–237 (1992).

122. Duncan, H. & Lasia, A. Influence of the electrode nature on conductivity measurements of gadolinia-doped ceria. *Solid State Ionics* **176**, 1429–1437 (2005).

123. Haile, S. M., West, D. L. & Campbell, J. The role of microstructure and processing on the proton conducting properties of gadolinium-doped barium cerate. *Journal of Materials Research* **13**, 1576–1595 (1998).

124. Bowman, W. J., Zhu, J., Sharma, R. & Crozier, P. A. Electrical conductivity and grain boundary composition of Gd-doped and Gd/Pr co-doped ceria. *Solid State Ionics* **272**, 9–17 (2015).

125. Roberts, J. N. & Schwartz, L. M. Grain consolidation and electrical conductivity in porous media. *Phys. Rev. B* **31**, 5990–5997 (1985).

126. Vischjager, D. J., van Zomeren, A. A., Schoonman, J., Kontoulis, I. & Steele, B. C. H. Ionic conductivity of ceramic superconductors. *Solid State Ionics* **40–41**, 810–814 (1990).

127. Reich, B. J., Storlie, C. B. & Bondell, H. D. Variable Selection in Bayesian Smoothing Spline ANOVA Models: Application to Deterministic Computer Codes. *Technometrics* **51**, 110–120 (2009).

128. Hayes, K., Fouts, M. W., Baheri, A. & Mebane, D. S. Forward variable selection enables fast and accurate dynamic system identification with Karhunen-Lo\`eve decomposed Gaussian processes. Preprint at https://doi.org/10.48550/arXiv.2205.13676 (2023).

129. Scott, S. L. *et al.* Bayes and big data: the consensus Monte Carlo algorithm. *International Journal of Management Science and Engineering Management* **11**, 78–88 (2016).

130. Vahidi, H. *et al.* A Review of Grain Boundary and Heterointerface Characterization in Polycrystalline Oxides by (Scanning) Transmission Electron Microscopy. *Crystals* **11**, 878 (2021). https://doi.org/10.3390/cryst11080878

131. Kirkland, E. J. Some effects of electron channeling on electron energy loss spectroscopy. *Ultramicroscopy* **102**, 199–207 (2005).

132. Song, K. *et al.* Cerium reduction at the interface between ceria and yttria-stabilised zirconia and implications for interfacial oxygen non-stoichiometry. *APL Materials* **2**, 032104 (2014).

133. Luches, P. *et al.* Atomic Scale Structure and Reduction of Cerium Oxide at the Interface with Platinum. *Advanced Materials Interfaces* **2**, 1500375 (2015).

134. Garvie, L. A. J. & Buseck, P. R. Determination of Ce4+/Ce3+ in electron-beam-damaged CeO2 by electron energy-loss spectroscopy. *Journal of Physics and Chemistry of Solids* **60**, 1943–1947 (1999).

135. Burton, G. L., Ricote, S., Foran, B. J., Diercks, D. R. & Gorman, B. P. Quantification of grain boundary defect chemistry in a mixed proton-electron conducting oxide composite. *Journal of the American Ceramic Society* **103**, 3217–3230 (2020).

136. Guo, X. & Waser, R. Electrical properties of the grain boundaries of oxygen ion conductors: Acceptor-doped zirconia and ceria. *Progress in Materials Science* **51**, 151–210 (2006).

137. Van Laethem, D., Deconinck, J. & Hubin, A. Ionic conductivity of space charge layers in acceptor doped ceria. *Journal of the European Ceramic Society* **39**, 432–441 (2019).

138. Bae, J. *et al.* Thermally-Induced Dopant Segregation Effects on the Space Charge Layer and Ionic Conductivity of Nanocrystalline Gadolinia-Doped Ceria. *J. Electrochem. Soc.* **163**, F919 (2016).

139. Parras, J. P. *et al.* The grain-boundary resistance of CeO2 ceramics: A combined microscopy-spectroscopy-simulation study of a dilute solution. *Journal of the American Ceramic Society* **103**, 1755–1764 (2020).

140. Avila-Paredes, H. J. & Kim, S. The effect of segregated transition metal ions on the grain boundary resistivity of gadolinium doped ceria: Alteration of the space charge potential. *Solid State Ionics* **177**, 3075–3080 (2006).

141. Kharton, V. V. *et al.* Ceria-based materials for solid oxide fuel cells. *Journal of Materials Science* **36**, 1105–1117 (2001).

142. Christie, G. M. & van Berkel, F. P. F. Microstructure — ionic conductivity relationships in ceria-gadolinia electrolytes. *Solid State Ionics* **83**, 17–27 (1996).

143. Sánchez-Bravo, G. B. *et al.* Influence of the precursor pyrolysis temperature on the microstructure and conductivity of Gd-doped ceria materials. *Journal of the European Ceramic Society* **33**, 1825–1832 (2013).

144. Ralph, J. M., Kilner, J. A. & Steele, B. C. H. Improving Gd-Doped Ceria Electrolytes for Low Temperature Solid Oxide Fuel Cells. *MRS Online Proceedings Library (OPL)* **575**, 309 (1999).

145. Zhang, T. S. *et al.* Different conduction behaviors of grain boundaries in SiO2-containing 8YSZ and CGO20 electrolytes. *Solid State Ionics* **177**, 1227–1235 (2006).

146. Zhang, T. S., Ma, J., Cheng, H. & Chan, S. H. Ionic conductivity of high-purity Gd-doped ceria solid solutions. *Materials Research Bulletin* **41**, 563–568 (2006).

147. Kudo, T. & Obayashi, H. Mixed Electrical Conduction in the Fluorite-Type Ce1 − x Gd x O 2 − x / 2. *J. Electrochem. Soc.* **123**, 415 (1976).

148. Grieshammer, S., Nakayama, M. & Martin, M. Association of defects in doped non-stoichiometric ceria from first principles. *Phys. Chem. Chem. Phys.* **18**, 3804–3811 (2016).

149. Schmitt, R. *et al.* A review of defect structure and chemistry in ceria and its solid solutions. *Chem. Soc. Rev.* **49**, 554–592 (2020).

150. Genreith-Schriever, A. R., Parras, J. P., Heelweg, H. J. & De Souza, R. A. The Intrinsic Structural Resistance of a Grain Boundary to Transverse Ionic Conduction. *ChemElectroChem* **7**, 4718–4723 (2020).

151. Bowman, W. J., Darbal, A. & Crozier, P. A. Linking Macroscopic and Nanoscopic Ionic Conductivity: A Semiempirical Framework for Characterizing Grain Boundary Conductivity in Polycrystalline Ceramics. *ACS Appl. Mater. Interfaces* **12**, 507–517 (2020).

152. Zeng, Y. *et al.* High-entropy mechanism to boost ionic conductivity. *Science* **378**, 1320–1324 (2022).

153. Bérardan, D., Franger, S., Dragoe, D., Meena, A. K. & Dragoe, N. Colossal dielectric constant in high entropy oxides. *physica status solidi (RRL) – Rapid Research Letters* **10**, 328–333 (2016).

154. Rost, C. M. *et al.* On the thermal and mechanical properties of Mg0.2Co0.2Ni0.2Cu0.2Zn0.2O across the high-entropy to entropy-stabilized transition. *APL Materials* **10**, 121108 (2022).

155. Wang, D. *et al.* Spinel-structured high entropy oxide (FeCoNiCrMn)3O4 as anode towards superior lithium storage performance. *Journal of Alloys and Compounds* **844**, 156158 (2020).

156. Zhao, B. *et al.* High-Entropy Enhanced Microwave Attenuation in Titanate Perovskites. *Advanced Materials* **35**, 2210243 (2023).

157. Wang, K. *et al.* Synergy of cations in high entropy oxide lithium ion battery anode. *Nat Commun* **14**, 1487 (2023).

158. Su, L. *et al.* Direct observation of elemental fluctuation and oxygen octahedral distortion-dependent charge distribution in high entropy oxides. *Nat Commun* **13**, 2358 (2022).

159. Dupuy, A. D., Wang, X. & Schoenung, J. M. Entropic phase transformation in nanocrystalline high entropy oxides. *Materials Research Letters* **7**, 60–67 (2019).

160. Guo, H., Wang, X., Dupuy, A. D., Schoenung, J. M. & Bowman, W. J. Growth of nanoporous high-entropy oxide thin films by pulsed laser deposition. *Journal of Materials Research* **37**, 124–135 (2022).

161. Guo, H. *et al.* Designing Nanostructure Exsolution-Self-Assembly in a Complex Concentrated Oxide. *Matter (in press)* (2023).

162. Sarkar, A. *et al.* High-Entropy Oxides: Fundamental Aspects and Electrochemical Properties. *Advanced Materials* **31**, 1806236 (2019).

163. Ning, Y. *et al.* Achieving high energy storage properties in perovskite oxide via high-entropy design. *Ceramics International* **49**, 12214–12223 (2023).

164. Xiao, J. *et al.* Recent progress of emerging cathode materials for sodium ion batteries. *Materials Chemistry Frontiers* **5**, 3735–3764 (2021).

165. Gao, X. *et al.* Recent Advances for High-Entropy based Layered Cathodes for Sodium Ion Batteries. *Small Methods* **7**, 2300152 (2023).

166. Bérardan, D., Franger, S., K. Meena, A. & Dragoe, N. Room temperature lithium superionic conductivity in high entropy oxides. *Journal of Materials Chemistry A* **4**, 9536–9541 (2016).

167. Xu, Y., Xu, X. & Bi, L. A high-entropy spinel ceramic oxide as the cathode for proton-conducting solid oxide fuel cells. *J Adv Ceram* **11**, 794–804 (2022).

168. Sun, Y. & Dai, S. High-entropy materials for catalysis: A new frontier. *Science Advances* **7**, (2021).

169. Rost, C. M. *et al.* Entropy-stabilized oxides. *Nat Commun* **6**, 8485 (2015).

170. Davies, P. K. & Navrotsky, A. Thermodynamics of solid solution formation in NiO□MgO and NiO□ZnO. *Journal of Solid State Chemistry* **38**, 264–276 (1981).

171. Brahlek, M. *et al.* What is in a name: Defining “high entropy” oxides. *APL Materials* **10**, 110902 (2022).

172. Salian, A. & Mandal, S. Entropy stabilized multicomponent oxides with diverse functionality – a review. *Critical Reviews in Solid State and Materials Sciences* **47**, 1–52 (2021).

173. Amiri, A. & Shahbazian-Yassar, R. Recent progress of high-entropy materials for energy storage and conversion. *J. Mater. Chem. A* **9**, 782–823 (2021).

174. Moździerz, M. *et al.* Mixed ionic-electronic transport in the high-entropy (Co,Cu,Mg,Ni,Zn)1-xLixO oxides. *Acta Materialia* **208**, 116735 (2021).

175. Balcerzak, M., Kawamura, K., Bobrowski, R., Rutkowski, P. & Brylewski, T. Mechanochemical Synthesis of (Co,Cu,Mg,Ni,Zn)O High-Entropy Oxide and Its Physicochemical Properties. *J. Electron. Mater.* **48**, 7105–7113 (2019).

176. Dupuy, A. D. & Schoenung, J. M. Morphological evolution in nanostructured secondary phases in entropy stabilized oxides. *Materials Characterization* **193**, 112301 (2022).

177. Dupuy, A. D. *et al.* Hidden transformations in entropy-stabilized oxides. *Journal of the European Ceramic Society* **41**, 6660–6669 (2021).

178. Lee, J. & Chung, D. S. Heterojunction oxide thin film transistors: a review of recent advances. *J. Mater. Chem. C* **11**, 5241–5256 (2023).

179. Vahidi, H. *et al.* Reversible Enhancement of Electronic Conduction Caused by Phase Transformation and Interfacial Segregation in an Entropy-Stabilized Oxide. *Advanced Functional Materials* **n/a**, 2315895. https://doi.org/10.1002/adfm.202315895

180. Harrington, G. F. *et al.* Tailoring Nonstoichiometry and Mixed Ionic Electronic Conductivity in Pr0.1Ce0.9O2−δ/SrTiO3 Heterostructures. *ACS Appl. Mater. Interfaces* **11**, 34841–34853 (2019).

181. Lee, T. *et al.* Atomic-scale origin of the low grain-boundary resistance in perovskite solid electrolyte Li0. 375Sr0. 4375Ta0. 75Zr0. 25O3. *Nature Communications* **14**, 1940 (2023).

182. Ko, S.-T. *et al.* Compositionally complex perovskite oxides: Discovering a new class of solid electrolytes with interface-enabled conductivity improvements. *Matter* (2023).

183. Tong, X., Bowman, W. J., Mejia-Giraldo, A., Crozier, P. A. & Mebane, D. S. New Data-Driven Interacting-Defect Model Describing Nanoscopic Grain Boundary Compositions in Ceramics. *J. Phys. Chem. C* **124**, 23619–23625 (2020).

184. *Introduction to Focused Ion Beams: Instrumentation, Theory, Techniques and Practice*. (Springer US, Boston, MA, 2005). doi:10.1007/b101190.

185. Kresse, G. & Furthmüller, J. Efficient iterative schemes for ab initio total-energy calculations using a plane-wave basis set. *Phys. Rev. B* **54**, 11169–11186 (1996).

186. Kresse, G. & Furthmüller, J. Efficiency of ab-initio total energy calculations for metals and semiconductors using a plane-wave basis set. *Computational Materials Science* **6**, 15–50 (1996).

187. Janisch, R. & Elsässer, C. Segregated light elements at grain boundaries in niobium and molybdenum. *Phys. Rev. B* **67**, 224101 (2003).

188. Dudarev, S. L., Botton, G. A., Savrasov, S. Y., Humphreys, C. J. & Sutton, A. P. Electron-energy-loss spectra and the structural stability of nickel oxide: An LSDA+U study. *Phys. Rev. B* **57**, 1505–1509 (1998).

189. Blöchl, P. E. Projector augmented-wave method. *Phys. Rev. B* **50**, 17953–17979 (1994).

190. Kresse, G. & Joubert, D. From ultrasoft pseudopotentials to the projector augmented-wave method. *Phys. Rev. B* **59**, 1758–1775 (1999).

191. Monkhorst, H. J. & Pack, J. D. Special points for Brillouin-zone integrations. *Phys. Rev. B* **13**, 5188–5192 (1976).

192. Grzesik, Z. *et al.* Defect structure and transport properties in (Co,Cu,Mg,Ni,Zn)O high entropy oxide. *Journal of the European Ceramic Society* **39**, 4292–4298 (2019).

193. Hristova, E., Janisch, R., Drautz, R. & Hartmaier, A. Solubility of carbon in α-iron under volumetric strain and close to the Σ5(310)[001] grain boundary: Comparison of DFT and empirical potential methods. *Computational Materials Science* **50**, 1088–1096 (2011).

194. Osenciat, N. *et al.* Charge compensation mechanisms in Li-substituted high-entropy oxides and influence on Li superionic conductivity. *Journal of the American Ceramic Society* **102**, 6156–6162 (2019).

195. Zhou, X., Marchand, D., McDowell, D. L., Zhu, T. & Song, J. Chemomechanical Origin of Hydrogen Trapping at Grain Boundaries in fcc Metals. *Phys. Rev. Lett.* **116**, 075502 (2016).

196. Akdoğan, E. K. *et al.* Pressure effects on phase equilibria and solid solubility in MgO-Y2O3 nanocomposites. *Journal of Applied Physics* **111**, 053506 (2012).

197. Wang, S., Kobayashi, T., Dokiya, M. & Hashimoto, T. Electrical and Ionic Conductivity of Gd-Doped Ceria. *J. Electrochem. Soc.* **147**, 3606 (2000).

198. Kikuchi, S., Oda, H., Kiyohara, S. & Mizoguchi, T. Bayesian optimization for efficient determination of metal oxide grain boundary structures. *Physica B: Condensed Matter* **532**, 24–28 (2018).

199. Xia, Y. *et al.* Molecular Dynamics Simulations of Xe Behaviors at the Grain Boundary in UO2. *Metals* **12**, 763 (2022).

200. Hirel, P., Moladje, G. F. B., Carrez, P. & Cordier, P. Systematic theoretical study of [001] symmetric tilt grain boundaries in MgO from 0 to 120 GPa. *Phys Chem Minerals* **46**, 37–49 (2019).

201. Bowman, W. J., Kelly, M. N., Rohrer, G. S., Hernandez, C. A. & Crozier, P. A. Enhanced ionic conductivity in electroceramics by nanoscale enrichment of grain boundaries with high solute concentration. *Nanoscale* **9**, 17293–17302 (2017).

202. Bowman, W. J., Darbal, A. & Crozier, P. A. Linking Macroscopic and Nanoscopic Ionic Conductivity: A Semiempirical Framework for Characterizing Grain Boundary Conductivity in Polycrystalline Ceramics. *ACS Appl. Mater. Interfaces* **12**, 507–517 (2020).

203. Berardan, D., Meena, A. K., Franger, S., Herrero, C. & Dragoe, N. Controlled Jahn-Teller distortion in (MgCoNiCuZn)O-based high entropy oxides. *Journal of Alloys and Compounds* **704**, 693–700 (2017).

204. O'Brien, M. C. M. & Chancey, C. C. The Jahn–Teller effect: An introduction and current review. *American Journal of Physics* **61**, 688–697 (1993).

205. Guo, X., Sigle, W. & Maier, J. Blocking Grain Boundaries in Yttria-Doped and Undoped Ceria Ceramics of High Purity. *Journal of the American Ceramic Society* **86**, 77–87 (2003).

206. Dupuy, A. D. *et al.* Hidden transformations in entropy-stabilized oxides. *Journal of the European Ceramic Society* **41**, 6660–6669 (2021).

207. Dupuy, A. D., Chellali, M. R., Hahn, H. & Schoenung, J. M. Nucleation and growth behavior of multicomponent secondary phases in entropy-stabilized oxides. *Journal of Materials Research* (2022) doi:10.1557/s43578-022-00784-y.

208. Porter, D. A., Easterling, K. E. & Easterling, K. E. *Phase Transformations in Metals and Alloys (Revised Reprint)*. (CRC Press, Boca Raton, 2009). doi:10.1201/9781439883570.

209. Lensch-Falk, J. L., Sugar, J. D., Hekmaty, M. A. & Medlin, D. L. Morphological evolution of Ag2Te precipitates in thermoelectric PbTe. *Journal of Alloys and Compounds* **504**, 37–44 (2010).

210. Jungblut, R., Johnson, M. T., aan de Stegge, J., Reinders, A. & den Broeder, F. J. A. Orientational and structural dependence of magnetic anisotropy of Cu/Ni/Cu sandwiches: Misfit interface anisotropy. *Journal of Applied Physics* **75**, 6424–6426 (1994).

211. Kim, J. *et al.* Development of coherent-precipitate-hardened high-entropy alloys with hierarchical NiAl/Ni2TiAl precipitates in CrMnFeCoNiAlxTiy alloys. *Materials Science and Engineering: A* **823**, 141763 (2021).

212. Ardell, A. J. & Ozolins, V. Trans-interface diffusion-controlled coarsening. *Nature Mater* **4**, 309–316 (2005).

213. Grzesik, Z. *et al.* Defect structure and transport properties in (Co,Cu,Mg,Ni,Zn)O high entropy oxide. *Journal of the European Ceramic Society* **39**, 4292–4298 (2019).

214. Zhou, H.-B., Jin, S., Zhang, Y., Lu, G.-H. & Liu, F. Anisotropic Strain Enhanced Hydrogen Solubility in bcc Metals: The Independence on the Sign of Strain. *Phys. Rev. Lett.* **109**, 135502 (2012).

215. Chae, S., Williams, L., Lee, J., Heron, J. T. & Kioupakis, E. Effects of local compositional and structural disorder on vacancy formation in entropy-stabilized oxides from first-principles. *npj Comput Mater* **8**, 1–7 (2022).

216. Osenciat, N. *et al.* Charge compensation mechanisms in Li-substituted high-entropy oxides and influence on Li superionic conductivity. *Journal of the American Ceramic Society* **102**, 6156–6162 (2019).

217. Lewis, T. J. & Wright, A. J. The electrical conductivity of magnesium oxide at low temperatures. *J. Phys. D: Appl. Phys.* **1**, 441 (1968).

218. Singh, I. & Bedi, R. K. Studies and correlation among the structural, electrical and gas response properties of aerosol spray deposited self assembled nanocrystalline CuO. *Applied Surface Science* **257**, 7592–7599 (2011).

219. Younas, M., Nadeem, M., Idrees, M. & Akhtar, M. J. Jahn-Teller assisted polaronic hole hopping as a charge transport mechanism in CuO nanograins. *Appl. Phys. Lett.* **100**, 152103 (2012).

220. Lange, F. & Martin, M. The electrical conductivity of CoO: Experimental results and a new conductivity model. *Berichte der Bunsengesellschaft für physikalische Chemie* **101**, 176–184 (1997).

221. Mitoff, S. P. Electrical Conductivity and Thermodynamic Equilibrium in Nickel Oxide. *The Journal of Chemical Physics* **35**, 882–889 (2004).

222. Qiao, L. & Bi, X. Direct observation of Ni3+ and Ni2+ in correlated LaNiO3−δ films. *EPL* **93**, 57002 (2011).

223. Wang, H., Li, C., Zhao, H., Li, R. & Liu, J. Synthesis, characterization, and electrical conductivity of ZnO with different morphologies. *Powder Technology* **239**, 266–271 (2013).

224. Sun, L., Huang, X., Wang, L. & Janotti, A. Disentangling the role of small polarons and oxygen vacancies in $\mathrm{Ce}{\mathrm{O}}_{2}$. *Phys. Rev. B* **95**, 245101 (2017).

225. Balcerzak, M., Kawamura, K., Bobrowski, R., Rutkowski, P. & Brylewski, T. Mechanochemical Synthesis of (Co,Cu,Mg,Ni,Zn)O High-Entropy Oxide and Its Physicochemical Properties. *J. Electron. Mater.* **48**, 7105–7113 (2019).

226. Biesuz, M., Spiridigliozzi, L., Dell'Agli, G., Bortolotti, M. & Sglavo, V. M. Synthesis and sintering of (Mg, Co, Ni, Cu, Zn)O entropy-stabilized oxides obtained by wet chemical methods. *J Mater Sci* **53**, 8074–8085 (2018).

227. Jacobson, V. *et al.* The role of Co valence in charge transport in the entropy-stabilized oxide (Mg0.2Co0.2Ni0.2Cu0.2Zn0.2)O. *Journal of the American Ceramic Society* **106**, 1531–1539 (2023).

228. Dupuy, A. D., Wang, X. & Schoenung, J. M. Entropic phase transformation in nanocrystalline high entropy oxides. *Materials Research Letters* **7**, 60–67 (2019).

229. Vikrant, K. S. N., Chueh, W. C. & García, R. E. Charged interfaces: electrochemical and mechanical effects. *Energy Environ. Sci.* **11**, 1993–2000 (2018).

230. Coles-Aldridge, A. V. & Baker, R. T. Oxygen ion conductivity in ceria-based electrolytes co-doped with samarium and gadolinium. *Solid State Ionics* **347**, 115255 (2020).

231. Venkataramana, K., Madhuri, C., Madhusudan, Ch., Suresh Reddy, Y. & Vishnuvardhan Reddy, C. Investigation on micro-structural, structural, electrical and thermal properties of La3+, Sm3+ & Gd3+ triple-doped ceria as solid-electrolyte for intermediate temperature-solid oxide fuel cell applications. *Journal of Applied Physics* **126**, 144901 (2019).

232. Wang, X. *et al.* Radiation-induced segregation in a ceramic. *Nat. Mater.* **19**, 992–998 (2020).

233. Zhou, N., Hu, T., Huang, J. & Luo, J. Stabilization of nanocrystalline alloys at high temperatures *via* utilizing high-entropy grain boundary complexions. *Scripta Materialia* **124**, 160–163 (2016).

234. Luo, J. & Zhou, N. High-entropy grain boundaries. *Commun Mater* **4**, 1–8 (2023).

235. Tsai, J.-Y. *et al.* A High-Entropy-Oxides-Based Memristor: Outstanding Resistive Switching Performance and Mechanisms in Atomic Structural Evolution. *Advanced Materials* **35**, 2302979 (2023).